UNIVERSITÀ DEGLI STUDI DI CATANIA

Dottorato di Ricerca in Scienza e Tecnologia dei Materiali - XXVIII ciclo

---

Giuseppe Cacciato

Metal-TiO_2 nanocomposites towards efficient solar-driven photocatalysis

Tutor: Prof.ssa M. G. Grimaldi

Supervisors: Dr. M. Zimbone, Dr. F. Ruffino

Coordinatore: Prof.ssa M. G. Grimaldi

Tesi per il conseguimento del titolo

Contents

Abstract

Water, together with energy and food, has been addressed as one of the main urgent problem of humanity. The reduction of fresh clean water sources will definitely lead to huge issues in the next future, especially in developing countries. The conventional wastewater treatments suffer some limitations related to the effectiveness in decontamination (mechanical filtration), in the heavy use of chemicals (chlorination), or in elevate operational costs and energy requirements (desalination and reverse osmosis). In this sense, new materials such as nanocomposites may overcome these issues taking advantage of the peculiar properties of materials at nanoscale. Research on novel nanotechnologies must bring advances in order to contrast and prevent water scarcity and pollution. In order to be effective, these nanotechnologies should run at low operational cost, even in places unequipped by strong infrastructures and in concert with conventional cheap methodologies.

Among the alternative water purification methods, TiO_2-based photocatalysis has attracted great attention due to material stability, abundance, non-toxicity and high decontamination efficiency. In this material, electron-hole pairs, generated by light absorption, separate from each other and migrate to catalytically active sites at the surface of the photocatalyst. Photogenerated carriers are able to induce the water splitting reaction and, consequently, to decompose organic pollutants. The main deficiency of this material, related to its large band gap, is that only the UV fraction of the solar spectrum is effective to this purpose. Several approaches have been proposed to overpass this issue and, among them, the use of metal-TiO_2 nanocomposites with proper nanostructurarion seems very promising for water purification strategies.

Aim of this work is to investigate the possibility to develop efficient solar-driven TiO_2 photocatalyst taking advantage of metallic nanostructures

to efficiently couple the incident light to the photoactive semiconductor. Two approaches have been followed: TiO_2 nanoparticles obtained via pulsed laser ablation in liquid and optical engineering of multilayered metal-TiO_2 thin films. The first approach maximizes the exposed surface, thus enhancing the photocatalytic efficiency. However, in this case nanomaterials is dispersed in the surrounding environment, and in order to avoid this drawback we have investigated, as second approach, the use of metal-TiO_2 thin films.

The outline of the thesis is the following:

- Chapter 1 is devoted to the description of the fundamental processes involved in TiO_2 photocatalysis and to the most recent development in metal-TiO_2 nanocomposites. Particular attention is given to plasmonic metal nanostructures, giving the principles of Localized Surface Plasmon Resonances (LSPR).
- Chapter 2 reports on TiO_2 nanoparticles obtained via laser ablation in liquid.. The structure and morphology of the nanoparticles as well as the photocatalytic activity are accurately described, also in Ag-TiO_2 mixtures. Arguments will be presented to identify the processes responsible for the activity enhancement.
- Chapter 3, Chapter 4 and Chapter 5 describe the studies on metal-TiO_2 nanocomposite films. In these chapters, nanocomposite film of plasmonic metal (Au or Ag) nanoparticles and TiO_2 are structurally, morphologically and optically characterized. More in detail, in Chapter 3 the thermal dewetting is employed as nanostructuration strategy. Then, in Chapter 4 a proper optical engineering of the nanocomposite films has been demonstrated the key factor in order to obtain an enhanced optical response of the film and, in Chapter 5, in order to observe a high photocatalytic activity under visible irradiation.

Chapter 1: Metal-TiO_2 nanocomposites

The conventional wastewater treatments suffer some limitations related to the effectiveness in decontamination, in the heavy use of chemicals, or in elevate operational costs and energy requirements. In this sense, specific nanomaterials and nanocomposites may overcome these issues taking advantage of the peculiar properties of materials at nanoscale. Among the water purification methods, TiO_2-based photocatalysis has attracted great attention due to material stability, abundance, non-toxicity and high activity.

In this chapter we will present the principles of titanium dioxide photocatalysis, followed by a brief review of the recent promising results regarding metal-TiO_2 nanostructures and nanocomposite and the strategies to adopt for environmental remediation applications. Particular attention will be given to the properties and effects of plasmonic metal nanostructures, especially for solar-driven photocatalysis.

1.1 Introduction

Water, together with energy and food, has been addressed as one of the main urgent problem of humanity. The reduction of fresh clean water sources will definitely lead to huge issues in the next future [Win08] [Suà08][Mal09]. The conventional wastewater treatments suffer some limitations related to the effectiveness in decontamination (mechanical filtration), in the heavy use of chemicals (chlorination), or in elevate operational costs and energy requirements (desalination and reverse osmosis)[Sha08]. In this sense, new materials such as nanocomposites may overcome these issues taking advantage of the peculiar properties of materials at nanoscale. Research on novel nanotechnologies must bring advances in order to contrast and prevent water scarcity and pollution. In order to be effective, these nanotechnologies should run at low operational

cost, even in places unequipped by strong infrastructures and in concert with conventional cheap methodologies. In Fig. 1.1 is ideally suggested such a picture, where the advances from nanotechnology can insert at the reverse osmosis step and in the disinfection treatment.

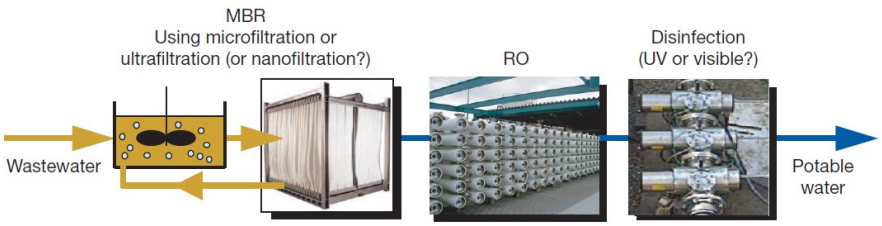

Figure 1.1: Membrane bioreactor (MBR) treatment system for direct conversion to potable water. Depiction of a next generation MBR-based treatment method that can potentially take wastewater from municipal, agricultural, livestock or other high-organic-content sources and convert it to potable water. Future methods may be able to omit the RO step with a nanofiltration membrane, and follow with a visible light disinfection step to ensure that all pathogens, including viruses, are inactivated. From ref. [Sha08].

Among the alternative water purification methods, TiO_2-based photocatalysis has attracted great attention due to material stability, abundance, non-toxicity and high activity [Has05][Fuj08][Cho10]. In this material, electron-hole pairs, generated by a flux of photons, separate from each other and migrate to catalytically active sites at the surface of the photocatalyst. Photogenerated carriers are able to induce the water splitting reaction and to decompose organic pollutants. Depending on the reaction path, highly reactive species ($OH\cdot$, O_2^-, H_2O_2) can be created in solution. These reactants are able to decompose and mineralize most of the organic pollutants in solution as well as destroy bacteria [Fuj08]. The main deficiency of titanium dioxide relies on its wide band gap (~3.2 eV) that makes it inefficient for solar-driven applications. However, proper nanostructuration of titanium dioxide and metal-TiO_2 nanocomposites have

been demonstrated able to improve its efficiency, thus making this material an ideal candidate for water purification strategies.

1.2 TiO_2-based photocatalysis

Whatever the application, such as water or air purification, solar energy conversion, water splitting etc., photocatalytic reactions are always the result of complex and concurring processes occurring on the surface at the nanoscale. These processes are [Hof95][Fuj08]: (i) the absorption of light creating electron–hole excitations in a thin layer of a semiconducting compound, (ii) the separation followed by (iii) the transfer of these charges to the surface in contact with water or air, (iv) their interaction with organic or inorganic molecules located on this surface through oxidation and reduction reactions, leading finally (v) the electronic system to recover its ground state.

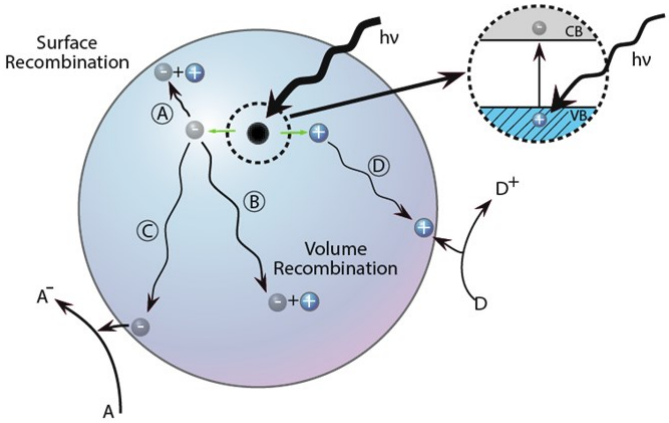

Figure 1.2: Schematic representation of the phenomena taking place in a semiconductor photocatalyst. The photogenerated carriers can recom-bine at a surface trap (A) or in the bulk (B) otherwise they can interact with acceptor (C) or donor (D) species. Adapted from [Lin95].

These processes are sketched in Fig. 1.2. In this figure an energetic photon generates a e^-/h^+ pair. The carriers can recombine at a surface trap (A) or in the bulk (B) otherwise they can interact with acceptor (C) or donor (D) species adsorbed on the surface.

In Fig. 1.3 are reported the valence band (VB) and the conduction band (CB) positions (at pH = 0) for a range of semiconductors on a potential scale (V) versus the normal hydrogen electrode (NHE). Dashed red lines represent the energy levels for the water-splitting half-reactions redox potentials. For the water-splitting reaction to be thermodynamically favorable, the bandgap of the semiconductor photocatalyst should straddle these redox potentials, that is, the CB should have higher energy (more negative potential) than the hydrogen-evolution potential and the VB should be lower in energy (more positive potential) than the oxygen-evolution potential.

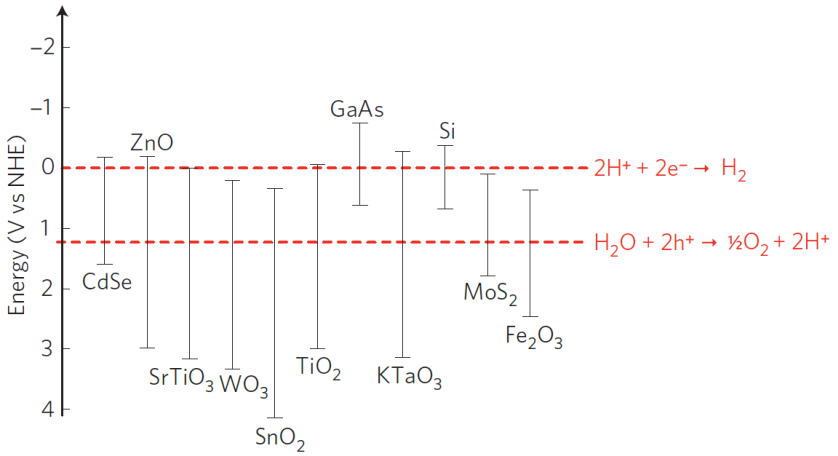

Figure 1.3: VB and CB for a range of semiconductors on a potential scale (V) versus the normal hydrogen electrode (NHE) at pH = 0. Redox potentials for the water-splitting half-reactions versus the NHE are also indicated by dashed red lines. From [Lin11].

Prior to the Honda-Fujishima effect in titanium dioxide [Fuj72], interest in photocatalysis was centered on ZnO, which has similar CB and VB

to TiO_2. The material is, however, limited by intrinsic photocorrosion upon excitation in aqueous media by the photoinduced hole weakening of Zn^{2+}–O^{2-} bonds to produce O_2 and soluble Zn^{2+} [Ger66]. Hematite (α-Fe_2O_3) is another material that was originally thought to be an ideal photocatalyst due to its low cost, abundance, and narrow bandgap for harnessing solar energy (bandgap = 2.0-2.2 eV, excitation wavelength up to 620 nm) [Teo12]. However, the material suffers from rapid charge recombination (lifetime <10 ps) and a short charge carrier diffusion length (2−4 nm) [Teo12]. Tungsten trioxide (WO_3) is another narrow bandgap material (band gap = 2.7 eV) that has received fresh interest. The primary disadvantage of WO_3 lies in its low CB, which is below that required for the single-electron reduction of molecular oxygen [Teo12]. Despite the narrow band gap and the ideal position of VB and CB energy levels with respect to water splitting semi-reactions potentials, CdSe (either in bulk or in quantum dot) is known to be toxic [Der04], thus is not suitable for pollution remediation.

The interest in titanium dioxide as the most studied photocatalytic material remains indisputable. This material has the advantage of being stable, abundant, non-toxic and highly active [Has05][Fuj08][Cho10]. TiO_2 has three main polymorphs [Han11]: rutile (stable), anatase (metastable) and brookite (metastable). These have different activities for photocatalytic reactions, but the precise reasons for differing activities is a matter of debate and have not still been elucidated in detail. The most common studied phases are anatase and rutile. Rutile has three main crystal faces, two that are quite low in energy and are thus considered to be important for practical polycrystalline or powder materials [Ram94]. These are: (110) and (100) (Fig. 1.4 (a) and (b)). The most thermally stable is (110), and therefore it has been the most studied. It has rows of bridging oxygens (connected to just two Ti atoms). The corresponding Ti atoms are 6-coordinate. In contrast, there are rows of 5-coordinate Ti atoms running parallel to the rows of bridging oxygens and alternating with these. The (100) (Fig. 1.4 (b)) surface also has alternating rows of bridging oxygens and 5-coordinate Ti atoms, but these exist in a different geometric relationship with each other.

Anatase has two low energy surfaces, (101) and (001) (Fig. 1.5 (a) and (b)), which are common for natural crystals [Hen00]. The (101) surface, which is the most prevalent face for anatase nanocrystals, is corrugated, also with alternating rows of 5-coordinate Ti atoms and bridging oxygen, which are at the edges of the corrugations. The (001) (Fig. 1.4 (b)) surface is rather flat [Hen00].

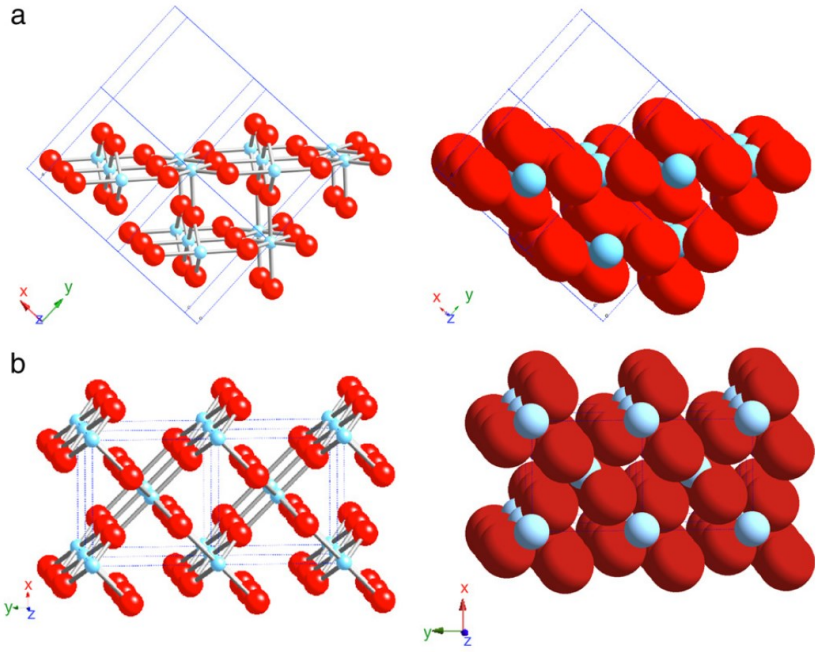

Figure 1.4: Schematic representations of selected low-index faces of rutile: (a) (110) and (b) (100). From [Fuj08].

The commercial standard is the Aeroxide P25® (formerly Degussa P25). The P25 is a powder composed by a mixture of anatase (75%) and rutile (25%) [Ohn01]. There is a large debate in literature claiming whether rutile or anatase is the best phase for photocatalytic reaction [Lut14]. Anatase seems to be more active than rutile [Lut14], even if some studies

suggest that the mixture of the two phases is the best compromise [Sca13]. Moreover, one has to consider that, in view of decontamination strategies, the use of a photocatalyst fixed onto a substrate instead of a powder dispersed in solution may represent a clear advantage. In the work presented in this thesis, we will adopt both strategies: on one hand, we will synthetize and characterize TiO_2 nanoparticles obtained via pulsed laser ablation in liquid; on the other hand, we will elaborate nanostructured TiO_2 thin films. In the first approach we aim to maximize the exposed surface, while in the second we prefer to obtain a photocatalytic film that does not disperse nanomaterial in aqueous solution.

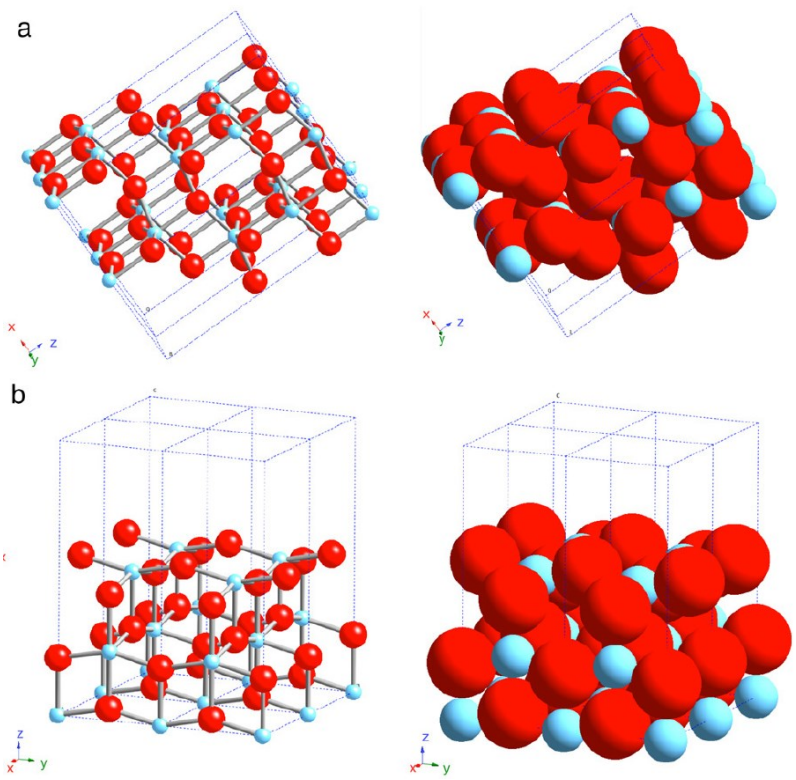

Figure 1.5: Schematic representations of selected low-index faces of anatase: (a) (101) and (b) (100). From [Fuj08].

1.2.1 Principles of photocatalysis

Photocatalysis is generally thought of as the catalysis of a photochemical reaction at a solid surface, usually a semiconductor. This simple definition, while correct and useful, however, conceals the fact that there must be at least two reactions occurring simultaneously, the first involving oxidation, from photogenerated holes, and the second involving reduction, from photogenerated electrons. Both processes must be balanced precisely in order to conserve the charge neutrality and for the photocatalyst itself not to undergo change (which is, after all, one of the basic requirements for a catalyst). In other words, photocatalysis is based on "back-to-back" or short-circuited photoelectrochemical and electro-chemical reactions, balancing electrons and holes [Fuj08]:

$$h\upsilon \rightarrow \mathrm{e}^- + \mathrm{h}^+ \qquad (1.1)$$

$$2\mathrm{H_2O} + 4\mathrm{h}^+ \rightarrow \mathrm{O_2} + 4\mathrm{H}^+ \qquad (1.2)$$

$$\mathrm{O_2} + 4\mathrm{H}^+ + 4\mathrm{e}^- \rightarrow 2\mathrm{H_2O} \qquad (1.3)$$

Because reduction or oxidation by the photoinduced charges of the reacting species involves electron transfer, these redox processes usually occur with species adsorbed to the surface. In competition with the charge carriers transfer processes, recombination takes place, either in bulk or at the surface. Retarding the recombination processes could effectively enhance the photocatalytic activity. Thereby, the presence of trap centers at the surface could extend the life mean time of e^-/h^+ pairs. The typical time scale in photocatalytic reactions is reported in Fig. 1.6.

Even in a perfect crystal one observes the occurrence of a certain number of defects, especially at the surface [Kit08]. In correspondence of these particular locations there will be a trap center for carriers, whose position in the band diagram will depend on the type of defect. Since h^+ are attracted by oxygen atoms in the lattice, while e^- are attracted by Ti, one

can state that defects which influence oxygen or titanium in the lattice correspond to level close to the valence band or close to the conduction band, respectively. Actually, one of the most common defects in TiO_2 surface is represented by an oxygen vacancy [Fuj08]. The Ti^{4+} site left from this vacancy can attract an e^-, thus becoming a Ti^{3+} site. Ti^{3+} on the surface is an ideal site for adsorption of oxygen [Fuj08]. Moreover, when two oxygen vacancies are close to the same Ti site on the surface, then the Ti atom can translate from its position thus becoming an interstitial defect. Interstitial Ti, interacting with the oxygen of the TiO_2 lattice, is a trap for photogenerated holes [Gop10].

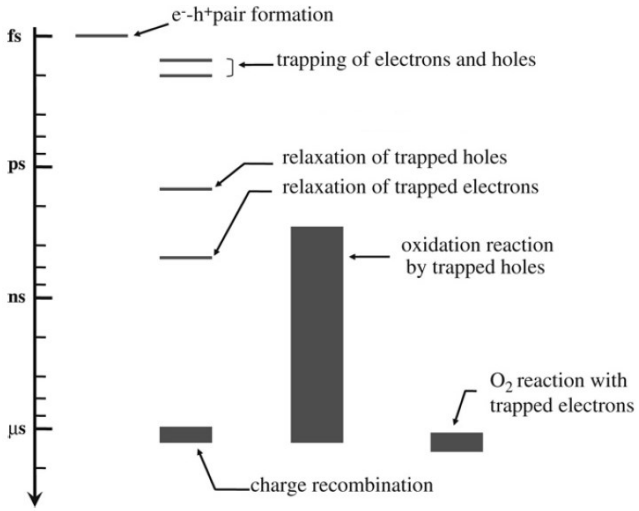

Figure 1.6: Time scale in photocatalysis [Fuj08].

In TiO_2 photocatalysis, surface adsorbed O_2 acts as the primary electron acceptor and no photocatalytic organic degradation is observed to occur in the absence of O_2 [Hof95]. The reduction of O_2 has been demonstrated to be the rate-limiting step in semiconductor photocatalysis [Hof95]. O_2 plays a critical role in enhancing photocatalysis by acting as an electron scavenger, thus reducing e^-/h^+ pair recombination, and forming

highly oxidative species such as H_2O_2. These reactive oxygen species contribute to the oxidation of organic compounds by either directly attacking the organic or by producing hydrogen peroxide, which is a source of hydroxyl radicals that act as a strong oxidizer as shown in:

$$O_2 + 2e^- + 2H^+ \rightarrow H_2O_2 \rightarrow 2HO\cdot \qquad (1.4)$$

In aqueous solutions, several different pathways have been suggested for O_2 reduction. For example, Hoffman suggested that O_2 first adsorbs to the TiO_2 surface before gaining an electron and then combines with two protons to form H_2O_2, which subsequently converts to hydroxyl species that degrade organic compounds [Hof95][Fuj08]. Nakamura suggested two mechanisms for this process; one where an O^- on the TiO_2 surface transfers an electron to an O_2 in solution that then reacts with H^+ to form HO_2^- and eventually H_2O_2; and a second mechanism involving an O_2 in solution that adsorbs to a surface Ti^{4+} site by sequentially accepting two electrons and subsequently reacting with two protons to form H_2O_2, which is released into solution upon addition of the secondH^+[Nak03]. Mattioli *et al.* and Filippone *et al.* both suggested that O_2 accepts two electrons as it adsorbs on the TiO_2 surface and subsequently accepts two protons to form adsorbed H_2O_2, which then desorbs [Mat06][Fil07].

Surface adsorbed water or hydroxide anions act as the main hole acceptors in TiO_2 photocatalysis, although it has been suggested that certain organic materials may be directly oxidized by holes from TiO_2 [Hof95][Fuj08]. Indeed, holes are primarly oxidizing species in photo-catalytic reactions.

Most organic pollutant in water can be decomposed and mineralized on the surface of TiO_2 under UV irradiation. There are, obviously, several factors affecting the mineralization processes: light intensity, pH, ions dispersed in solution, etc. [Fuj08]. TiO_2 Photocatalytic reaction reasonably follow first-order kinetics with respect to the concentration of the organic compound adsorbed, and α order with respect to light intensity [Hof95]:

$$r = k\Gamma I^{\alpha} \qquad (1.5)$$

where r is the reaction rate, k the first-order constant, Γ the concentration for surface unity and I the light intensity. At high intensity $0 < \alpha < 1$, while at low intensity $\alpha = 1$.

1.2.2 Photocatalytic test

There are a large and growing number of research groups and industries associated with semiconductor photocatalysis. Thus, it appears obvious the necessity of a methodology that allows at the same time to evaluate the photocatalytic performance of a material and to compare it with the results obtained elsewhere. In this sense, standards help researchers as well as manufacturers to develop and deliver products which have the defined characteristics. However, how the activity of a given photocatalyst sample can be represented by a single test method is not an easy task. Indeed, it is known the fact that the activity of a photocatalyst depends on how it is measured limits the general applicability of a specific test method [Ryu08].

Nonetheless, methylene blue (MB) discoloration test has become one of the most popular method for assessing photocatalytic activity of titania films and powders [Mil07][Mil12]. This methodology has been developed for the determination of photocatalytic activity of surfaces in an aqueous medium by degradation of methylene blue (ISO 10678:2010 [ISO10]), by International Organization for Standardization (ISO) [ISO15]. Using this method it is possible to extract the reaction constant rate for a certain material. To do so, a sample is immersed in a MB-water solution and irradiated by UV (or visible) light. By measuring the dye concentration as a function of time one can evaluate the photocatalytic activity relative to the sample. In Fig. 1.7 is sketched the experimental set up for the test. Usually the sample is placed at the bottom of a cylindrical vessel filled with MB-

water solution. The solutions is left for a certain time in dark to allow the adsorption of MB onto sample and vessel surfaces and then illuminated. During light irradiation the vessel is covered with quartz in order to avoid evaporation during irradiation. Two important indications of the standard refer to the ideal concentration of the MB solution (about 10^{-5}M, showing an absorbance value of about 1.0-1.2) and to the intensity of the external irradiation (~1 mW/cm^2). In fact, both these parameters can strongly affect the activity evaluation.

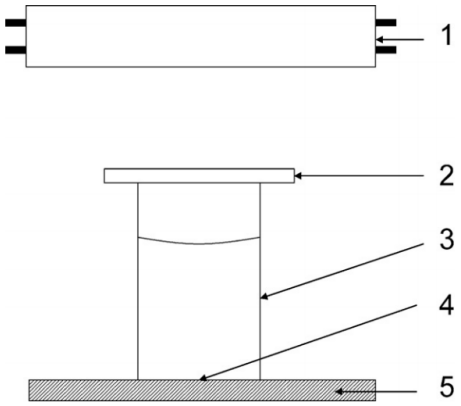

Figure 1.7: Irradiation set up for the methylene blue standard, com-prising: (1) UV light source, (2) cover glass, (3) testing cylinder, (4) testing area and (5) sample under test. From [Mil12].

Actually, during the test, one measures the absorbance of the MB solution at the wavelength of 664 nm and relates it to the concentration according to the Lambert-Beer law:

$$A = C\epsilon x \qquad (1.6)$$

where A is the absorbance, C is the dye concentration, ϵ is the molar extinction coefficient (for MB at 664 nm $\epsilon_{MB}^{664} = 7.4 \cdot 10^4 \mathrm{M}^{-1}\mathrm{cm}^{-1}$) and x is the optical path length. Since in the experimental set up all the

parameters stay constant apart from the MB concentration, it is possible to extract the discoloration rate measuring the absorbance of the solution that is undergoing to photocatalytic reactions. As a matter of fact, one refers to the initial concentration C_0 thus measuring the variation $\frac{C}{C_0} = \frac{A}{A_0}$. Moreover, it is assumed that the reaction occurs according to a first order exponential law:

$$C = C_0 e^{(-kt)} \Rightarrow \ln\left(\frac{C}{C_0}\right) = -kt \qquad (1.7)$$

being k the reaction rate constant and t the time.

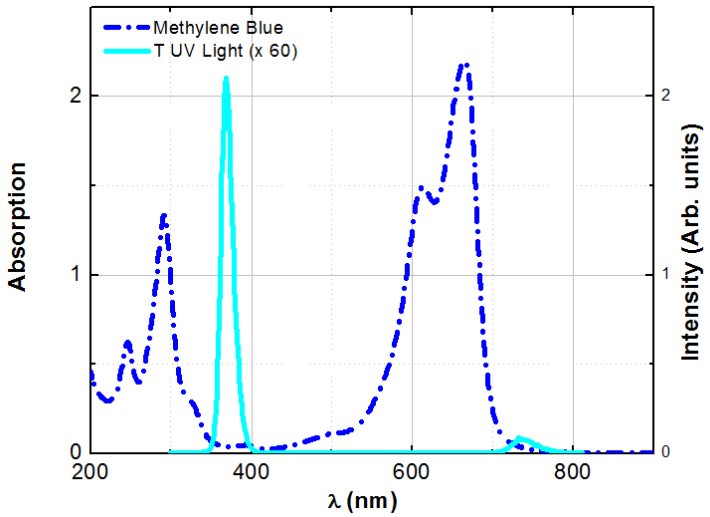

Figure 1.8: Absorbance spectra of a MB (dark blue dash-dot line, left y scale) and emission spectra of the UV lamp used for the photocatalytic test (light blue line, right y scale).

The reason why the wavelength of 664 nm is chosen is easily understandable looking at the typical absorption spectra of MB. In Fig. 1.8 is reported the MB absorption spectra together with the irradiance spectra of

the UV lamp used for photocatalytic tests (TL 8 W BLB 1FM, Philips). The absorption spectrum of MB has two peaks, one at 664 nm and the other one at about 610 nm. While the first one is related to monomer absorption, the second one is related to the dimer [Liu12]. Thus, one records the absorption at the wavelength corresponding to the monomer concentration, i.e. 664 nm. In Fig. 1.9 are reported the absorbance measurements related to a test on Degussa P25 titania powder. It is clear that the concentration of MB decreases under illumination. This results evident from Fig. 1.10 where are reported the absorbance value of MB solution at 664 nm versus time, for different concentration of TiO_2 powder.

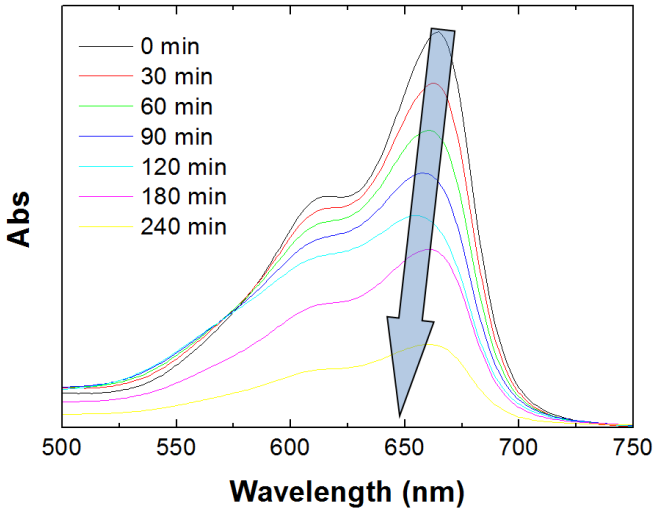

Figure 1.9: Absorbance spectra of a MB solution irradiated with UV light versus time. The solution contains Degussa P25 titania powder.

In our following experimental consideration we will adopt this methodology in order to evaluate the photoactivity of the elaborated samples.

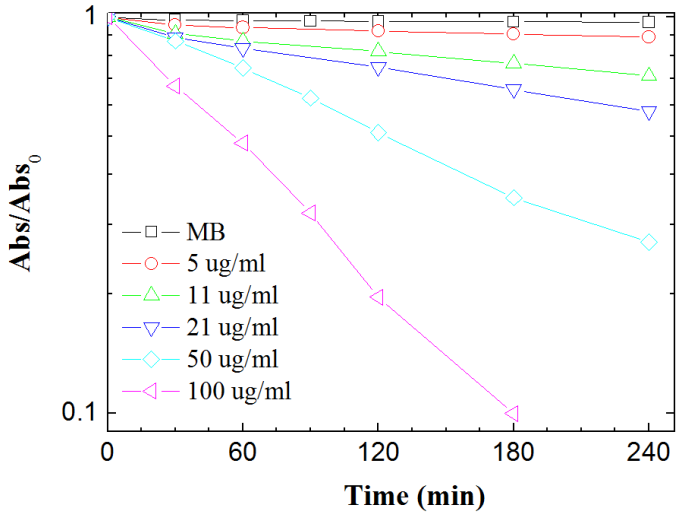

Figure 1.10: Absorbance value of MB solution at 664 nm versus time, for different concentration of TiO_2 powder.

1.3 Plasmonic metal-TiO_2 nanocomposites

Due to its wide band-gap, TiO_2 (either rutile or anatase) absorbs only in the UV range of the electromagnetic spectrum. However, sunlight contains a small amount of UV photons (~5%). Thus, in the last 20 years have been developed several strategies devoted to increase the efficiency of titanium dioxide under visible (solar) irradiation. Among the most extensively studied methods we cite the doping with N [Asa01], transition metals [Lit99] and C [Kha02], the coupling with a narrow band-gap semiconductor quantum dots [Rob06], the preparation of oxygen-deficient and/or hydrogen-rich TiO_x [Che11][Che15] and the use of plasmonic metal nanostructures [Lin11][Hou13].

We are interested, in particular, in this last approach. Plasmonics exploits the physics of collective oscillations of free electrons in metals, induced by the interactions with electromagnetic radiation. Incident light

can be either coupled to the metal-dielectric interface in a form of propagating Surface Plasmon Polariton (SPP) waves, or confined in the nanoscale metallic structures at Localized Surface Plasmon Resonance (LSPR) [Mai07][Nov06]. While SPPs are partially propagative (2D or 1D) plasmonic modes, LSPRs are completely localized modes (0D). When an electromagnetic wave hits a metal nanoparticle, one observes a scattered field whose composition can be split into two components: the far-field and the near-field. The first regards the propagation of the scattered wave, while the second regards an evanescent field localized few nm close to the metal nanostructure surface [Nov06]. In the following we will discuss LSPR and the effects of coupling plasmonic metal nanostructures with TiO_2.

1.3.1 Localized Surface Plasmon Resonance (LSPR)

LSPRs are non-propagating excitations of the conduction electrons of metallic nanoparticles in an oscillating electromagnetic field. As schematically shown in Fig. 1.11 the interactions with a fixed background of positively charged ion cores gives a restoring force on the driven electrons so that a resonance can arise, leading to field amplification both inside and in the near-field zone outside the particle. The model is similar to that of a damped harmonic oscillator.

Since the conduction electrons in metals have nearly a continuum of available states, the optical properties of metals can be explained by a classical Drude model of free-electron gas moving against crystal lattice of positive ions [Gre98]. In the model, the details of lattice potential are approximated by an effective mass of electrons *m*, while the electron-electron and electron-phonon interactions, as well as scattering on lattice defects or grain boundaries, are described by damping occurring with a characteristic frequency γ with typical values on the order of 10^{14} s^{-1} at room temperature. Within the Drude-Lorentz model, the dielectric function of a metal can be approximated as:

$$\varepsilon(\omega) = 1 - \frac{\omega_p^2}{\omega^2 + i\gamma\omega} \tag{1.8}$$

where $\omega_p = \frac{ne^2}{\varepsilon_0 m}$ is the plasma frequency of the electron gas, depending on the electron density n.

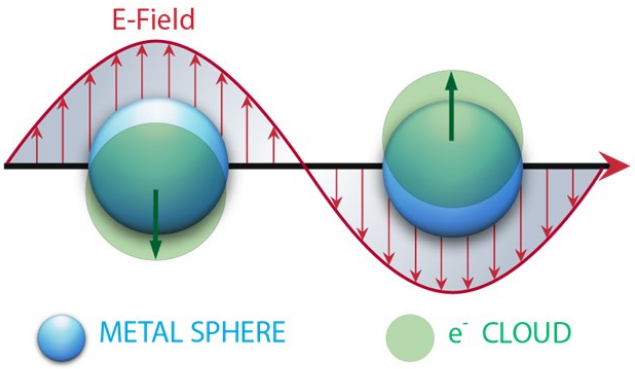

Figure 1.11: Schematic of plasmon oscillation for a sphere, showing the displacement of the conduction electron charge cloud relative to the nuclei.

If we assume that the dimension of the metallic nanoparticle is much smaller than the wavelength of the exciting radiation, i.e. $d \ll \lambda$, than the phase of harmonic electromagnetic field is nearly constant over the particle volume. Under this hypothesis, the charges in the nanoparticle will feel a static electromagnetic field. Therefore, the scattering problem can be simplified to a particle in an electrostatic field, known as quasi-static approximation [Mai07].

Consider a homogeneous spherical particle having radius a and complex dielectric function $\varepsilon = \varepsilon(\omega)$, embedded in an isotropic and non-absorbing medium having dielectric constant ε_m. Assume that the particle is immersed in an electrostatic field $\mathbf{E} = \mathrm{E}_0\hat{z}$. These hypothesis are sketched in Fig. 1.12. The light scattering problem is addressed by solving the Laplace equation for potential ϕ:

$$\nabla^2\phi = 0 \qquad (1.9)$$

from which one can calculate the electric field:

$$\mathbf{E} = -\nabla\phi \qquad (1.10)$$

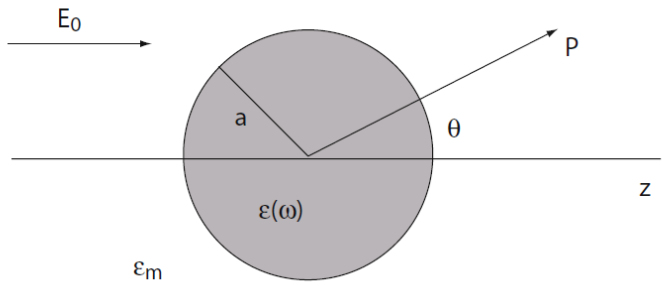

Figure 1.12: Sketch of a homogeneous sphere placed into an electrostatic field.

Due to the azimuthal symmetry of the problem, the general solution is of the form:

$$\phi(r,\theta) = \sum_{l=0}^{\infty}\left[A_l r^l + B_l r^{-(l+1)}\right] P_l(\cos\theta) \qquad (1.11)$$

where $P_l(\cos\theta)$ are the Legendre Polynomials of order l, and θ is the angle between the position vector $\boldsymbol{r}$ at the z-axis. The coefficients A_l and B_l are determined from the boundary conditions: (i) at $r \to \infty$and (ii) from equality of potentials, tangential components of the electric field, and normal components of the displacement field at $r = a$ (sphere surface).
Without presenting the detailed calculations [Jac99], the potentials inside ϕ_{in} and outside ϕ_{out} the sphere can be written as:

$$\phi_{in} = -\frac{3\varepsilon_m}{\varepsilon + 2\varepsilon_m} \mathrm{E}_0 r\cos\theta \tag{1.12}$$

$$\phi_{out} = -\mathrm{E}_0 r\cos\theta + \frac{\mathbf{p}\cdot\mathbf{r}}{4\pi\varepsilon_0\varepsilon_m r^3} \tag{1.13}$$

being ε_0 the dielectric constant in vacuum and $\mathbf{p}$ the dipole moment, defined as:

$$\mathbf{p} = \varepsilon_0\varepsilon_m\alpha\mathbf{E}_0 \tag{1.14}$$

introducing the polarizability α:

$$\alpha = 4\pi a^3 \frac{\varepsilon - \varepsilon_m}{\varepsilon + 2\varepsilon_m} \tag{1.15}$$

Fig. 1.13 shows the absolute value and phase of α with respect to frequency ω (in energy units) for a dielectric constant varying as $\varepsilon(\omega)$ of the Drude form (equation 1.8), in this case fitted to the dielectric response of silver [Mai07]. It is apparent that the polarizability experiences a resonant enhancement under the condition that $|\varepsilon + 2\varepsilon_m|$ is a minimum, which for the case of small or slowly-varying $\mathrm{Im}\{\varepsilon\}$ around the resonance simplifies to:

$$\mathrm{Re}\{\varepsilon(\omega)\} = -2\varepsilon_m \tag{1.16}$$

This relationship is called the Fröhlich condition and the associated mode (in an oscillating field) the *dipole surface plasmon* of the metal nanoparticle. For a sphere consisting of a Drude metal with a dielectric function (1.8) located in air, the Fröhlich criterion is met at the frequency $\omega_0 = \omega_p/\sqrt{3}$. Condition (1.16) further expresses the strong dependence of the resonance frequency on the dielectric environment: the resonance redshifts as ε_m is increased.

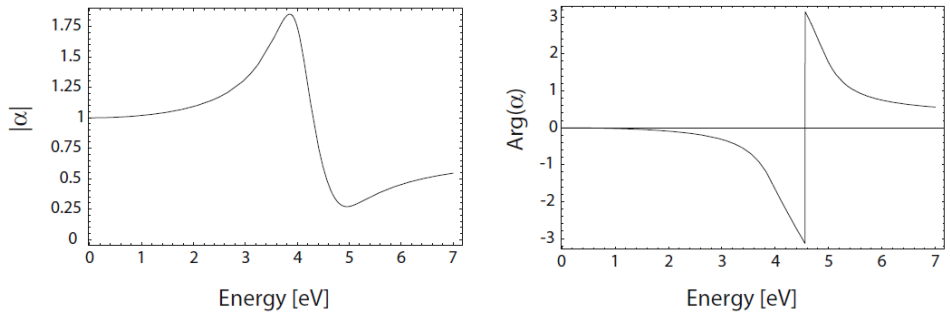

Figure 1.13: Absolute value and phase of the polarizability α (1.15) of a sub-wavelength metal nanoparticle with respect to the frequency of the driving field (expressed in eV units). Here, $\varepsilon(\omega)$ is taken as a Drude fit (equation 1.8) to the dielectric function of silver from [Joh72]. Taken from ref. [Mai07].

From the potential (1.12) and (1.13) it is possible to calculate the electric field:

$$\mathbf{E}_{in} = \frac{3\varepsilon_m}{\varepsilon + 2\varepsilon_m}\mathbf{E}_0 \tag{1.17}$$

$$\mathbf{E}_{out} = \mathbf{E}_0 + \frac{3\mathbf{n}(\mathbf{p}\cdot\mathbf{n}) - \mathbf{p}}{4\pi\varepsilon_0\varepsilon_m r^3} \tag{1.18}$$

where $\mathbf{n}$ is the unit vector in the direction of the point of interest. As expected, the resonance in α also implies a resonant enhancement of both the internal and dipolar fields. It is this field-enhancement at the plasmon resonance the peculiar characteristic of metal nanoparticle.

The above considerations demonstrate that in the quasi-static approximation ($a \ll \lambda$) a metal nanoparticle can be represented as an ideal dipole. Thus, we can extend the model in the case of time-varying fields, neglecting spatial retardation effects over the particle volume. From the viewpoint of optics, it is worth noting that another consequence of the resonantly enhanced polarization α is a concomitant enhancement in the efficiency with which a metal nanoparticle scatters and absorbs light. The

corresponding scattering and absorption cross sections, calculated via the Poynting vector, are given by [Mai07][Boh83]:

$$\sigma_{sca} = \frac{k^4}{6\pi}|\alpha|^2 = \frac{8\pi}{3}k^4a^6\left|\frac{\varepsilon - \varepsilon_m}{\varepsilon + 2\varepsilon_m}\right|^2 \qquad (1.19)$$

$$\sigma_{abs} = k\mathrm{Im}\{\alpha\} = 4\pi ka^3\mathrm{Im}\left\{\frac{\varepsilon - \varepsilon_m}{\varepsilon + 2\varepsilon_m}\right\} \qquad (1.20)$$

where $k = \frac{2\pi}{\lambda}$ is the wavenumber.

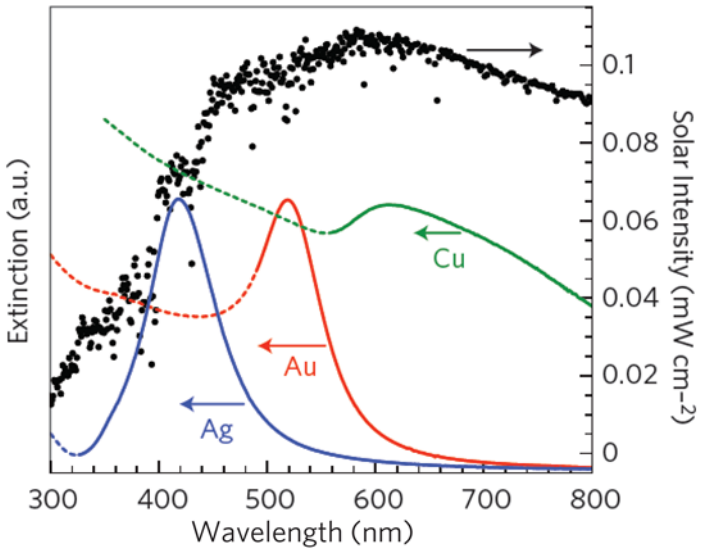

Figure 1.14: Simulated normalized extinction spectra of spherical Ag (38 nm diameter), Au (25 nm), Cu (133 nm); in black the intensity of solar spectrum. From ref. [Lin11].

For noble metals, silver and gold, in air the resonance is observed in the visible region of the electromagnetic spectrum. Indeed, the wavelength (energy) at which plasmon resonance occurs strongly depends on the

metal. At a fixed electron density (i.e. for a certain metal), the plasmon resonance peak depends on the shape and on the dimension of the nanostructure [Kel03][Moc02][Nog07]. In fig 1.14 are reported the simulated extinction spectra ($\sigma_{ext} = \sigma_{sca} + \sigma_{abs}$) for nanoparticles composed by Ag (blue), Au (red) and Cu (green). Note that the peak position changes for each metal. Moreover, one observes, especially for Au and Cu, a high value of the extinction for lower wavelengths (dashed lines) due to intraband transitions.

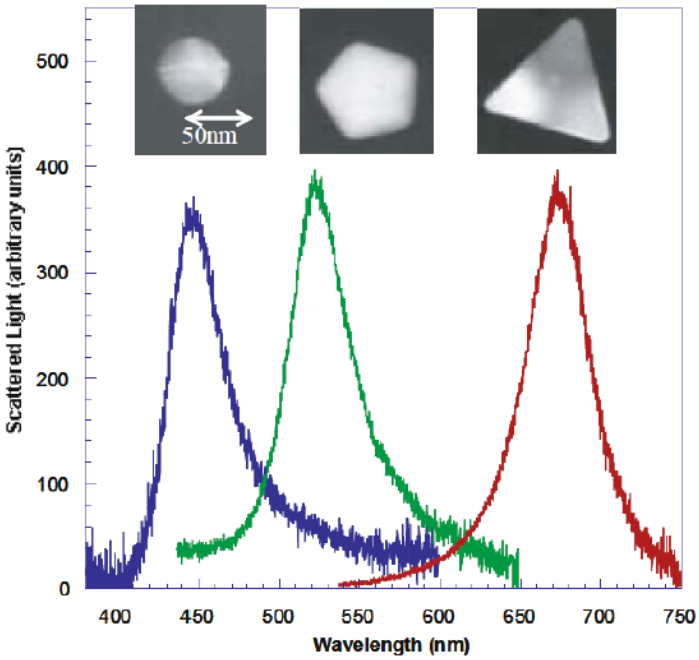

Figure 1.15: Experimental optical spectroscopy measurements of individual silver nanoparticles having different shapes. From ref. [Moc02].

In Fig. 1.15 are shown the experimental data for Ag nanostructures having different shapes. In general, it is not obvious to predict how a certain shape will influence the position of the resonance peak.

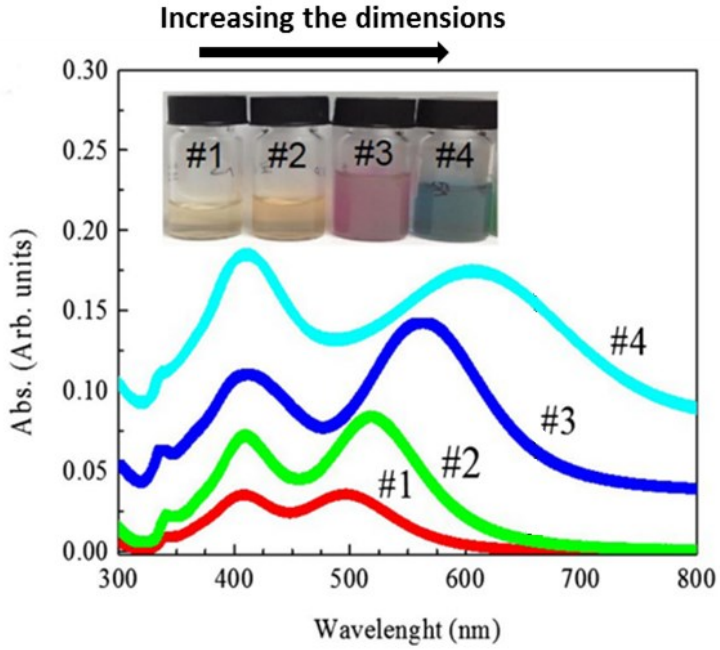

Figure 1.16: UV–Vis spectra of different Ag nanoplatelet solutions. The nanoplatelets have a transversal size of 20 nm and a longitudinal length in the range 65–92 nm (growing from sample #1 to sample #4). In the inset, a photographs of the corresponding solutions are shown. From ref. [Zim15].

However, asymmetric and complex shapes can reveal several resonances, depending on the polarization of incident light [Kel03][Zim15]. In Fig. 1.16 are reported the UV-Vis spectra of Ag nanoplatelets whose transversal size is fixed (20 nm) while the longitudinal length varies in the range between 65 nm and 92 nm [Zim15]. This data are interesting since it is possible to observe two resonance peaks. The first one, located at about 400 nm, is fixed for all the samples and is related to the transversal size of the nanostructures. The second one redshifts from about 500 nm to about 650 nm and, at the same time, broadens as the longitudinal dimension increases.

Two mechanisms occur as the nanostructure size increases: a redshift and a broadening of the resonance peak [Cat08]. The first one is due to the *dynamic depolarization*: increasing particle dimensions, conduction electrons no longer move in phase, reducing the depolarization field and thus the restoring force, causing a redshift of the resonance. The second one is due the *radiative damping*: as scattering becomes significant, this re-radiation leads to a radiative damping correction to the quasi-static polarizability, the effect of which is to significantly broaden the plasmon resonance. Taking into account these effects, the polarizability will take the form [Mei83]:

$$\alpha \approx \frac{1-\frac{1}{10}(\varepsilon+\varepsilon_m)x^2}{\left(\frac{1}{3}+\frac{\varepsilon_m}{\varepsilon-\varepsilon_m}\right)-\frac{1}{30}(\varepsilon+10\varepsilon_m)x^2-i\frac{4\pi^2\varepsilon_m^{3/2}}{3}\frac{V}{\lambda_0^3}}V \qquad (1.21)$$

with $x=\frac{\pi a}{\lambda}$ is a size parameter. Comparing this equation with (1.15), one notes several new terms. In particular, the term x^2 in the numerator accounts for retardation effects of the exciting field on the volume of the particle, causing a shift of the resonance. The same effect has the term x^2 in the denominator, this time due to retardation in the depolarized field. For noble metals (and also for Drude metals) the total shift occurs towards lower energies (longer wavelengths). This is qualitatively explainable since in bigger particles there will be a greater distance among the charges at the opposite sides of the particles. This translates in a smaller resting force and thereby to lower resonance energy. The term in i in the denominator of equation (1.21) takes into account the radiative damping coming from electrons oscillations [Kok72]. This phenomena is the main responsible for the broadening of the plasmon peak with the increase of particles size.

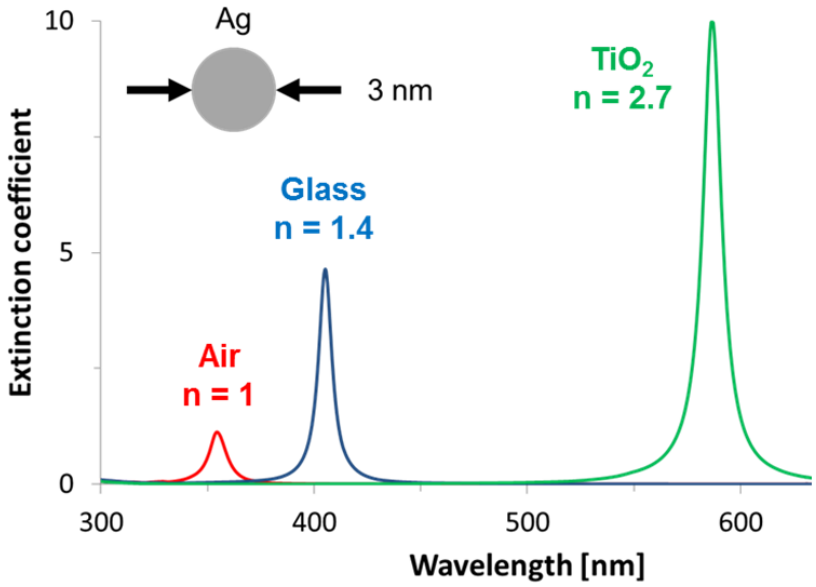

Figure 1.17: Simulation of the extinction spectra versus wavelength of a silver sphere having diameter of 3 nm immersed in air (red), glass (blue) or TiO_2 (green). The refractive index at the resonance peak wavelength of each medium is also reported.

The red-shift and broadening of the resonance with increased nanoparticle size would generally be expected to be an advantage for solar-driven applications, since it translates in an enlarged absorption of the visible spectrum.

As already pointed out, the dielectric constant of the embedding medium also dramatically influences the plasmon resonance and its quality factor [Kel03]. In Fig. 1.17 are reported the simulations of the extinction spectra of a silver sphere having diameter of 3 nm immersed in air (refractive index $n = 1$), glass ($n = 1.4$) or TiO_2 ($n = 2.7$). The simulations clearly show how the plasmon peak shifts to higher wavelengths (lower energies) as the refractive index increases. At the same

time, one observes an increasing of the quality factor of the resonance, due to a higher confinement of the electric field.

1.3.2 Field enhancement in metal gaps

As previously mentioned, in the neighboring of the plasmonic metal nanoparticle one observes a high enhancement of the electromagnetic field, in particular during the occurrence of a LSPR. Such a high rise in the intensity of the field can, in principle, lead to non-linear effects both in the metal particle and in the embedding matrix. In Fig. 1.18 is reported the simulated magnitude of the electromagnetic field in the vicinity of a silver nanocube of diameter 75 nm, at a wavelength of λ = 420 nm matching the plasmon resonance [Lin11]. The field intensity is redistributed leading to a region where the field enhancement reaches a factor up to 10^3 times the incident intensity.

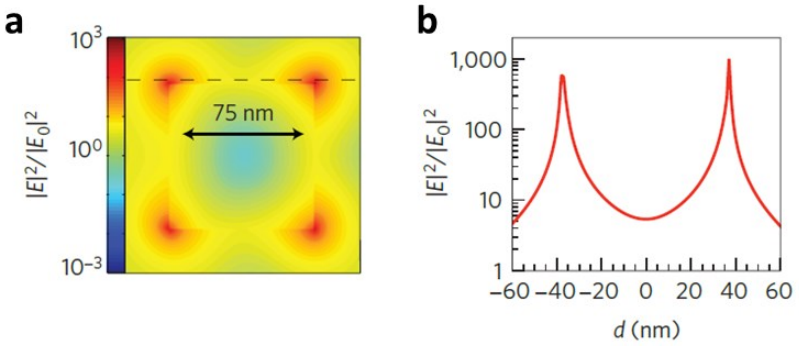

Figure 1.18: a) Spatial distribution of the SPR-induced enhancement of electric field intensity at the SPR peak wavelength (420 nm), from a FDTD simulation of a 75 nm Ag nanocube. b) Enhancement in the electric field intensity at the SPR peak wavelength as a function of distance *d* along the dashed line indicated in a). Taken from ref. [Lin11].

The field enhancement is particularly strong inside metal gaps, i.e. in the space between two metal nanostructures close (few nm) each other [Pav13]. As an example, in fig 1.19 is shown the calculated maximum enhancement in the electric field intensity as function of distance between two Ag cubic particles [Lin11]. Remarkably, in this case the enhancement reaches a factor up to 10^4 for very close nanostructures.

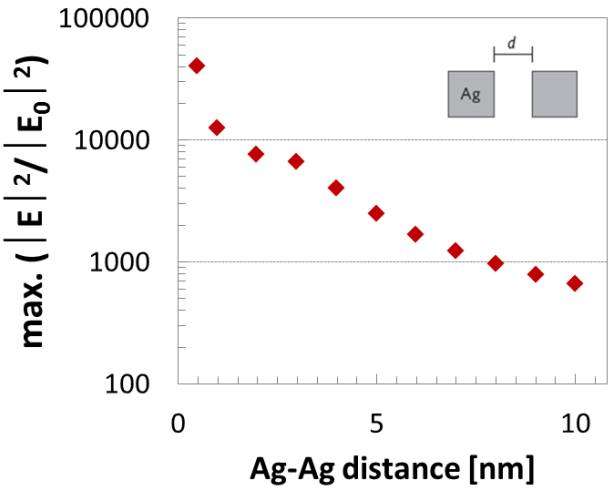

Figure 1.19: Maximum enhancement in the electric field intensity as function of distance between two Ag particles, calculated from a series of finite-difference time-domain (FDTD) simulations. Data taken from ref. [Lin11].

1.3.3 Metal-TiO_2 nanocomposites

As previously mentioned, one of the main deficiency of TiO_2 relies on its wide band-gap. In order to enhance the material efficiency in the visible range of the electromagnetic spectrum, surface-plasmon mediated photocatalytic activity of TiO_2 has become a hot research topic [Awa08] [Sta09][Lin11][Che12][Hou13][Zha13][Dah14][Liu14].

As depicted in Fig. 1.20, metal nanostructures in presence of an external exciting electromagnetic field can interact with a photoactive substrate at least in three different ways [Nov06][Bha09]:

A. the far-field component of the scattered field will induce a prolonged optical path for photons and thereby will increase the probability of absorption within the semiconductor substrate;
B. the near-field component of the field can cause locally enhancement of the field intensity in the vicinity of the nanostructure, thus leading to non-linear effects as well as local heating effects;
C. as a consequence of the metal-semiconductor junction, a direct injection of photoexcited carriers into the substrate can occur as well as a charge separation process due to the Schottky barrier [Sze07].

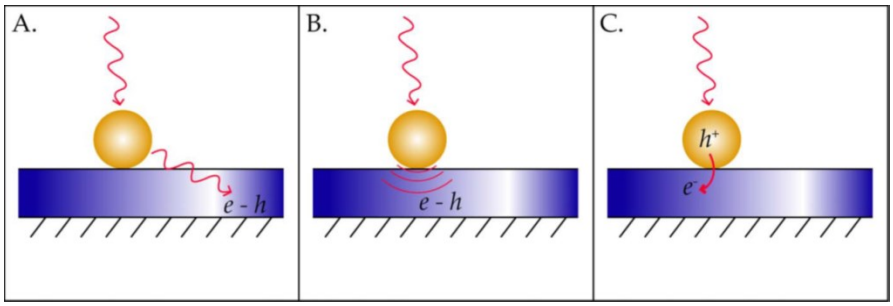

Figure 1.20: Schematic of different interactions between a metal nanoparticle and a photoactive substrate: (A) far-field scattering, (B) near-field scattering, and (C) direct injection of photoexcited carriers into the semiconductor. From ref. [Bha09].

For photocatalysis, the last two effects are particularly important. The advantage of the formation of e^-/h^+ pairs, close to the semiconductor surface, is that these charge carriers are readily separated from each other and easily migrate to the surface, where they can perform photocatalytic transformations.

Experimental evidences of the improvement in the photocatalytic activity under visible irradiation have been recently reported [Awa08] [Ing11][Lin11][Liu11][Hou13]. In Fig. 1.21 is reported the comparison between oxygen and hydrogen evolution from solution of Ag-TiO_2 and bare TiO_2 nanocomposites upon illumination with a broadband visible source (400-900 nm, ~500 mW/cm^2, spectral peak at 580 nm) [Ing11]. The solution was prepared mixing a colloidal solution of Ag nanocubes with nitrogen-doped TiO_2 (N-TiO_2) solution. The composite was 5% metal by weight. The presence of silver nanostructures is responsible for the enhancement in the activity of the photocatalyst through charge injection. According to this model, electrons near the metal Fermi level E_f are excited to surface plasmon (SP) states; then, after the relaxation of the plasmon oscillations, some electron can transfer to the nearby semiconductor and, at this point, activate electron-driven processes such as the hydrogen-evolution half-reaction [Lin11] [Gov14](Fig.1.22).

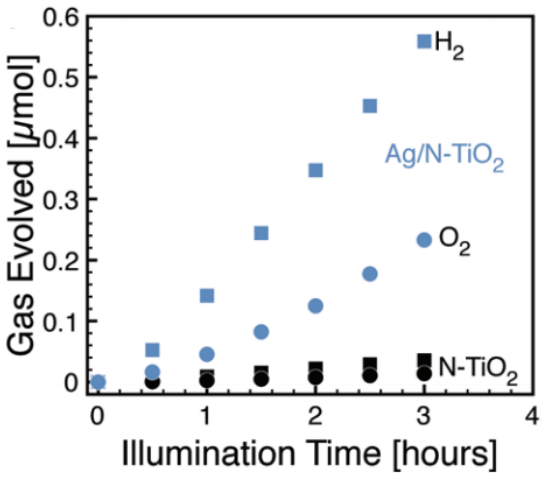

Figure 1.21: H_2 (squares) and O_2 (circles) production upon visible illumination of N-TiO_2 (black symbols) and Ag/N-TiO_2 (blue symbols) photocatalysts, as measured by mass spectrometry. From ref. [Ing11].

In another experiment conducted by Liu *et al.* [Liu11], the enhancement in the photoactivity of an Au-TiO_2 nanocomposite film is explained in terms of the local electric field enhancement near the TiO_2 surface, rather than by the direct transfer of charge between the two materials. According to the authors, in this case the near-field optical enhancement increases the electron-hole pair generation rate at the surface of the TiO_2. In Fig. 1.23 (a)-(d) are reported the FDTD simulations on the 5 nm thick Au film onto TiO_2 substrate, showing the presence and distribution of region of high electromagnetic field intensity (*hot spots*) within metal gaps. In Fig. 1.23 (e)-(f) are reported the experimental photocurrent measurements emphasizing the better performance of the Au-TiO_2 composite film in the spectral range of interest for LSPR in gold (red region of the visible spectra).

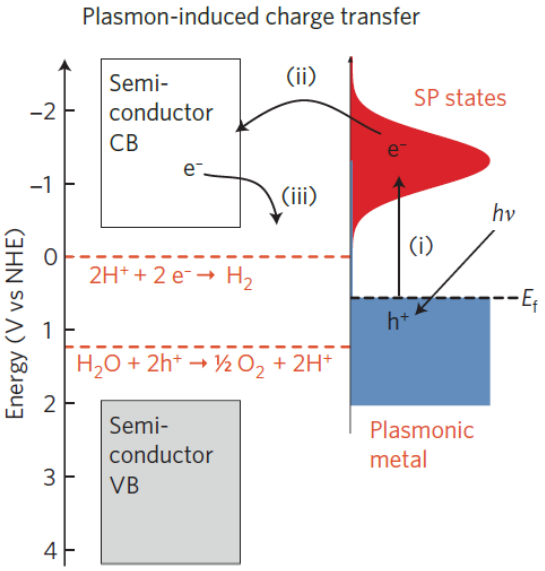

Figure 1.22: Mechanism of SPR-induced charge transfer with approximate energy levels on the NHE scale. Dashed red lines refer to the water-splitting redox potentials (see Fig. 1.3). From ref. [Lin11].

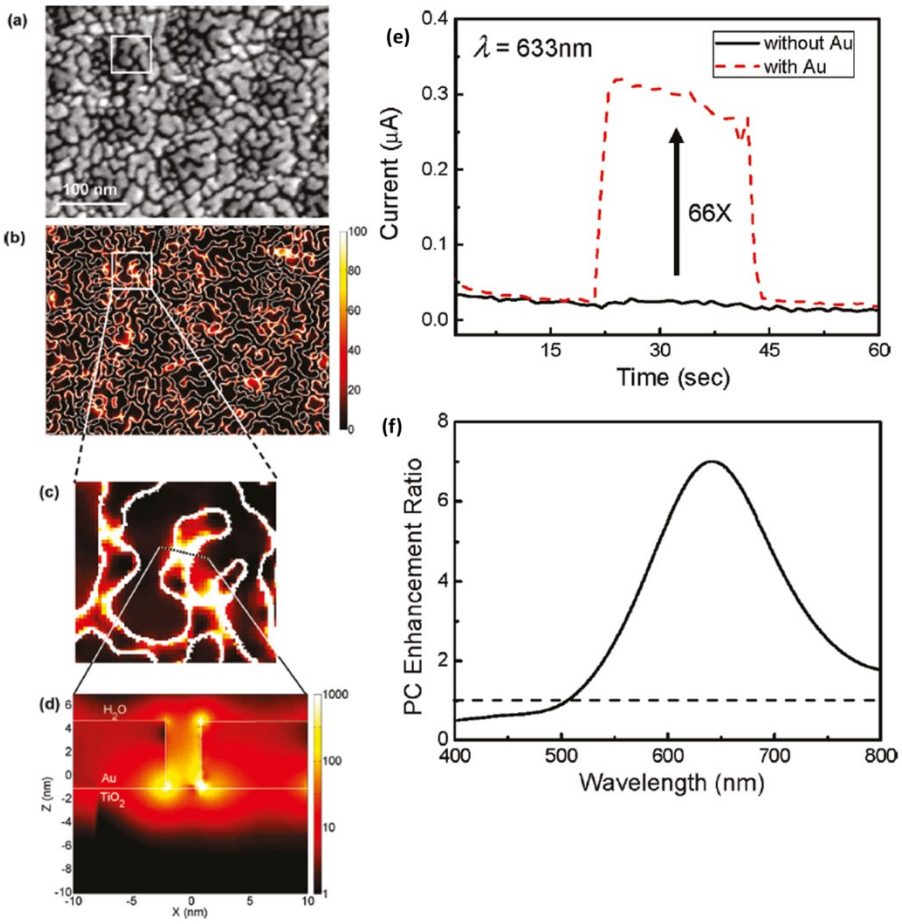

Figure 1.23: On the left, (a) SEM image of a 5 nm thick Au island film on TiO_2; FDTD simulated electric field intensity, in the plane xy (b,c) and in a vertical section (d). On the right, (e) photocurrent of anodic TiO_2 with and without Au nanoparticles irradiated with λ = 633 nm light for 22 s; (f) photocurrent enhancement ratio spectrum; the dashed line refers to the bare TiO_2 (value 1). From ref. [Liu11].

However, it has been also proposed a photocatalytic reaction directly on the surface of the plasmon excited metal nanoparticle [Chr11][Zha13][Gov14].In this picture, excited NPs inject hot electrons to

the states (orbitals) of the adsorbed species (reactants). It is a process similar to charge injection but without the mediation of the semiconductor material.

Whatever the process involved, it seems clear that the presence of metal nanostructures can effectively improve the efficiency under visible (solar) irradiation.

1.4 Conclusion

TiO_2-based photocatalysis appears to be a promising technology for a number of applications such as air purification, hazardous waste remediation and water treatment and disinfection. Indeed, in the framework of environmental friendly and sustainable technologies, solar-driven photocatalysis rises as ideal candidate for such a purpose. Towards the development of green photocatalysts, metal-TiO_2 nanocomposites appear as the ideal candidates for green remediation technology.

1.5 References

[Asa01] R. Asahi, T. Morikawa, T. Ohwaki, K. Aoki, Y. Taga, Science, **293**, 269 (2001).

[Atw10] H. A. Atwater, A. Polman, Nature Materials **9**, 205–213 (2010).

[Awa08] K. Awazu, M. Fujimaki, C. Rockstuhl, J. Tominaga, H. Murakami, Y. Ohki, N. Yoshida, T. Watanabe, J. Am.Chem. Soc., **130**, 1676–1680 (2008).

[Bha09] P. Bharadwaj, B. Deutsch, L. Novotny, Adv. Opt. Photonics, **1**, 438–483 (2009).

[Boh83] C. F. Bohren; D. R. Huffman, *Absorption of Light by Small Particles*, Wiley: New York, 1983.

[Cat08] K. R. Catchpole, A. Polman, OPTICS EXPRESS, **16** (26), 21793 (2008).

[Che11] X. Chen, L. Liu,P. Y. Yu, S. S. Mao, Science, **331**, 746 (2011).

[Che12] K.-H. Chen, Y.-C. Pu, K.-D. Chang, Y.-F. Liang, C.-M. Liu, J.-W. Yeh, H.-C. Shih, Y.-J. Hsu, J. Phys. Chem. C, **116**, 19039–19045 (2012).
[Che15] X. Chen, L. Liu, F. Huang, Chem. Soc. Rev., **44**, 1861 (2015).
[Cho10] M. N. Chong, B. Jin, C. W.K. Chow, C. Saint, Water research, **44**, 2997-3027 (2010).
[Chr11] P. Christopher, H. Xin, S. Linic, Nature Chemistry, **3**, 467–472 (2011).
[Dah14] M. Dahl, Y. Liu, Y. Yin, Chem. Rev., **114**, 9853–9889 (2014).
[Der04] A. M. Derfus, W. C. W. Chan, S. N. Bhatia, Nano Letters, **4**(1), 11–18 (2004).
[Fil07] F. Filippone, G. Mattioli, A. A. Bonapasta, Catal. Today, **129**, 169−176 (2007).
[Fuj08] A. Fujishima, X. Zhang, D. A. Tryk, Surf. Sci. Rep., **63**, 515-582 (2008).
[Fuj72] A. Fujishima, K. Honda, Nature, **238**, 37-38(1972).
[Ger66] H. Gerischer, J. Electrochem. Soc., **113**, 1174−1182 (1966).
[Gov14] A. O. Govorov, H. Zhang, H. V. Demir, Y. K. Gun'ko, Nano Today, **9**, 85-101(2014).
[Gre98] W. Greiner, *Classical Electrodynamics*, Springer, New York (1998)
[Gop10] N. O. Gopal, H.-H. Lo, S.-C. Sheu, S.-C. Ke, J. Am. Chem. Soc., **132**, 10982–10983 (2010).
[Han11] D. A. H. Hanaor, C. C. Sorrell, J. Mater. Sci. , **46**, 855-874 (2011).
[Has05] K. Hashimoto, H. Irie, A. Fujishima, Jpn. J. Appl. Phys., **44**, 8269-8285 (2005).
[Hen00] R. Hengerer, B. Bolliger, M. Erbudak, M. Grätzel, Surf. Sci., **460**, 162–169 (2000).
[Hof95] M. R. Hoffmann, S. T. Martin, W. Choi, D. W. Bahnemann, Chem. Rev., **95**, 69-96 (1995).
[Hou13] W. Hou, S. B. Cronin, Adv. Funct. Mater., **23**,1612–1619 (2013).
[Jac99] J. D. Jackson, *Classical Electrodynamics*, John Wiley & Sons, Inc., New York, NY, 3rd edition (1999).
[Joh72] P. B. Johnson, R. W. Christy, Phys. Rev. B, **6**(12), 4370–4379 (1972).
[Kel03] K. L. Kelly, E. Coronado, L. L. Zhao, G. C. Schatz, J. Phys. Chem. B, **107**, 668-677 (2003).
[Kha02] S. U. M. Khan, M. Al-Shahry, W. B. Ingler, Science, **297**, 2243 (2002).

[Kit08] C. Kittel, *Introduzione alla Fisica dello Stato solido*, , Casa Editrice Ambrosiana, Italy, 8th Edition (2008).
[Kok72] Th. Kokkinakis, K. Alexopoulos, Phys. Rev. Lett., **28**, 1632 (1972).
[Ing11] D. B. Ingram, S. Linic, J. Am. Chem. Soc., **133**, 5202–5205 (2011).
[ISO10] ISO 10678:2010, "*Fine ceramics, advanced technical ceramics – determination of photocatalytic activity of surfaces in an aqueous medium by degradation of methylene blue*", ISO, Geneva, 2010.
[ISO15] http://www.iso.org/iso/home.html (accessed November 2015).
[Lin95] A. L. Linsebigler, G. Lu, J. T. Yates Jr., Chem. Rev., **95**, 735-758 (1995).
[Lin11] S. Linic, P. Christopher, D. B. Ingram, Nature Materials, **10**, 911–921 (2011).
[Lit99] M. I. Litter, Appl. Catal. B, **23**, 89-114 (1999).
[Liu11] Z. Liu, W. Hou, P. Pavaskar, M. Aykol, S. B. Cronin, Nano Letters **11**, 1111-1116 (2011).
[Liu12] B. Liu, L. Wen, K. Nakata, X. Zhao, S. Liu, T. Ochiai, T. Murakami, A. Fujishima, Chem. Eur. J., **18**, 12705 – 12711 (2012).
[Liu14] E. Liu, L. Kang, Y. Yang, T. Sun, X. Hu, C. Zhu, H. Liu, Q. Wang, X. Li, J. Fan, Nanotechnology, **25**, 165401 (2014).
[Lut14] T. Luttrell, S. Halpegamage, J. Tao, A. Kramer, E. Sutter, M. Batzill, Scientific Reports 4, Article number: 4043 (2014) doi:10.1038/srep04043.
[Mai07] S. A. Maier, *Plasmonics: Fundamentals and applications*, Springer, New York, (2007).
[Mal09] S. Malato, P. Fernandez-Ibanez, M. I. Maldonado, J. Blanco, W. Gernjak, Catal. Today **147**, 1-59 (2009).
[Mat06] G. Mattioli, F. Filippone, A. Amore Bonapasta, J. Am. Chem. Soc., **128**, 13772−13780 (2006).
[Mei83] M. Meier, A. Wokaun, Optics Letters, **8**(11), 581-583 (1983).
[Mil07] A. Mills, M. McFarlane, Catalysis Today, **129**, 22–28 (2007).
[Mil12] A. Mills, C. Hill, P. K. J. Robertson, J. Photochem. Photobiol. A, **237**, 7-23 (2012).
[Moc02] J. J. Mock, M. Barbic, D. R. Smith, D. A. Schultz, S. Schultz, J. Chem. Phys., **116**, 6755 (2002).

[Nak03] R. Nakamura, A. Imanishi, K. Murakoshi, Y. Nakato, J. Am. Chem. Soc., **125**, 7443−7450 (2003).
[Nog07] C. Noguez, J. Phys. Chem. C, 111, 3806-3819 (2007).
[Nov06] L. Novotny, B. Hecht, *Principles of Nano-Optics*, Cambridge Univ. Press, Cambridge, UK, (2006).
[Noz96] A. J. Nozik, R. Memming, J. Phys. Chem., **100**, 13061-13078 (1996).
[Ohn01] T. Ohno, K. Sarukawa, K. Tokieda, M. Matsumura, J. Catal., **203**, 82–86 (2001).
[Pav13] P. Pavaskar, I.-K. Hsu, J. Theiss, W. H. Hung, S. B. Cronin, J. Appl. Phys., **113**, 034302 (2013).
[Ram94] M. Ramamoorthy, D. Vanderbilt, R.D. King-Smith, Phys. Rev. B, **49**, 16721 (1994).
[Rob06] I. Robel, V. Subramanian, M. Kuno, P. V. Kamat, J. Am. Chem. Soc., **128**(7), 2385-2393 (2006).
[Ryu08] J. Ryu, W. Choi, Environ. Sci. Technol., **42**, 294–300 (2008).
[Sca13] D. O. Scanlon, C. W. Dunnill, J. Buckeridge, S. A. Shevlin, A. J. Logsdail, S. M. Woodley, C. R. A. Catlow, M. J. Powell, R. G. Palgrave, I. P. Parkin, G. W. Watson, T. W. Keal, P. Sherwood, A. Walsh, A. A. Sokol, Nature Materials, **12**, 798–801 (2013).
[Sha08] M. A. Shannon, P. W. Bohn, M. Elimelech, J. G. Georgiadis, B. J. Marinas, A. M. Mayes, Nature, **452**, 301-310 (2008).
[Sta09] S. D. Standridge, G. C. Schatz, J. T. Hupp, J. Am. Chem. Soc., **131**, 8407–8409 (2009).
[Suà08] S. Suàrez, M. Carballa, F. Omil, J. M. Lema, Rev. Environ. Sci. Biotechnol. **7**, 125-138 (2008).
[Sze07] S. M. Sze, K. Ng Kwok, *Physics of semiconductor devices*, Third edition, John Wiley & Sons, NY, (2007).
[Teo12] W. Y. Teoh, J. A. Scott, R. Amal, J. Phys. Chem. Lett., **3**(5), 629–639 (2012).
[Win08] T. Wintgens, F. Salehi, R. Hochstrat, T. Melin, Water Sci. Technol. **57**, 99-107 (2008).
[Zha13] X. Zhang, Y. L. Chen, R. S. Liu, D. P. Tsai, Rep. Prog. Phys., **76**, 046401 (2013).

[Zim15] M. Zimbone, E. Messina, G. Compagnini, M. E. Fragalà, L. Calcagno, J. Nanopart. Res., **17**, 402 (2015).

Chapter 2: TiO_2 nanoparticles obtained by laser ablation in water

In this section we report about TiO_2 nanoparticles (NPs) obtained by a novel, industrially scalable and eco-friendly technique such as laser ablation in liquid. In particular, we observed that the photocatalytic performance of the synthetized nanomaterials is close to that of the commercial TiO_2 powder (P25). Remarkably, the antibacterial performance of the nanomaterial resulted higher than that of the commercial standard. The latter is in the crystalline state, while nanoparticles obtained via laser ablation are in amorphous phase. In order to describe the unexpected high photocatalytic activity, we suggest an explanation based on the high hydrogen content, as showed by FT-IR measurements. In addition, we studied the influence of metal nanoparticles by mixing TiO_2 NPs with Ag NPs.

2.1 Pulsed laser ablation in liquid

In the past two decades, with the rise of nanoscience, laser ablation has been broadly applied and developed for the synthesis of nanostructures [Zen12]. Nanoparticles are of great interest for a variety of application, including photocatalysis, due to the extremely high surface to volume ratio [Bey99][Lan13]. Pulsed Laser Ablation in Liquids (PLAL) has been proposed as a green, alternative nanoparticles synthesis method, addressing some of the drawbacks of the common chemical processes [Bar13]. By this method, laser radiation is used to ablate a solid target in a liquid environment, resulting in the formation of a nanoparticle colloid. A huge advantage of this synthesis route is its independence from chemical precursors (such as metal-organic substances), avoiding the use of toxic substances or by-products that possibly adsorb onto the nanoparticle surface. At the same

time, the post laser irradiation of suspended nanomaterials can be applied to further modify their size, shape, and composition [Zen12].

Laser ablation is a physical process that is fundamentally different from chemical nanoparticle synthesis routes. In the past, this process has been widely performed in a vacuum chamber (UHV or moderate gas pressure) and only recently systematic studies of laser ablation in liquids have been conducted [Yan12]. Such laser-generated colloidal nanoparticles are characterized by several potential advantages:

- *versatility*: compared to common chemical reduction or precipitation routes which rely on the availability of the respective precursors, this physico-chemical laser ablation method allows for the production of nanoparticles from any base material (metal, alloy, semiconductor, ceramic) and in numerous liquids, including polymer dissolving organic liquids or even ionic liquids.
- *availability of precursors*: the solid raw material for laser-based nanoparticle production is easily available and often 5 to 10 times cheaper than commonly used metal-organic precursor compounds.
- *purity*: the synthesis method gives access to highly pure colloids, without residual chemical precursors and without necessity of expensive cleaning treatments; this may also result in a high nanoparticle surface activity because the particle surface is not blocked by the chemical ligands or residues of the reducing agents.
- *defects*: under controlled conditions, defect-rich materials and suboxides can be synthesized [Gol06][Zen05][Sem10], potentially broadening the range of optical, semiconducting, or catalytic properties.

The main disadvantage of this technique relies on the size polydispersity (20-40%).

2.1.1 Laser ablation mechanism

The laser-target interaction can be designed in different environments (vacuum, gas, or liquid) in order to fabricate various materials. The ablation of the target material upon laser irradiation is a very complex process. The incident laser pulse penetrates into the surface of the material within a certain penetration depth. This dimension is dependent on the laser wavelength and the refraction index of the target and is typically in the range of 1000 - 10 nm. At a laser fluence of some J/cm^2, the material is typically converted to a plasma, which contains various energetic species including atoms, molecules, electrons, ions, clusters, particulates, and molten globules, and therefore possesses some unique characteristics such as high temperature, high pressure, and high density [Zen12]. Subsequently, the large pressure difference between the laser produced initial seed plasma and ambient conditions of the external environment causes a rapid expansion of the plasma plume that then cools down. This process is nearly adiabatic and transonic [Cha07]. Under suitable condensation conditions (temperature and pressure), the plasma species will nucleate and grow into desirable nanostructures, either on a substrate or in a cool liquid medium.

In the case of laser ablation in liquid, when the laser beam heats the metal target, plasma, vapor, and metal micro- or nanosized droplets can be generated as possible initial products, which further react with the liquid medium to form nanoparticles [Yan12]. So far, the main formation mechanisms of laser ablated nanostructures were based on: i) the thermal evaporation (and thus formation of the vapor or plasma phase) with the subsequent interactions with the liquid and ii) the explosive ejection of nanodroplets [Zen07][Liu08b][Niu10][Niu10b].

In Fig. 2.1 the laser ablation process in liquid ambient is sketched. First, a laser beam is focused onto a target substrate immersed in a liquid (Fig. 2.1(a)). As the beam energy is suddenly absorbed by the target surface, the temperature rises. The target material starts to vaporize and, as a consequence of the rise in the temperature, the liquid undergoes to phase

transition and reach the vapor phase. These phenomena induce a rapid increase in the pressure, thus a shock wave propagates, leaving behind a cavitation bubble (Fig. 2.1(b)). The cavitation bubble contains the plasma with a mixture of electrons, atoms and molecules coming from the target and the liquid. The cavitation bubble expands (Fig. 2.1(c)) till when the energy is relaxed and the material inside the bubble collapses in clusters and, subsequently, in nanoparticles (Fig. 2.1(d)).

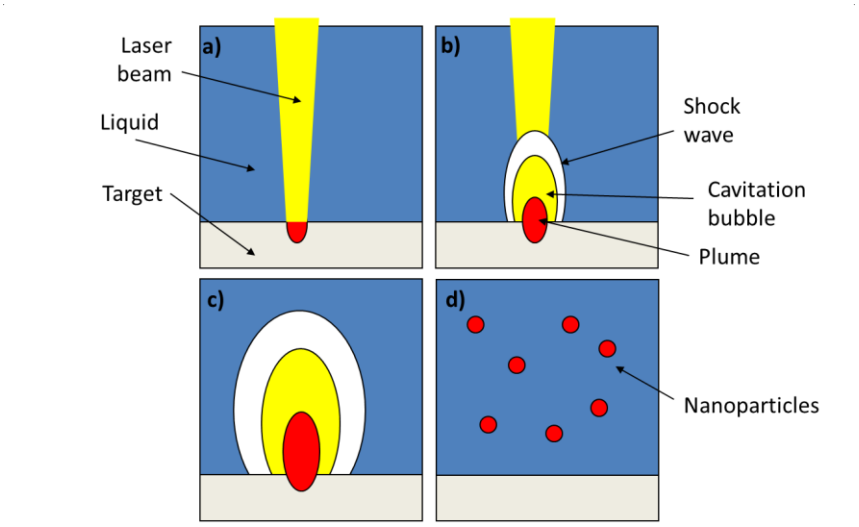

Figure 2.1: Schematic representation of the laser ablation process.(a) A laser beam is focused onto a target substrate immersed in a liquid. (b) As the beam energy is suddenly absorbed by the target surface, the sudden rise in temperature and pressure translates in a shock wave and a cavitation bubble. (c) The cavitation bubble contains a hot plasma with a mixture of electrons and atoms coming from the target and the liquid. The cavitation bubble expands and shrinks several times before (d) the formation of nanoparticles.

The ablation mechanisms is greatly determined by the laser parameters [Zen07][Niu10][Yan07]: the incident energy per unit area (fluence, F), the wavelength λ_L, the pulse duration τ_L and the optical and mechanical properties of the target and the liquid. Incoming photons are

absorbed by the electrons of the target, leading to the formation of a gas of hot carriers which eventually transfer their energy to the ions through repeated emission of phonons; the ions and electrons gas eventually reach equilibrium (the temperature of the electrons gas, T_e, equals that of the lattice, T), and this occurs on a timescale $\tau_E = 10^{-12} - 10^{-11}$ s [Sie95]. This timescale is crucially important for a proper description of the phenomenon, as it sets the boundary between strictly thermal and possible non-thermal routes to ablation, as well as between "long" and "short" pulses [vdL97]: if $\tau_L \gg \tau_E$, equilibrium between electrons and phonons prevails throughout the heating stage and phase changes can be regarded as slow thermal processes involving quasi-equilibrium thermodynamics. In contrast, for ultrashort pulses ($\tau_L \leq 10^{-12}$ s), the material is driven into a highly non-equilibrium state and $T_e \gg T$ [Yan12]: in this case, the time with which structural changes take place, τ_M, determines whether thermal mechanisms are involved ($\tau_M \gg \tau_E$) or not ($\tau_M < \tau_E$). In the case of ns pulses, the processes take place in the thermal regime. The hot electrons gas relaxes via electrons-phonons interaction and thermal effects are dominant. A portion of the target of the order of the temperature diffusion length melts and vaporizes. The fluence threshold is set by the minimum energy required the expulsion of the material:

$$F > F_{th} \approx \rho \Omega \sqrt{D \tau_L} \qquad (2.1)$$

being ρ the material density, Ω the evaporation enthalpy, D the thermal diffusion coefficient and τ_L, previously mentioned, the laser pulse. For titanium $F_{th} \sim 3\ \mathrm{J/cm^2}$.

The literature concerning Ti ablation in water is controversial since some authors claim that the ablation of a titanium target in water results in the formation of metallic titanium nanoparticles [Sem10], while others have obtained TiO_x particles [DeB13][Hua10][Nik09] or a mixture of amorphous and crystalline phases [Bou13]. Reasonably, the details of laser ablation process have a strong impact on the properties of nanoparticles.

2.2 Photocatalytic and antibacterial activity of TiO_2 NPs obtained by laser ablation in water

2.2.1 Synthesis

The synthesis of laser ablated TiO_2 nanoparticles (LA-NPs) was performed by the PLAL method. A Nd:YAG (Giant G790-30) 1064 nm laser (10 ns pulse duration, 10 Hz repetition rate) was employed to irradiate a titanium metal plate (Goodfellow, purity 99.9%, as rolled). The laser was focused using a lens (focal length of 20 cm) on the bottom of a teflon vessel filled with 5 ml of deionised Milli-Qwater (resistivity 18 MΩ·cm). The sample was irradiated at a fluence of 5 J/cm^2 and the spot size was approximately 3.5 mm in diameter. The mass of the ablated material was estimated by weighting the target before and after the ablation with a microanalytical balance (Sartorius M5) with a sensitivity of 100 μg. The titanium concentration in solution was calculated assuming that ablated material has been totally converted in nanoparticle.

Commercial standard TiO_2 nanoparticles (C-NPs) by Sigma-Aldrich were used as a reference for the discoloration experiments. Batch solution is obtained by dissolving 8 mg of powder in 8 ml of Milli-Q water (final concentration of 1 mg/ml) and stirring for 30 min.

2.2.2 Materials and methods

The UV–Vis spectra were collected using a Perkin-Elmer Lambda40 spectrometer in the wavelength range 350-900 nm with an integrating sphere (Labsphere 20). DLS measurements were performed by a homemade apparatus [Zim12]: briefly, the illumination source was a 660 nm diode laser whose power ranged between 15 and 150 mW, and the light scattered at 90° with respect the forward direction was recorded. The

intensity auto-correlation function is obtained by a BI-9100 (Brookhaven Instruments Corporation) correlator working in photon counting regime. The field autocorrelation function, g_1, is computed from the intensity autocorrelation function, g_2, using the Segret relation ($g_2 = |g_1|^2$) [Ber76] and is analyzed with second cumulant analysis method.

Infrared spectra were measured by a Fourier transform infrared Perkin-Elmer Spectrum 1000 spectrophotometer operating in the range 400-4000 cm^{-1} with a resolution of 4 cm^{-1}. To determine the absorbance, a reference spectrum of a uncoated silicon wafer was subtracted.

SEM images were acquired by using a Field Emission SEM (Gemini Zeiss SUPRATM25) at working distance of 5-6 mm, using an electron beam of 5 keV and an in-lens detector. ImageJ software was used to estimate the nanoparticles size.

High resolution TEM (HR-TEM) images were acquired using a JEOL 2010F microscope operating at an acceleration voltage of 200 kV.

Crystal structure of the reference and synthesized nanoparticles was determined by X-ray diffraction (XRD, Bruker D-9000, Cu Kα, 40 kV, 40 mA, at 0.01°s^{-1}) and Bruker diffraction suite software for the diffraction analysis. The Scherrer equation was applied to estimate the crystallite size.

The samples for SEM, TEM and XRD measurements were prepared drying a solution drop on copper foil substrates, on copper grid (covered with a holey carbon film) and glass respectively. Although some spurious effects can arise during and after drying (aggregation), the phase, shape, dimension and structure of the nanoparticles are expected to be not influenced by these effects.

The nanoparticles stoichiometry was checked by RBS using a 2 MeV He^+ beam with a scattering angle of 165° in normal incidence. Solid samples for this measurement were produced drying off a 100 µl drop of the LA-NPs solution on a suitable substrate resulting in a film of several hundreds of nm; deposited amount was estimated to be 42 µg of TiO_2.

For comparison purposes, commercial polycrystalline TiO_2 powder was amorphized by ion implantation. Gold ions (Au^+) at 250 keV at fluence

up to $4.7 \cdot 10^{15}$ at/cm^2 were used to induce a controlled damage and to obtain amorphous layers on a crystalline substrate.

Raman spectroscopy has been used to analyse and compare the quantitative crystalline composition of the samples i.e. amount of crystalline phases versus amorphous. We collected Raman spectra using a HR800 integrated system (Horiba Jobin Yvon) in a back-scattering configuration. The excitation wavelength is supplied by a He-Cd laser at 325 nm and the penetration depth for UV laser is about 16 nm so only part of the nanoparticles is probed.

In order to evaluate the photocatalytic activity of nanoparticles dispersed in water, UV-photo-degradation test with methylene blue (MB) dye was carried out [Mil12]. For these tests 20 µl of MB solutions (0.05 wt %) was added to the titanium oxide dispersion. Appropriate volumes of water were added up to 2 ml. The MB concentrations were measured applying the Lambert-bear law at 664 nm (extinction coefficient 7.4 $\cdot 10^4 M^{-1}cm^{-1}$) after subtraction of background due to the scattering of the nanoparticles. Moreover, the scattering intensity resulted in an indirect indicator of nanoparticles concentration. The solutions were left for one hour in dark in order to allow the absorption of MB onto nanoparticles and vessels surfaces and then were irradiated with UV light. During the UV light illumination the solutions were placed in a circular vessel of 2 cm^2 and covered with a quartz slide in order to prevent evaporation during irradiation. The wavelength of the UV light source was centred at 368 nm (FWHM lower than 10 nm) and UV irradiance was 1.1 mW/cm^2.

Raman and FTIR has been performed on samples deposited on a double-polished silicon substrate.

Escherichia coli is a well-known Gram-negative bacteria; it is a representative of coliforms and it is considered to be an indicator of faecal contamination. International regulations on wastewater treatment fix an upper limit of E. coli concentration in drinkable water. Hence, E. coli has been chosen as a model organism. Antibacterial activity of both C-NPs and LA-NPs was tested on Escherichia coli ATCC25922. A single colony was inoculated in 50 ml of Luria-Bertani (LB) broth and grown overnight at 37°C

by constant agitation at 180 rpm under aerobic conditions. The following day, the bacterial growth was measured by optical density at 600 nm.

CFU count. Bacteria were diluted up to 10^8 CFU/ml and exposed either to C-NPs or LA-NPs at different concentrations in a volume of 2 ml. In order to test antibacterial activity, photocatalysis was induced by exposition to the same UV light as for the MB photodegradation. Untreated and exposed to UV only bacteria were treated in parallel as controls. Experiments were made in triplicates. Different final concentrations of C-NPs and LA-NPs were tested, ranging from 25 to 100 μg/ml. Aliquots were collected at 15, 30 and 60 min respectively, conveniently diluted by serial dilutions 1:10 and plated in LB Agar Petri dishes. Plates were incubated overnight at 37°C. CFU were counted the following day.

MTT assay. Bacteria were diluted up to 10^8 CFU/ml and exposed either to C-NPs or LA-NPs at different concentrations in a volume of 200 μl. Different final concentrations of C-NPs and LA-NPs were tested, ranging from 25 to 100 μg/ml. Untreated and exposed to UV only samples were run in parallel as controls. After 60 min exposition under the UV light, 100 μl was collected from each sample. MTT (10 μl) was added to each collected sample. Samples were incubated at 37°C for 2 h in a thermostatic bath. After incubation, they were centrifuged at 8000 rpm for 3 min and the supernatant discarded. Precipitated formazan crystals were resuspended in 200 μl SDS 10%, HCl 0.01 N. After addition of 800 μl of NaCl 0.9%, samples absorbance was measured at 575 nm.

2.2.3 Structural and morphological characterization

We performed SEM and HR-TEM analysis on solid samples obtained by drying the NPs solution onto a proper substrate. As already mentioned in the previous section, despite the aggregation of nanoparticles has occurred, the phase, shape, dimensions and structure of the nanoparticles are expected to be not influenced. In Fig. 2.1 are shown the NPs diameters

distribution and a high magnification SEM (inset). The distribution has been fitted with a log-normal distribution [Gra76]:

$$f(d) = \frac{1}{\sqrt{2\pi}\sigma d} e^{-\frac{(\ln d - \ln\langle d\rangle)^2}{2\sigma^2}} \qquad (2.1)$$

with a mean diameter $\langle d\rangle = 34 \pm 1\ \mathrm{nm}$ and $\sigma = 0.5$. As previously mentioned, PLAL typically is characterized by a high polydispersity.

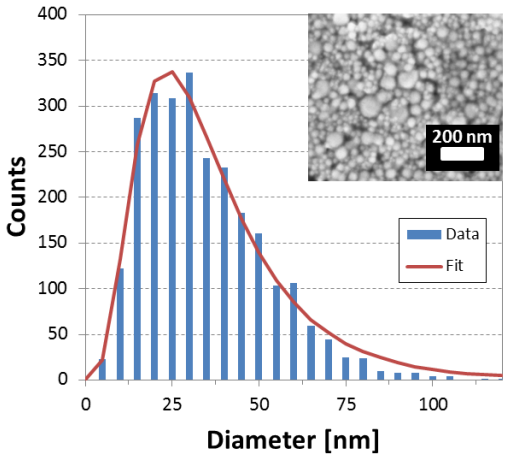

Figure 2.1: Size distribution of LA-NPs together with a log-normal distribution fit. In the inset, a typical SEM image of the laser ablated nanoparticles.

Fig. 2.2(a) reports a HR-TEM image of laser ablated nanoparticles (LA-NPs). The nanoparticles appear amorphous and spherical with well-defined contour. In the case of commercial nanoparticles (C-NPs) compact aggregates of some microns in diameter are observed (Fig. 2.2 (b)). These aggregates are constituted by smaller nanoparticles with mean size of 50 nm.

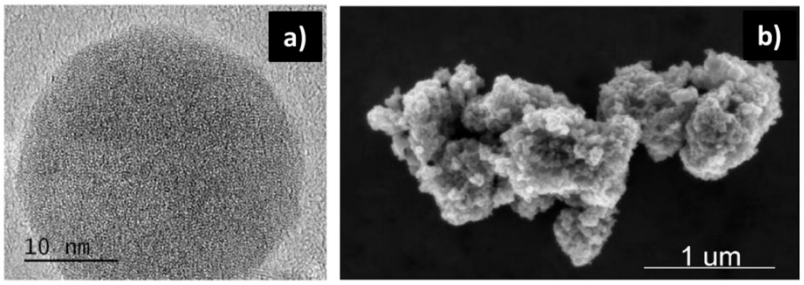

Figure 2.2: (a) High resolution TEM image of a LA-NP and (b) SEM image of aggregate commercial nanoparticles (C-NPs). From ref. [Zim15].

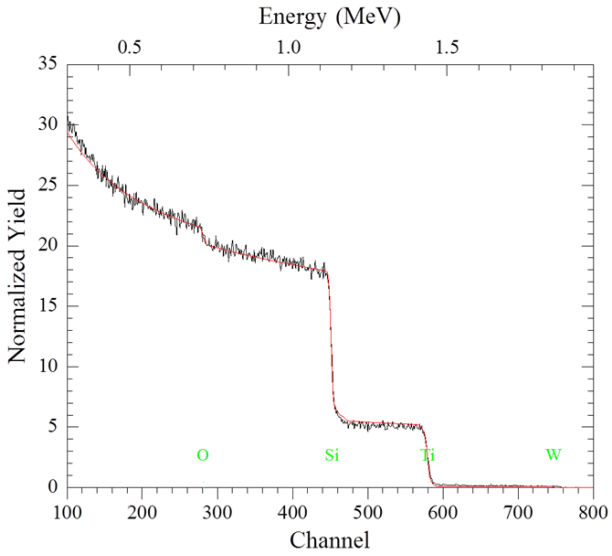

Figure 2.3: RBS spectrum of LA-NPs. The position of the signal of W, Ti, Si and O are marked.

The stoichiometry of the laser ablated nanoparticles was checked via RBS. The measurement was performed on a solid sample obtained drying several drops on nanoparticles solution onto a Si substrate. The RBS spectrum, reported in Fig. 2.3, shows signals from Ti, O, and Si. Actually, a small contamination of tungsten is observable. A similar contamination was found on the Ti target, and is probably due to the process (rolling) for the

production of the foil. From the ratio of the Ti peak area to that of O, the ratio [O]/[Ti] = 2.0 ± 0.1 has been evaluated. This stoichiometry is an averaged value since the film is composed by a random distribution of aggregated nanoparticles and it is not possible to evaluate the eventual oxidation profile over the particle structure.

XRD patterns obtained from LA-NPs and C-NPs are presented in Fig. 2.4. The diffraction pattern of the LA-NPs presents a very low intensity and broad peak (in the range 20°–30°) indicating the existence of a weak crystalline (highly disordered) structure. However, the position of the peak close to the anatase phase signal, though the presence of small amount of rutile cannot be excluded.

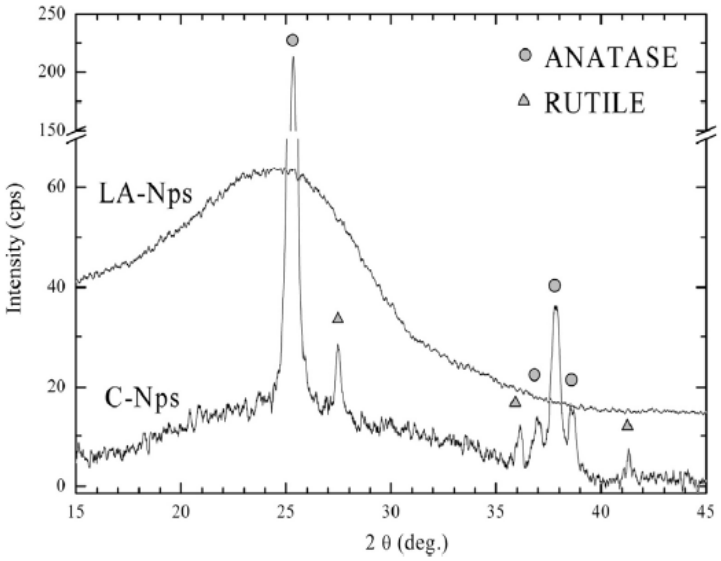

Figure 2.4: XRD pattern of LA-NPs and C-NPs. The anatase and rutile peaks are represent by circles and triangles, respectively. From ref. [Zim15].

Not taking into account lattice imperfections, possible inhomogeneous strains of the crystalline lattice, and assuming a unique anatase phase crystal, the average grain size of 2 nm can be estimated from the spectra by using the Debye-Scherrer approximation [Cul78]. This value is not contrast

with SEM and TEM observation because the used approximation refers to the crystal grain size and not to the particle dimension. C-NPs have well defined crystal structure composed by anatase and rutile, with a mixture of about 86% of anatase and 14% of rutile. We extracted the relative amounts of the crystalline structure from XRD according to [Spu57]:

$$w_{Ru} = \frac{1}{1 + 0.8\frac{I^{An}_{(101)}}{I^{Ru}_{(110)}}} \tag{2.2}$$

where w_{Ru} is the weight fraction of rutile in the powders, $I^{An}_{(101)}$ is the X-ray intensity of the anatase peak for the orientation (101) ($2\vartheta = 25.5°$), and $I^{Ru}_{(110)}$ is the X-ray intensity of the rutile peak for the orientation (110) ($2\vartheta = 27.5°$).

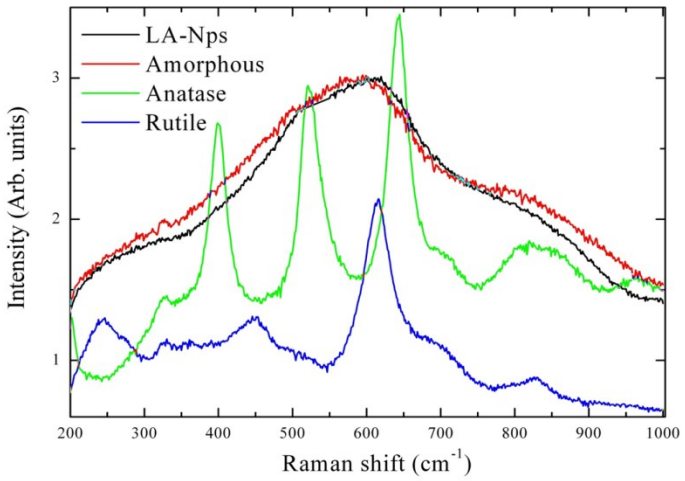

Figure 2.5: Raman response of LA-NPs compared with that of amorphous, rutile and anatase TiO_2 samples. From [Zim15].

The presence of amorphous phase cannot be excluded on the basis of the XRD results. Indeed, a broad peak compatible with an amorphous

phase has been observed by Raman spectroscopy measurements (Fig. 2.5). For comparison purposes, commercial polycrystalline TiO_2 powder was amorphized by ion implantation. Gold ions (Au^+) at 250 keV at fluence up to $4.7 \cdot 10^{15}$ at/cm^2 were used to induce a controlled damage and to obtain amorphous layers on a crystalline substrate. According to Raman analysis, LA-NPs show a response composed by broad peaks, similar to amorphous TiO_2 sample. The typical response of crystalline (rutile or anatase) TiO_2 is also reported.

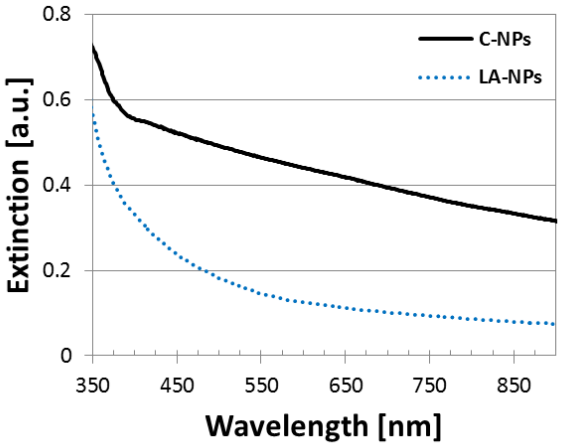

Figure 2.6: UV–Vis spectra of laser abated titanium oxide nanoparticles and commercial TiO_2 nanoparticles in water.

In general, the crystalline phases of TiO_2 are the most stable. In particular, anatase is preferred in crystallites smaller than about 14 nm [Zha98]. The formation of the amorphous phase in LA-NPs could be ascribed to the fast, non-equilibrium quenching process and to the high temperature and pressure that are peculiar of the laser ablation process. During the laser ablation in liquid, high temperature and high pressure are exercised on the target surface, thus leading to the formation of a hot plasma plume over the laser spot [DeG13]. High pressure (similar to those obtained during confinement of the plume inside the cavitation bubble) has

been reported to cause the anatase-amorphous transition [Swa05][Yan07]. Moreover, since the process take place in water, the mixing with hydrogen, oxygen and water molecules can likely occur, enhancing the temperature quenching and realizing the Ti-O alloy [Iti11][Sem10].

Fig. 2.6 shows the UV-Vis spectra of laser ablated and commercial TiO_2 nanoparticles in distilled water. A strong absorption occurs below 400 nm in both samples; at longer wavelength the extinction of LA-NPs is definitely lower than that of C-NPs because of the scattering contribution. In order to extract the absorption coefficient α from the extinction spectra, the contributions of the scattered light, fitted with an exponential law, has been subtracted.

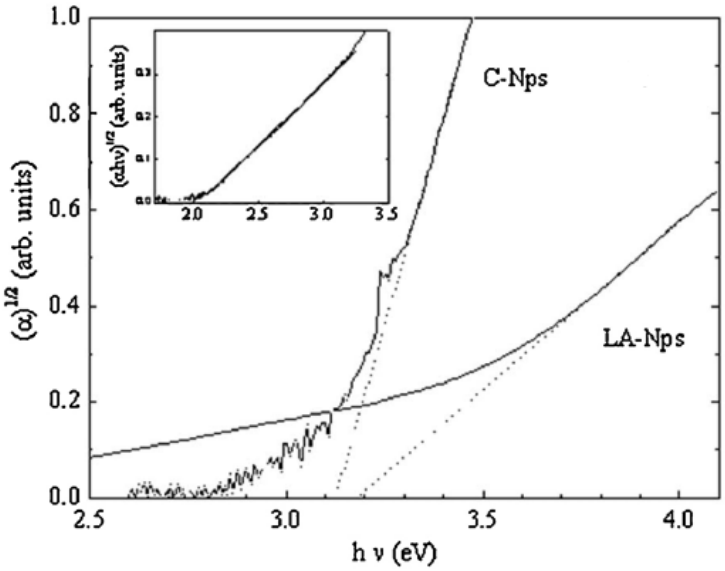

Figure 2.7: Tauc plot of laser ablated (LA-NPs) and commercial (C-NPs) nanoparticles. In the inset, a detail of LA-NPs spectra in low photon energy range, evidencing the presence of intragap states. Taken from [Zim15].

It is well known that in direct bandgap or amorphous semiconductors the quantity $(\alpha h\upsilon)^r$ depends linearly on $h\upsilon$ being $r = 2$ or

$r = 1/2$ respectively [Sch06]. In indirect bandgap semiconductors $\alpha^{1/2}$ is linear with $h\upsilon$ and the band gap value is the intercept of the fit of the experimental curve with $h\upsilon$ axis. In Fig. 2.7 $\alpha^{1/2}$ versus $h\upsilon$ is reported for both LA-NPs and C-NPs. From the linear fit of the two curves we extracted a bandgap value of 3.13 eV and 3.18 eV for laser ablated and commercial nanoparticles, respectively. This result is in agreement with generally accepted values [Bar10]. Moreover, in the inset of Fig. 2.7 LA-NPs spectra evidences a linear behavior at photons energy lower than 3 eV, thereby suggesting either the presence of a large amount of states inside the band-gap or a fraction of amorphous phase.

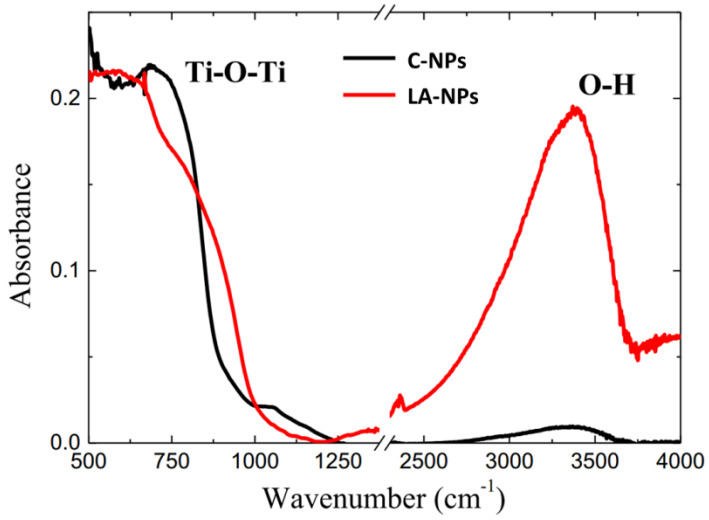

Figure 2.8: FTIR spectra of crystalline TiO_2 (C-NPs), and laser ablated nanoparticles (LA-NPs). Ti-O-Ti vibration and O-H stretching bands are referred in the figure. Adapted from [Zim15b].

It is worth noting that the presence of hydroxyl groups, in dried LA-NPs, has been evidenced by FTIR spectroscopy measurements, reported in Fig. 2.8. Hydrogen is identified by OH stretching at about 3400 cm^{-1} in FTIR spectra, as previously reported by Johnson *et al.* [Joh73]. In the spectral range sampled in Fig. 2.8, we clearly observe the typical absorption of TiO_2

in the 500-1000 cm^{-1} range and a strong absorption at 3000-3500 cm^{-1} due to the hydroxyl vibration. The amount of hydroxyl groups is directly related to the amount of hydrogen in or on the nanoparticles surface [Joh73]. In order to compare the amount of OH in LA-NPs and C-NPs, we can normalize the spectra to the TiO_2 signal in both samples. The number of hydroxyl groups in LA-NPs is found to be about one order of magnitude greater than the crystalline samples. We can state that pulsed laser ablation in liquid, in this particular experimental set-up, results in the formation nm-sized hydrogenated TiO_2 nanoparticles. The phase of LA-NPs can be either a highly-disordered small-sized anatase phase or a mixture of anatase and amorphous TiO_2.

The hydrodynamic diameter and the mass of LA-NPs as a function of irradiation time are shown in Fig. 2.9a and Fig. 2.9b, respectively. In the initial stage (t < 10 min), large nanoparticles are formed at a rate of 30 µg/min, while at longer times both nanoparticles diameter and the ablation rate saturate at 180 nm and 70 g/min, respectively. In the inset of Fig. 2.9a the comparison between the intensity autocorrelation function of LA-NPs and C-NPs is shown. Cumulant analysis gives a decay time of $1.4 \cdot 10^{-3}$s and $8.5 \cdot 10^{-3}$s corresponding to a hydrodynamic diameter of about 181 nm for LA-NPs and 1.1 µm for C-NPs. Note that, even though DLS is a fast, non-destructive technique, it overestimates the particle size in polydisperse systems since the scattered light depends on the sixth power of the diameter. As a consequence, the hydrodynamic diameter does not correspond to the diameter of the nanoparticles as obtained via SEM and TEM analysis. The hydrodynamic diameter reduces abruptly during the first ten minutes of irradiation ($6 \cdot 10^3$ pulses) from 250 nm to the final steady state value of 180 nm. This can be caused by a variation of the nanoparticles morphology because of the re-irradiation of the nanoparticles dispersed in water. It has been shown that the absorption of the laser energy and the consequent melting or vaporization of the nanoparticles induce the reshaping or resizing, respectively [Eva12].

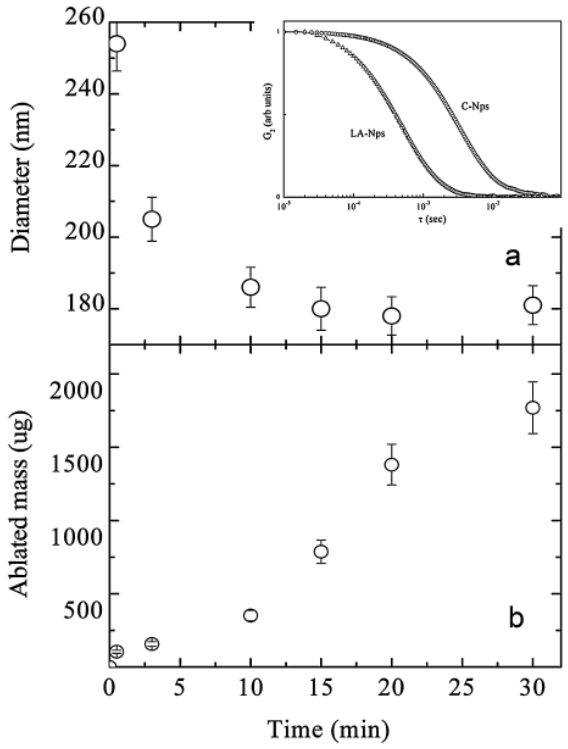

Figure 2.9: (a) Hydrodynamic diameter and (b) ablated mass as a function of ablation time. In the inset, DLS autocorrelation functions for LA-NPs and C-NPs in semi-log scale. From ref. [Zim15].

2.2.3 Photocatalytic and antibacterial tests

The photocatalytic activity of LA-NPs was measured by means of the discoloration of methylene blue dye. We performed test using colloidal solution of LA-NPs and C-NPs.

In Fig. 2.10 we report the relative MB absorption at 664 nm as a function of UV irradiation time, for concentration of LA-NPs ranging from 5 µg/ml to 100 µg/ml. The small decrease of pure MB-water solution under illumination is also shown for comparison. The MB-NPs solutions were left in dark prior to the UV irradiation in order to allow the adsorption of the

MB onto the surface of the NPs and also of the vessel containing the solution. Thus the reduction of MB concentration under UV exposure can be ascribed solely to the photocatalytic activity of TiO_2. The decrease of MB concentration under UV exposition follows a first-order kinetic law: $\ln\frac{C}{C_0} = -kt$, where *k* is the discoloration rate constant.

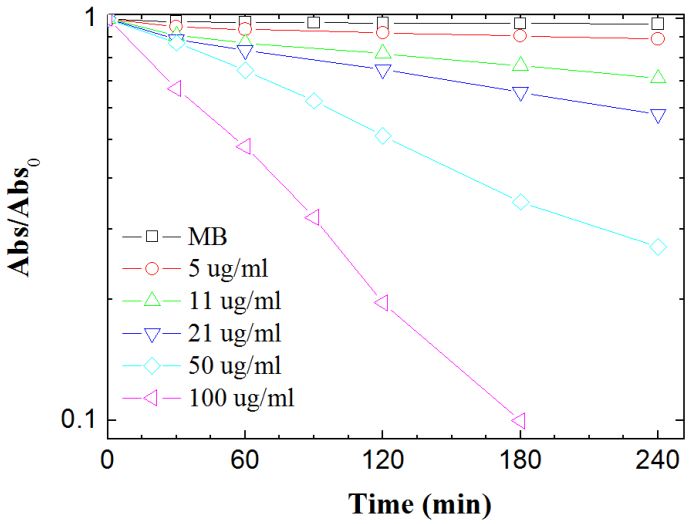

Figure 2.10: Relative MB absorption at 664 nm as a function of UV irradiation time, for concentration of LA-NPs ranging from 5 µg/ml to 100 µg/ml.

The results for several TiO_2 concentrations are summarized in Fig. 2.11, where the *k* values for both LA-NPs and C-NPs are reported as full dots and open circles, respectively. Interestingly, the data points from LA-NPs and C-NPs lie on the same curve. The observed discoloration rate presents a linear trend with the concentration of LA-NPs in solution. LA-NPs show a steady state photoactivity similar to that of C-NPs, demonstrating a high catalytic efficiency, despite the low degree of crystallinity and the presence of a highly disorder or amorphous phase.

Different concentrations of C-NPs and LA-NPs were tested for CFU counts and MTT assay, ranging from 25 μg/ml to 100 μg/ml. The best activity was obtained at the highest TiO_2 concentration (100 μg/ml). In Fig. 2.12a untreated and exposed to UV only bacteria, run as controls, are shown in the same figure. The reduction induced by the UV irradiation after 60 min is about 20%. After 60 min exposure to C-NPs, E. coli survival rate is around 25%. However, after 60 min exposure to LA-NPs, bacterial survival rate was around 15%. Thus, LA-NPs display a slightly enhanced antibacterial activity if compared to that showed by C-NPs.

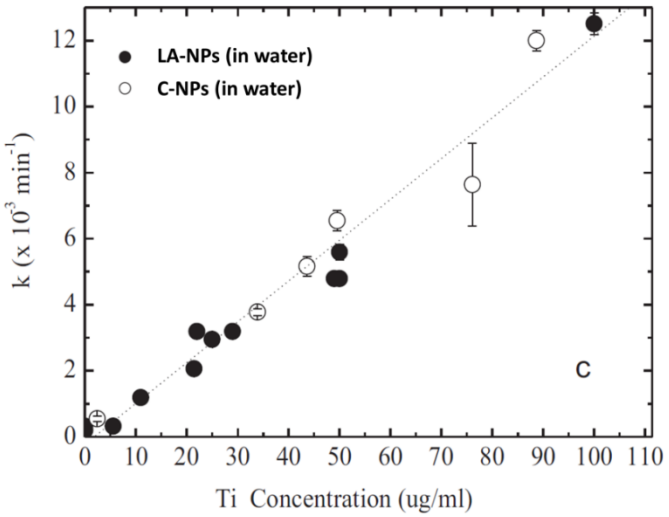

Figure 2.11: Discoloration rate constant of LA-NPs and C-NPs as a function of the amount of titanium. From ref. [Zim15].

In order to evaluate the effect on the vitality of the survived bacteria colonies, we used MTT assay test. MTT assay is based on the conversion of tetrazolium dye 3-(4,5-dimethylthiazol-2-yl)-2,5-diphenyltetrazolium bromide (MTT) into purple formazan crystals, by succinate dehydrogenase, a Krebs cycle's enzyme. Most respiring microorganisms are able to reduce tetrazolium dyes in their electron

transport chain, generating results within hours [Ber05]. Since in aerobic conditions, the respiratory activity is proportional to the number of viable cells, this assay is broadly used to measure in vitro cytotoxic effects. MTT assay confirms the results obtained by CFU count. After 60 min exposure to C-NPs at the final concentration of 100 μg/ml, metabolism rate is reduced up to 22% whereas after 60 min exposure to LA-NPs, metabolism rate is reduced up to 14%. This result is shown in Fig. 2.12b. Again, LA-NPs show a higher activity with respect to C-NPs. In both assays, the experimental error is 5%. Therefore, differences in the antibacterial activity of LA-NPs and C-NPs, albeit small, are statistically significant.

The high photocatalytic and antibacterial activity of LA-NPs maybe ascribed to the presence of a disordered phase, to the high concentration of defects and to the high content of hydrogen. In fact, the presence of defects such as Ti interstitials, O vacancies, H inclusions can enhance the photoactivity of titanium dioxide [Fuj08]. While the first introduce intragap trap states for photogenerated holes, the last two trap electrons and mediate the scavenging mediated by O_2. According to the most accepted mechanism of photocatalysis [Fuj08], holes are trapped at surface defects and electrons localize into small hydrogen-rich surface regions. This charge separation reduces the recombination probability and increases the photocatalytic effect. A highly disorder TiO_2 with a large amount of hydrogen inclusion (the so-called “black hydrogenated TiO_2”) has been recently synthesized [Che15]. The enhancement of the photocatalytic activity is ascribed to a superficial disordered layer induced by the incorporation of H onto the surface of the nanoparticles [Che11]. In our case, nanoparticles have both a relatively high amount of defects or disordered layer, and hydrogen content, as detected by FTIR. These characteristic are probably due to the synthesis mechanism. These features could make LA-NPs similar to black hydrogenated TiO_2 and this could be the reason of the high photocatalytic and antibacterial activity. Moreover, although the presence of mixed phase anatase-rutile has been ascribed responsible of an enhanced photoactivity due to charge separation [Sca13], also an amorphous component appears to be relevant.

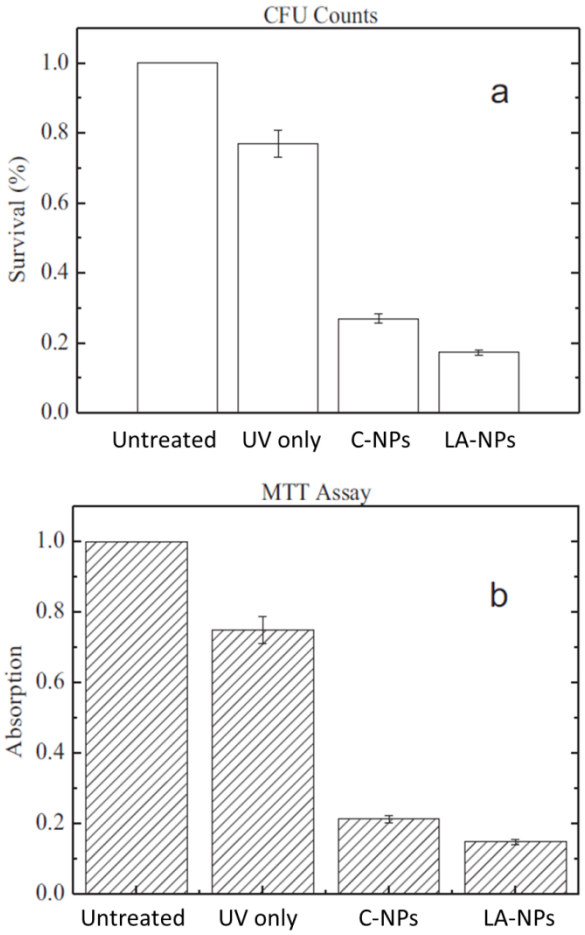

Figure 2.12: Antibacterial activity test. Relative E. coli survival rate for CFU count (a) and relative values of absorbance measured at 575 nm for MTT assay (b) after 60 min exposure to LA-NPs and C-NPs. Untreated control and UV control were run in parallel. From ref. [Zim15].

2.3 Ag-TiO_2 mixture

2.3.1 Ag nanoparticles obtained via pulsed laser ablation in liquid

The synthesis of laser ablated silver nanoparticles (Ag-NPs) was performed by the PLAL method. A Nd:YAG (Giant G790-30) 1064 nm laser (10 ns pulse duration, 10 Hz repetition rate) was employed to irradiate a silver metal target (purity 99.9%). The laser was focused using a lens (focal length of 20 cm) on the bottom of a teflon vessel filled with 5 ml of deionised Milli-Qwater (resistivity 18 MΩ·cm). The sample was irradiated at a fluence of 5 J/cm^2 and the spot size was approximately 3.5 mm in diameter.

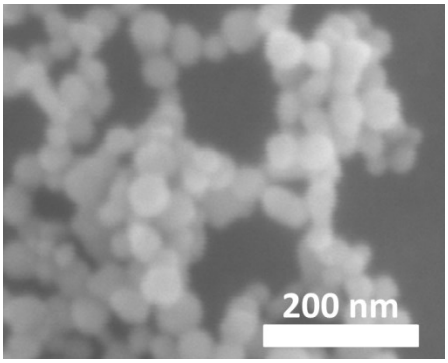

Figure 2.13: High magnification SEM image of laser ablated Ag nanoparticles.

In Fig. 2.13 is shown an SEM image of the Ag-NPs. In order to perform the measurement, a drop of nanoparticles solution was dried onto silicon substrate. The particles appear spherical and have an average diameter of 25 ± 1 nm nm.

From XRD the presence of metallic Ag is confirmed, as enlightened by the detail in Fig. 2.14. Once again the measurement has been performed drying a drop of Ag-NPs solution onto a solid substrate (quartz).The Debye-

Scherrer approximation [Cul78] provides a crystal size of about 29 ± 3 nm, in accordance with SEM observation.

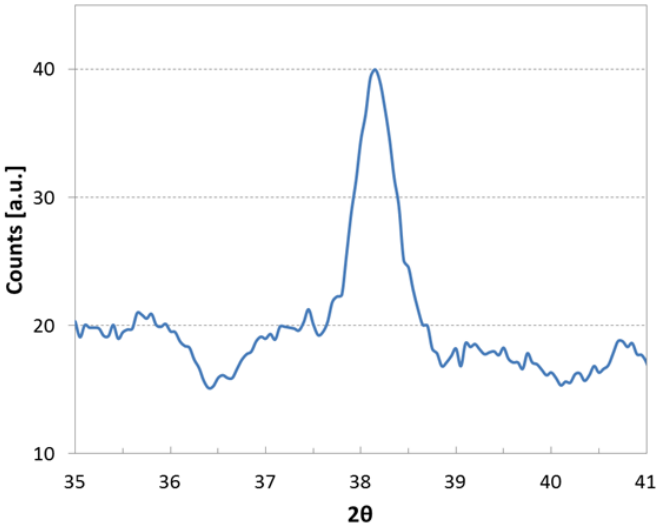

Figure 2.14: XRD spectra of the laser ablated Ag nanoparticles showing a detail of the Ag peak.

2.3.2 Effect of the Ag on the photocatalytic performance of the laser ablated TiO_2 NPs

In order to evaluate the effect of the Ag nanoparticles on the photoactivity of LA-NPs, we performed MB test with a mixture of Ag-NPs and TiO_2 nanoparticles obtained via laser ablation. We compared the resulting photocatalytic behavior with LA-NPs without silver. In Fig. 2.15 are shown the absorbance spectra of MB solution in contact with LA-NPs (Fig. 2.15 left) and Ag-TiO_2 mixture (Fig. 2.15 right) versus time of irradiation. Note that in presence of the Ag-NPs the concentration of MB has decreased more than in the case of bare TiO_2.

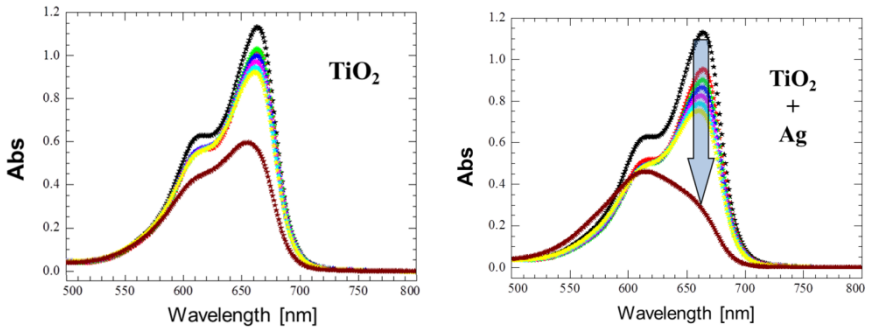

Figure 2.15: Absorbance of the MB solution in contact with LA-NPs (left) or a mixture of Ag and TiO_2 nanoparticles obtained by laser ablation (right) versus time.

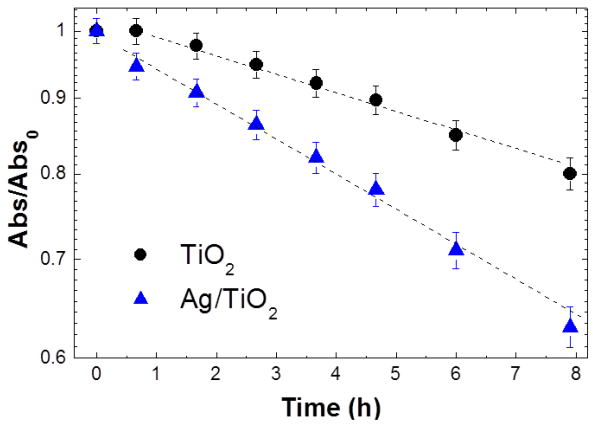

Figure 2.16: Normalized absorbance of the MB solution at the wavelength of 664nm in the case of LA-NPs (black circles) and Ag-TiO_2 mixture (blue triangles) versus time.

The difference in the efficiency results more evident from Fig. 2.16, where the normalized absorbance at 664 nm versus time for the two samples is reported. Note that this normalized value correspond to the concentration of MB in solution according to $\frac{C}{C_0} = \frac{A}{A_0}$. The Ag-$TiO_2$ mixture

shows clearly a better photocatalytic performance. Since silver itself is not a photocatalytic material, such enhancement is ascribable to the effect of the contact between Ag-NPs and TiO_2 LA-NPs. Indeed, the presence of a metal-TiO_2 contact can effectively enhance the charge separation at the surface of nanoparticles thus increasing the carrier lifetime and the photocatalytic efficiency [Lin11][Zha13].

2.4 Conclusions

TiO_2 nanoparticles have been synthetized via pulsed laser ablation in liquid. Laser ablated nanoparticles (LA-NPs) have been found in highly disordered phase and with a high hydrogen content. Despite the amorphous phase, LA-NPs showed a photocatalytic activity similar to crystalline commercial powder (P25, C-NPs) and a higher antibacterial activity. This unexpected result has been explained taking into account the effects of disorder and hydrogen inclusion in the structure of TiO_2 nanoparticles. The mixture of LA-NPs with Ag nanoparticles obtained via laser ablation has been demonstrated to further improve the photocatalytic efficiency of TiO_2, thanks to an enhanced charge separation.

2.5 References

[Bar10] F. Barreca, N. Acacia, E. Barletta, D. Spadaro, G. Currò, F. Neri, Appl. Surf. Sci., **256**, 6408–6412 (2010).
[Bar13] S. Barcikowski, G. Compagnini, Phys. Chem. Chem. Phys., **15**, 3022 (2013).
[Ber76] B. Berne, R. Pecora, *Dynamic Light Scattering*, New York, Wiley, (1976).
[Ber05] M. V. Berridge, P. M. Herst, A .S. Tan, Biotechnol. Annu. Rev., **11**, 127-152 (2005).

[Bey99] D. Beydoun, R. Amal , G. Low, S. McEvoy, J. Nanopart. Res., **1**, 439–458 (1999).
[Bou13] M. Boutinguiza, J. del Val, A. Riveiro, F. Lusquiños, F. Quintero, R. Comesaña, J. Pou, Phys. Proc., **41**, 787–793 (2013).
[Cha07] S. Chakraborty, H. Sakata, E. Yokoyama, M. Wakaki, D. Chakravorty, Appl. Surf. Sci., **254**, 638 (2007).
[Cul78] B. D. Cullity, *Elements of X-ray Diffraction*, Addison-Wesley, Reading, MA, (1978).
[Che11] X. Chen, L. Liu, P. Y. Yu, S. S. Mao, Science, **331**, 746 (2011).
[Che15] X. Chen, L. Liu, F. Huang, Chem. Soc. Rev., **44**, 1861 (2015).
[DeG13] A. De Giacomo, M. Dell'aglio, A. Santagata, C. R. Gaudiuso, O. De Pascale, P. Wagener, G. C. Messina, G. Compagnini, S. Barcikowski, Phys. Chem. Chem. Phys., **15**, 3083–3092 (2013).
[Eva12] C. C. Evans, J. D. B. Bradley, E. A. Martí-Panameno, E. Mazur, Opt. Expr., **20**(3), 3118–3128 (2012).
[Gol06] J. S. Golightly, A. W. Castleman Jr., J. Phys. Chem. B, **110**, 19979 (2006).
[Gra76] C. G. Granqvist, R. A. Buhrman, J. Appl. Phys., **47**, 2200-2219 (1976).
[Has09] M. Hashida, H. Mishima, S. Tokita, S. Sakabe, Opt. Express , **17**, 13116 (2009).
[Hua10] C. Huang, J. Bow, Y. Zheng, S.Y. Chen, N.J. Ho, P. Shen, Nanoscale Res. Lett., **5**, 972–985 (2010).
[Iti11] T.E. Itina, J. Phys. Chem. C, **115**, 5044–5048 (2011).
[Joh73] O. W. Johnson, J. DeFord, J. W. Shaner, J. Appl. Phys., **44**, 3008 (1973).
[Lan13] Y. Lan, Y. Lu, Z. Ren, Nano Energy, **2**, 1031-1045 (2013).
[Lin11] S. Linic, P. Christopher, D. B. Ingram, Nature Materials, **10**, 911–921 (2011).
[Liu08] P. Liu, C. X. Wang, X. Y. Chen, G. W. Yang, J. Phys. Chem. C, **112**, 13450 (2008).
[Liu08b] P. S. Liu, W. P. Cai, H. B. Zeng, J. Phys. Chem. C, **112**, 3261 (2008).
[Mil12] A. Mills, C. Hill, P. K. J. Robertson, J. Photochem. Photobiol. A, **237**, 7-23 (2012).

[Nik09] A. S. Nikolov, P. A. Atanasov, D. R. Milev, T. R. Stoyanchov, A. D. Deleva, Z. Y. Peshev, Appl. Surf. Sci. **255**, 5351–5354 (2009).
[Niu10] K. Y. Niu, J. Yang, S. A. Kulinich, J. Sun, H. Li, X. W. Du, J. Am. Chem. Soc., **132**, 9814 (2010).
[Niu10b] K. Y. Niu, J. Yang, J. Sun, X. W. Du, Nanotechnology, **21**, 295604 (2010).
[Sca13] D. O. Scanlon, C. W. Dunnill, J. Buckeridge, S. A. Shevlin, A. J. Logsdail, S. M. Woodley, C. R. A. Catlow, M. J. Powell, R. G. Palgrave, I. P. Parkin, G. W. Watson, T. W. Keal, P. Sherwood, A. Walsh, A. A. Sokol, Nature Materials, **12**, 798–801 (2013).
[Sch06] D. K. Schroder, *Semiconductor material and device characterization*, John Wiley & Sons, (2006.)
[Sem10] N. G. Semaltianos, S. Logothetidis, N. Frangis, I. Tsiaoussis, W. Perrie, G. Dearden, K. G. Watkins, Chem. Phys. Lett., **496**, 113–116 (2010).
[Sie95] Y. Siegal, E. N. Glezer, L. Huang, E. Mazur, Ann. Rev. Mat. Sci., **25**, 223, (1995).
[Spu57] R. A. Spurr, H. Myers, Anal. Chem., **29**, 760 (1957).
[Swa05] V. Swamy, A. Kuznetsov, L. S. Dubrovinsky, R. A. Caruso, D. G. Shchukin, B. C. Muddle, Phys. Rev. B, **71**, 184302 (2005).
[vdL97] D. von der Linde, K. Sokolowski-Tinten, J. Bialkowski, Appl. Surf. Sci., **109–110**, 1 (1997).
[Yan07] G. W. Yang, Prog. Mater. Sci., **52**, 648 (2007).
[Yan12] G. Yang (ed.), *Laser ablation in liquids: principles and applications in the preparation of nanomaterials*, CRC Press, (2012).
[Zen05] H. Zeng, W. Cai, Y. Li, P. Liu, J. Phys. Chem. B, **109**, 18260 (2005).
[Zen07] H. B. Zeng, Z. Li, W. Cai, B. Cao, P. Liu, S. Yang, J. Phys. Chem. B, **111**, 14311 (2007).
[Zen12] H. Zeng, X.-W. Du, S. C. Singh, S. A. Kulinich, S. Yang, J. He, W. Cai, Adv. Funct. Mater., **22**, 1333–1353 (2012).
[Zha98] H. Zhang, J. F. Banfield, J. Mater. Chem., **8(9)**, 2073–2076, (1998).
[Zha00] H. Zhang, J. F. Banfield, J. Phys. Chem. B, **104**, 3481–3487 (2000).
[Zha13] X. Zhang, Y. L. Chen, R. S. Liu, D. P. Tsai, Rep. Prog. Phys., **76**, 046401 (2013).

[Zim12] M. Zimbone, P. Musumeci, P. Baeri, E. Messina, S. Boninelli, G. Compagnini, L. Calcagno, J. Nanopart. Res., **14**, 1308 (2012).
[Zim15] M. Zimbone, M. A. Buccheri, G. Cacciato, R. Sanz, G. Rappazzo, S. Boninelli, R. Reitano, L. Romano, V. Privitera, M. G. Grimaldi, *Applied Catalysis B: Environmental*, **165**, 487-494, (2015).
[Zim15b] M. Zimbone, G. Cacciato, M. A. Buccheri, R. Sanz, N. Piluso, R. Reitano, F. La Via, M. G. Grimaldi, V. Privitera, Mat. Sci. Sem. Proc. (2015) http://dx.doi.org/10.1016/j.mssp.2015.09.012.

Chapter 3: Metal nanostructures on top of TiO_2 thin films

In this section we report about on the photocatalytic efficiency of both anatase and rutile thin films partially covered by Au nanoislands. The Au nanoparticles (NPs) film has been obtained by dewetting of a thin Au layer. Despite the reduction in the photocatalytic efficiency under UV illumination, ascribed to a shadowing effect, we can argue that the presence of metal nanostructures is not affecting the photocatalytic process of TiO_2 itself, i.e. the nanostructures do not seem to introduce defects and/or detrimental surface states that interfere with the process. Thus, these substrates are eligible as ideal candidate for visible-driven photocatalysis.

3.1 Thin metal film dewetting as nanostructuration strategy

Metal nanostructures have a key role in the actual nanotechnology revolution: they can be properly engineered in order to fit a specific application such as nanoelectronics, plasmonics or sensing [Joh12][Fel02] [Sau12][Lin12]. As already discussed in Chapter 1, TiO_2 titania large bang gap (3.2 eV) makes it unsuitable for efficient photocatalysis under solar illumination since only the UV component of the spectrum (~5%) activates the process. However, it has been proved that metal nanoparticles (NPs) can improve light absorption in the visible range by means of their localized surface plasmon resonances (LSRP) [Lin11][Hou13].

Several nanofabrication techniques have been developed, based on top-down as well as bottom-up approaches [Cui08]. In general top-down nanofabrication is an expensive method that allows obtaining nanostructures larger than 10 nm with a high control on spatial regularity and size. In contrast, the low-cost bottom-up approaches allow obtaining nanostructures smaller than 10 nm with poor spatial and size control. In

this sense, the controlled dewetting process of thin metal films arises as promising and powerful patterning strategy for metal nanostructures on surfaces because it can combine the strengths of both approaches [Ruf15].

The dewetting process is driven by the minimization of the total surface free energy of the system. In the case of a film, this minimum is reached when the film breaks to form droplets. The wettability of the film on the substrate is defined by the spreading coefficient S [Bon09][deG85] [Geo03][Lég92]:

$$S = \gamma_S - \gamma_F - \gamma_{S/F} \tag{3.1}$$

being γ_S the substrate surface free energy, γ_F the film surface free energy $\gamma_{S/F}$ the substrate-film interface energy. When $S > 0$ ($\gamma_F + \gamma_{S/F} < \gamma_S$), the film is thermodynamically stable on the surface and it wets the substrate. When $S < 0$ ($\gamma_F + \gamma_{S/F} > \gamma_S$), the film is thermodynamically unstable on the surface and it does not wet the substrate.

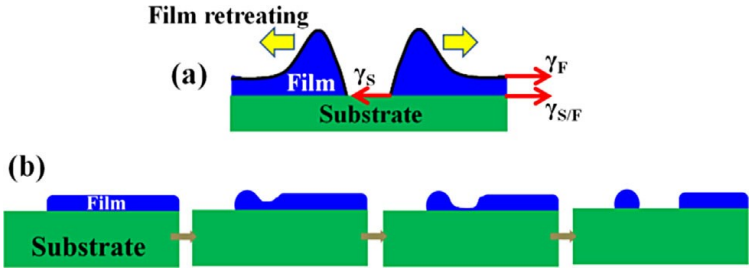

Figure 3.1: (a) Schematic representation of the thin film retreating process on a substrate as start step of the dewetting phenomenon if $S < 0$. (b) Schematic picture (cross-view) summary of a dewetting process leading to the production of droplets from a continuous film. From ref. [Ruf15].

In the latter case, the film tends to form droplets (Fig. 3.1), with a characteristic contact angle that is expressed, in first approximation, by the Young-Dupree equation [Bon09][deG85] [Geo03][Lég92]:

$$\cos\theta_c = \frac{(\gamma_S - \gamma_{S/F})}{\gamma_F} \qquad (3.2)$$

In general, the dewetting process can be summarized as follow [Mül03] [Her08][Tho12]: first the nucleation of holes occurs in the film; then, the holes reach the film surface and start to grow; as a consequence of mass conservation and also a curvature gradient at their edges, the holes develop a thickened rim (Fig 3.2(a)). At this point, the corners of the holes become unstable and, as the rims break, one observes the retraction of the film and the formation of material lines (Fig 3.2(b)) and, subsequently, the formation of droplets (Fig 3.2(c)).

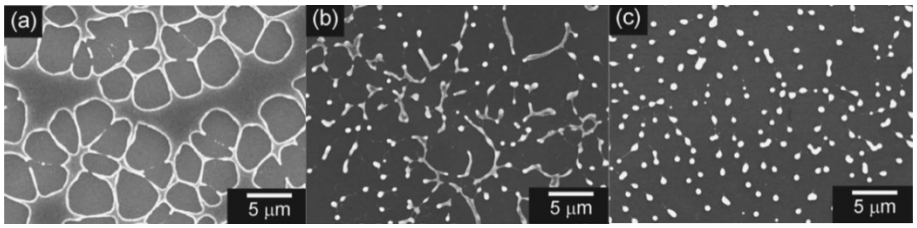

Figure 3.2: SEM images of a Mo film on SiO_2. In this case the dewetting occurs through laser annealing (a) before, (b) close and (c) above the threshold fluence for nanostructuring. From ref. [Hen05].

In the case of a metal film, *S* is commonly negative for solid non-metal substrates. In fact, the typical metal-metal interaction is much stronger than metal-non-metal one. Thus, metallic thin films deposited in non-metal substrates (e.g. oxides) are thermodynamically and dewetting could occur at temperatures well below the metal melting point (so that the entire transformation occurs in the solid state). The thermal budget required for dewetting, i.e. to start atomic diffusion, can be obtained by standard thermal annealing as well as laser, ion or electron beam irradiations [Ruf15].

The mean droplets (nanoparticles) radius $\langle r \rangle$ and spacing (surface to surface distance) $\langle s \rangle$ depends on the thickness of the film with a power-

law relation. For a given thickness, the final dimension and spacing of the nanoclusters will be mostly determined by the annealing temperature ($\propto e^{-\frac{1}{kT}}$) and, more weakly, by the annealing time ($\propto \sqrt{t}$).

3.2 Au nanoparticles on polycrystalline anatase and rutile

3.2.1 Phases of TiO_2 thin films

Titanium dioxide exists in three polymorphs: rutile, anatase (both tetragonal) and brookite (orthorhombic) [Han11]. While rutile is the stable phase, both anatase and brookite are metastable. The latter is difficult to synthesize and so TiO_2 is commonly studied in rutile or anatase phase [Bel06]. Only anatase and rutile have been observed in thin films [Tin02] [Che06][Che09][Zha09][Han11]. Amorphous TiO_2 films are formed if the substrate temperature during deposition is low [Löb94] [Han11]. Whether one finds anatase, rutile, or amorphous phase in evaporated or sputtered films, depends on the details of the deposition. It has been demonstrated that the main parameters that determine the phase formed are the energy of the impinging atoms and the substrate temperature [Sch81][Löb94]; in Fig. 3.3 the occurrence of amorphous, anatase or rutile phase is shown. The nucleation of rutile is favored by energetic particles impinging on the substrate.

According to our experimental observation, only amorphous phase is observed from both sputtering and evaporation at room temperature. After thermal annealing of the deposited films it is possible to observe rutile or anatase. The growth of anatase in an amorphous matrix is strongly favored with respect to rutile. This can be understood from the difference in the density of the involved phases. In fact, the density of the amorphous film (3.20-3.65 g cm^{-3}[Han11][Löb94]) is much lower than the density of rutile (4.25 g cm^{-3}[Han11]). Therefore, the formation of rutile from an amorphous matrix requires a stronger densification meaning more elastic

energy than the formation of anatase which has a density of $3.20 - 3.65\ \mathrm{gcm}^{-3}$ [Han11].

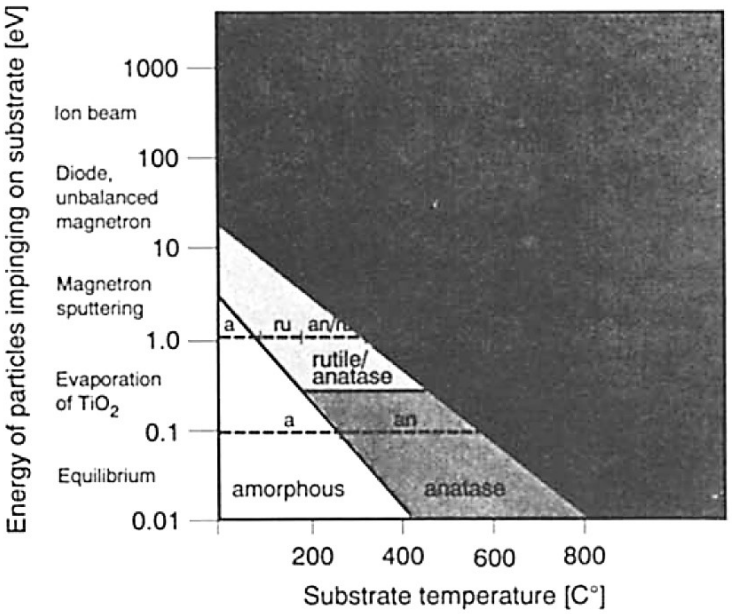

Figure 3.3: The diagram shows qualitatively the conditions for the occurrence of amorphous ('a'), anatase ('an') or rutile ('r') TiO_2 films. Substrate temperature and energy of the particle impinging on the substrate are relevant parameters. Taken from ref. [Löb94].

Moreover, it has been demonstrated, by thermodynamic arguments that the phase stability of TiO_2 also depends on the crystallite size [Zha98]. Indeed, when both the bulk and surface energy are taken into account it comes out that anatase is more stable than rutile in fine grained TiO_2, as long as the crystallite size is smaller than 14 nm [Zha98].

Thus, in general, one can control the phase formed in a TiO_2 film by a proper choice of the growth procedure.

3.2.2 TiO_2 films growth and characterization

In this paragraph we describe the procedure followed to form anatase and rutile TiO_2 films. The stoichiometry and the thickness of the films were checked by Rutherford Backscattering Spectrometry (RBS), using a 2 MeV He^+ beam with a scattering angle of 165°. We performed two different processes:

1) Sample #1: Ti film was grown by DC sputtering (P = 3 kW, Ar flow = 48 sccm, low pressure 10^{-3} mbar, t = 28 s) on 85 nm thick thermal SiO_2 on Si wafer. In these conditions a 100 nm thick film of pure Ti was formed as detected by RBS.
2) Sample #2: Ti based film was deposited by reactive evaporation of Ti in O_2 atmosphere ($5 \cdot 10^{-4}$ mbar) on quartz. According to RBS analysis, a 260 nm thick TiO_2 films was obtained.

Both samples were subsequently annealed at 600°C, 30 min in 2.5 lpm of O_2 flow using a standard Carbolite horizontal furnace.

Crystal structure of TiO_2 was determined by X-ray diffraction (XRD, Bruker D-9000, Cu Kα, 40 kV, 40 mA, at 0.01° s^{-1}) and Bruker diffraction suite software was used for the diffraction analysis.

SEM analyses were performed with a Zeiss FEG-SEM Supra 25 Microscope operating at 5 kV at a working distance of 4 mm. SEM images were analyzed by Gatan Digital Micrograph software.

AFM analyses were performed with a Veeco-Innova microscope operating in high amplitude mode, and ultra-sharpened Si tips were used (MSNL-10 from BRUKER). AFM images were analyzed by SPM LabAnalyses V.7.1 software.

Optical properties were measured in the wavelength range of 200-1000 nm using a Perkin-Elmer UV-Vis Lambda 40 spectrophotometer.

For the discoloration tests we referred to the guidelines of the ISO 10678:2010 [Mil12]. According to the standard, 10 µl of methylene blue (MB) solution (0.05 wt.%) were added to each 1 ml volume of deionized Milli-Q water (resistivity 18 MΩ·cm). The MB concentrations were measured according to the Lambert-Beer law at 664 nm (extinction

coefficient 7.4×10^4 M^{-1} cm^{-1}). During the tests, each sample was placed at the bottom of a cylindrical vessel having a base area of 2 cm^2 filled with 2 ml of the MB-water solution. The solutions were left for one hour in dark to allow the adsorption of MB onto films and vessels surfaces and then illuminated with UV light. During light irradiation the vessels were covered with quartz in order to avoid evaporation during irradiation. The wavelength of the UV light source was centered at 368 nm (FWHM lower than 10nm) and UV irradiance was 1.1 mW/cm^2.

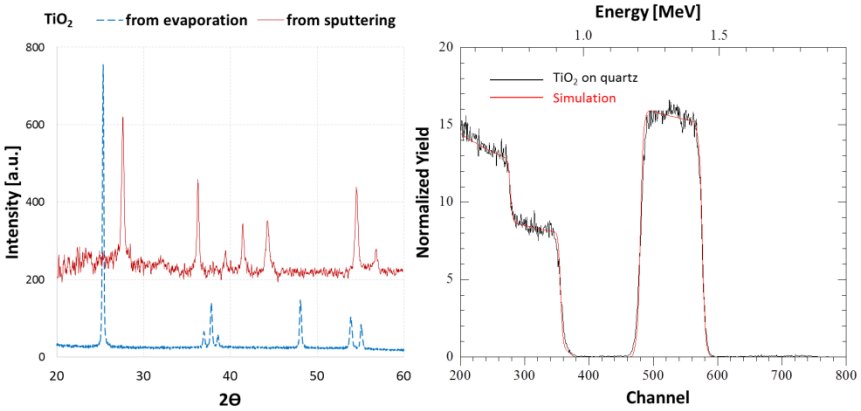

Figure 3.4: (Left) XRD spectra of the two TiO_2 substrates clearly evidenced the presence of a single phase film of anatase, starting from evaporation of TiO_2 on quartz, or a single phase film of rutile, starting from sputtered Ti on SiO_2/Si, after the annealing treatment at 600 °C in oxygen atmosphere. (Rigth) RBS spectra of the sample of TiO_2(anatase)/quartz. From ref. [Cac15].

After the annealing treatment at 600 °C, the film grown by evaporation showed the characteristic XRD peaks of anatase, while the film grown by sputtering the peaks of rutile (Fig. 3.4 left). No mixed phase was observed. An RBS spectra of the anatase film on quartz is shown in Fig. 3.4 (right), together with the simulation of a TiO_2 film of $2500 \cdot 10^{15}$ at/cm^2 onto quartz (SiO_2). The accordance between data and simulation confirmed that the film had the expected stoichiometry. Similar results have been

extracted from RBS spectra of the rutile film on SiO_2/Si. It is worth noting that we obtained two different titanium dioxide crystal phases following the same annealing treatment. This is possible even if rutile is the most stable phase, depending on the elaboration conditions [Löb94][Han11].

The thicknesses of the two titanium dioxide films have been evaluated both by means of RBS and optical measurements, resulting in 260 ± 5 nm for anatase and 165 ± 5 nm for rutile film.

3.2.3 Au nanoparticles on TiO_2: structural and morphological characterization

Au depositions were carried out on the polycrystalline TiO_2 using a RF (60Hz) Emitech K550x Sputter coater apparatus, clamping the substrates against the cathode located straight in front of the source (99.999% purity target). The electrodes were laid at a distance of 40 mm under Ar flow, keeping a pressure of 0.02 mbar in the chamber. After 120 s of deposition, at an emission current of 10 mA, a nominal thickness (checked by RBS) of $\mathrm{d} = 3\ \mathrm{nm}$ of Au was deposited. After Au depositions, the samples were annealed in vacuum (pressure $6 \cdot 10^{-3}$ mbar), at 400°C for 60 min.

TiO_2 and Au/TiO_2 SEM and AFM images are shown for both anatase and rutile substrates (Fig.3.5). Note that the morphology of the original TiO_2 substrates was different, essentially due to the diverse deposition techniques. However, as we discuss in the following, a similar Au NPs film has been obtained on both substrates. We extracted the percentage of covered surface, the mean NPs radius and NPs density by SEM images analysis. The parameters were obtained from a statistical population of about 2500 NPs.

The generic distribution of radii, *R*, was fitted using the log-normal function [Gra76]. The particles density was obtained counting the number of particles sampled on a certain area. We estimated the inter-particle mean surface to surface distance $\langle s \rangle$ by means of these parameters as $\langle s \rangle = \frac{1}{\sqrt{N}} - 2\langle R \rangle$, being *N* the particles density and $\langle R \rangle$ the mean radius. The results are summarized in Table 3.1.

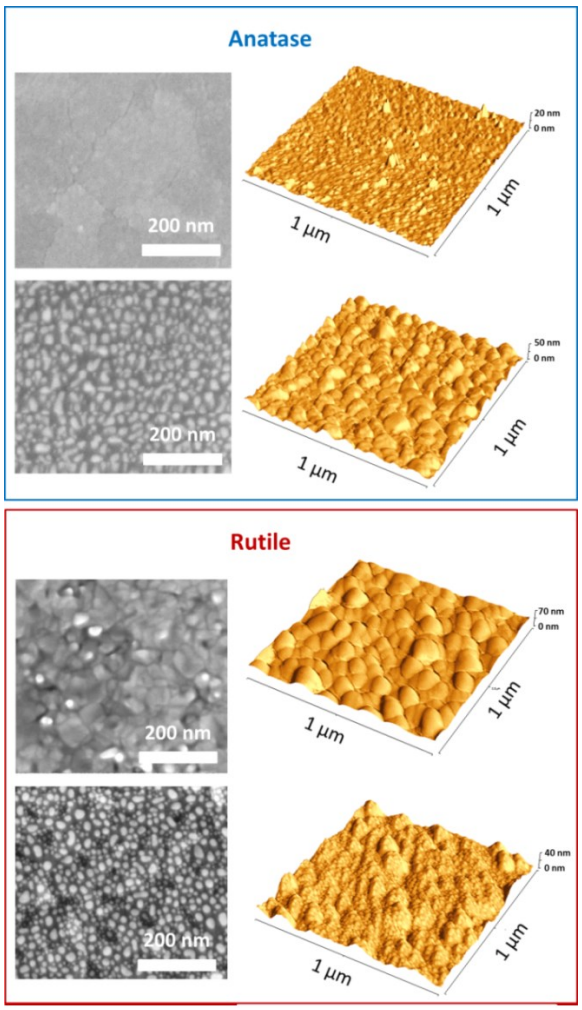

Figure 3.5: Comparison of the SEM and AFM images of the bare TiO_2 and Au/TiO_2 films for anatase and rutile phase. Adapted from ref. [Cac15].

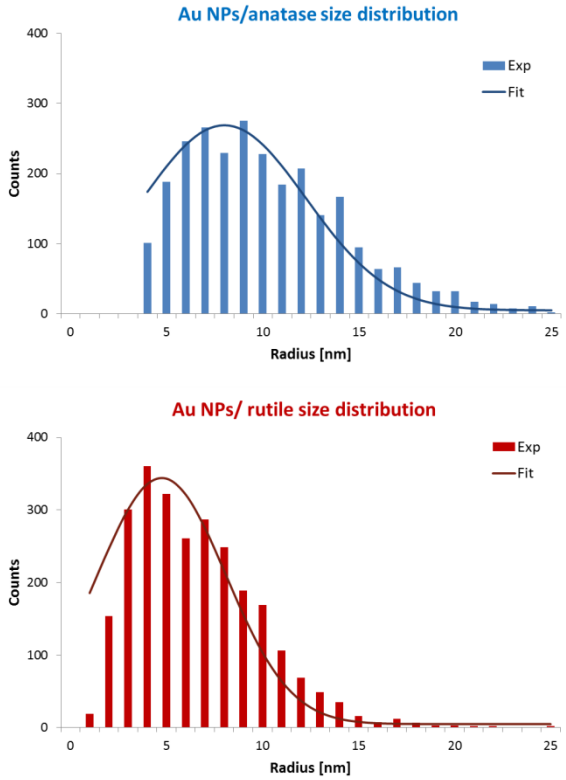

Figure 3.6: Size distributions of Au nanoislands on TiO_2 substrates. The width of the distributions is typical of the dewetting of a metal film. From ref. [Cac15].

Table 3.1

Au on	Surface coverage	Mean radius	Density [NPs/cm^2]	Mean distance
Anatase	31 ± 1 %	9 ± 4 nm	9.94 ± 0.08 E+10	13 ± 4 nm
Rutile	30 ± 1 %	6 ± 3 nm	16.2 ± 0.1 E+10	12 ± 3 nm

Despite the difference in the roughness of the two TiO_2 substrates (mainly due to the deposition techniques), and in surface free energy [Zha98], we obtained a gold nanoislands film with the same surface covertures and particle-to-particle average distances.

In Fig.3.6 the size distribution of the two nanocomposite films are reported. It is worth noting that the breadth of these distributions may turn advantageous from an optical point of view. Indeed, since the surface plasmon resonance of metal nanostructures strongly depends on the shape and size of nanoparticles [Kel03][Nog07], such a broad range of diameters means that the resonance will occur in a wider range of visible spectrum, as confirmed by optical response.

3.2.4 Optical characterization

The transmittance of the quartz substrate, anatase, Au-as deposited and Au NPs-anatase films is shown Fig.3.7 (a). The oscillations of the spectra are due to the interference at TiO_2–substrate interface. We can observe a reduction in the transmittance of the Au-as deposited film, while we do not observe shift in the position of the maxima and minima. In the range between 350 nm and 550 nm similar behavior is shown by the Au NPs-anatase film. Instead, in the range between 550 nm and 750 nm we can see a decrease in the transmittance of the nanostructured film due to the plasmonic absorption of metal nanostructures. Indeed, the plasmon resonance of such gold nanoparticles film lies in this spectral range.

The reflectance of the rutile, Au-as deposited and Au NPs-rutile films is shown in Fig. 3.7 (b). The differences in reflectivity spectra are evident in the range between 600 nm and 900 nm. Once again, we address the shape of Au NPs composite film spectra to a plasmonic resonance of metal nanostructures on the surface of the film.

Thus optical measurements on the TiO_2 substrates, Au-as deposited and Au NPs- TiO_2 films clearly evidence the presence of a plasmon resonance in the range between 550 nm and 750 nm, as already reported by Liu *et al.* [Liu11].

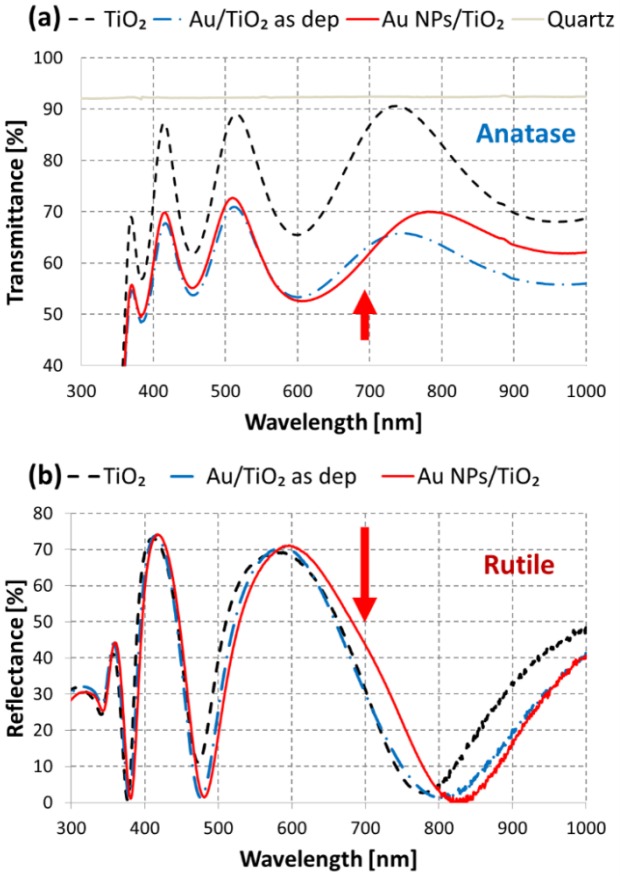

Figure 3.7: (a) Transmittance spectra of anatase/quartz, Au-as deposited/anatase/quartz and Au-NPs/anatase/quartz films. (b) Reflectivity spectra of rutile/SiO_2/Si, Au-as deposited/rutile/SiO_2/Si and Au-NPs/rutile /SiO_2/Si films. The arrows evidence the region of plasmon resonance. From ref. [Cac15].

The main effect of the wide distribution of the nanoislands radius is the broadening of the plasmon resonance peak. Relevantly, the influence of the substrate refractive index (n_{TiO_2}~2.7) at the plasmon resonance has a twofold effect, inducing at the same time a redshift of the Au NPs expected plasmon resonance peak position (that is expected at about 500 nm in air

for the specific size) and an enhancement in the quality factor of resonance [Mie08].

3.2.5 Photoactivity evaluation and effect of the Au nanostructures under UV illumination

In order to check the activity of our samples, we performed tests following the ISO 10678:2010 [Mil12]. The results of the discoloration experiments are summarized in Fig. 3.8, where the MB discoloration rate constant normalized to the macroscopic surface area is shown. The results in Fig. 3.8 show, apparently, a decrease in the UV efficiency of TiO_2 films in presence of the Au NPs.

In agreement with literature data indicating that anatase is a better photocatalyst, at least for the family of compounds similar to MB [Ryu08][Lut14], we found a higher discoloration rate in anatase TiO_2 film. The photocatalytic activity of the Au/TiO_2 composite films decreased for both anatase and rutile with respect to the bare TiO_2 substrate.

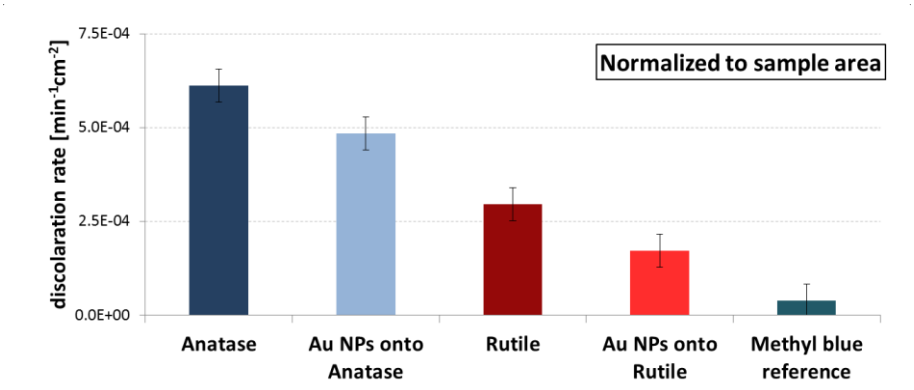

Figure 3.8: The value of the discoloration rate extracted by the measure of MB absorption versus time under UV illumination. The MB reference is reported for comparison. From ref. [Cac15].

However, if we report (Fig. 3.9) the discoloration rate normalized to the percentage of area not covered by NPs (about 70%) it comes out that the reaction rate is rather equal to the one of the original TiO_2 film.
More in detail, the discoloration rate *k* has been normalized according to $k_{norm} = \frac{k}{f_{exposed}}$, where $f_{exposed}$ is the fraction of the substrate surface area not covered by Au nanostructures (i.e. exposed). Being the Au surface coverage 30%, this fraction is the 70% of the total surface of the sample ($f_{exposed} \approx 0.7$). This means that the sputtering and the annealing of the gold film and the presence of metal islands, at the given density and particles dimension, are not affecting the TiO_2 substrate, even though are not giving an enhancement under UV.

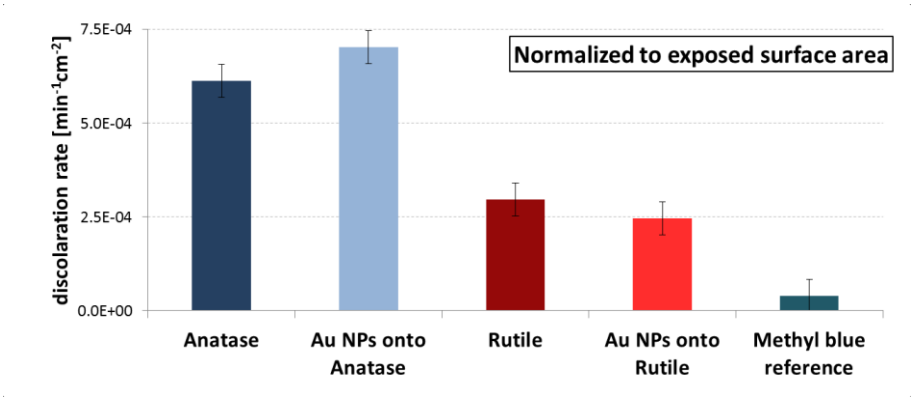

Figure 3.9: The reaction rate corrected for the real exposed surface area, that is the 70% of the physical surface of the sample, since the Au nanoislands film coverture reaches the 30% for both anatase and rutile substrates. From ref. [Cac15].

3.3 Conclusions

Two different phases (anatase and rutile) TiO_2 films were prepared. Gold nanostructures with similar average radius, surface coverage and particle-to-particle distance have been obtained by dewetting on both

anatase and rutile films. The optical response of the Au nanoislands films clearly showed the fingerprint of gold plasmon resonance. In the UV range the overall photocatalytic efficiency decreases in presence of the Au nanoparticles because of the consequent reduction of the exposed TiO_2 area. However, when looking at the reaction rate corrected for the real exposed surface area illustrates that the presence of gold nanostructures does not affect the properties of the active substrate, i.e. it does not seem to introduce defects and/or detrimental surface states. Therefore these substrates are eligible as ideal candidate for visible driven photocatalysis. Further enhancement in UV range photoactivity could be reached provided the encapsulation of the nanostructures into the TiO_2 matrix, as will be discussed in the next chapters. This strategy will combine the effect of the presence of metal NPs and the exposure of the active surface to the environment.

3.4 References

[Bel06]A. Beltran , L. Gracia , J. Andres, J. Phys. Chem. B, **110**, 23417 (2006).
[Bon09] D. Bonn, J. Eggers, J. Indekeu, J. Meunier, E. Rolley, Rev. Mo. Phys., **81**, 739 (2009).
[Cac15] G. Cacciato, F. Ruffino, M. Zimbone, R. Reitano, V. Privitera, M. G. Grimaldi, Mat. Sci. Sem. Proc. (2015)
http://dx.doi.org/10.1016/j.mssp.2015.07.074
[Che06] L. Chen, M. E. Graham, G. Li, K. A. Gray, Thin Solid Films, **515,** 1176–1181 (2006).
[Che09] L. Chen, M. E. Graham, G. Li, D. R. Gentner, N. M. Dimitrijevic, K. A. Gray, Thin Solid Films, **517,** 5641–5645 (2009).
[Cui08] Z. Cui, Nanofabrication: Principles, *Capabilities and Limits* (Springer, New York, 2008).
[deG85] P. G. de Gennes, Rev. Mo. Phys., **57**, 827 (1985).

[Fel02] D. L. Feldheim and C. A. Foss, Jr. (Eds.) *Metal Nanoparticles: Synthesis, Characterization, and Applications* (Marcel Dekker, Inc, New York, 2002).
[Geo03] M. Geoghegan, G. Krausch, Prog. Pol. Science, **28**, 261 (2003).
[Gra76] C. G. Granqvist, R.A. Buhrman, J. Appl. Phys., **47**, 2200-2219 (1976).
[Han11] D. A. H. Hanaor, C. C. Sorrell, J. Mater. Sci. , **46**, 855-874 (2011).
[Hen05] S. J. Henley, J. D. Carey, S. R. P. Silva, Phys. Rev. B, **72**, 195408 (2005).
[Her08] S. Herminghaus, M. Brinkmann, and R. Seemann, Annu. Rev. Mater. Res., **38**, 101 (2008).
[Hou13] W. Hou, S. B. Cronin, Adv. Funct. Mater., **23**,1612–1619 (2013).
[Kel03] K. L. Kelly, E. Coronado, L. L. Zhao, G. C. Schatz, J. Phys. Chem. B, **107**, 668-677 (2003).
[Kwo03] J.-Y. Kwon, T.-S- Yoon, K.-B. Kim, S.-H. Min, J. App. Phys., **93**, 3270 (2003).
[Joh12] R. L. Johnston and J. Wilcoxon (Eds.), *Metal Nanoparticles and Nanoalloys* (Elsevier, Oxford, 2012).
[Lég92] L. Léger, J. F. Joanny, Rep. Prog. Phys., **55**, 431 (1992).
[Lin11] S. Linic, P. Christopher, D. B. Ingram, Nature Materials, **10**, 911–921 (2011).
[Lin12] N. C. Lindquist, P. Nagpal, K. M. McPeak, D. J. Norris, and S.-H. Oh, Rep. Prog. Phys., **75**, 036501 (2012).
[Liu11] Z. Liu, W. Hou, P. Pavaskar, M. Aykol, S. B. Cronin , Nano Letters, **11**, 1111-1116 (2011).
[Löb94] P. Löbl; M. Huppertz, D. Mergel, Thin Solid Films, **251**, 72-79 (1994).
[Lon06] L. Longstreth-Spoor, J. Trice, C. Zhang, R. Kalyanaraman, J. Phys. D, **39**, 5149 (2006).
[Lut14] T. Luttrell, S. Halpegamage, J. Tao, A. Kramer, E. Sutter, M. Batzill, Sci. Rep., **4**, 4043 (2014); DOI:10.1038/srep04043.
[Mie08] G. Mie , Ann. Phys., **25**, 377 (1908).
[Mil12] A. Mills, C. Hill, P. K. J. Robertson, J. Photochem. Photobiol. A, **237**, 7-23 (2012).
[Mül03] P. Müller-Buschbaum, J. Phys.: Condens. Matter, **15**, R1549 (2003).

[Nog07] C. Noguez, J. Phys. Chem. C, **111**, 3806-3819 (2007).
[Ruf15] F. Ruffino, M. G. Grimaldi, Phys. Status Solidi A, 1–23 (2015) / DOI 10.1002/pssa.201431755.
[Ryu08] J . Ryu, W. Choi, Environ. Sci. Technol., **42**, 294–300 (2008).
[Sau12] T. K. Sau and A. L. Rogach (Eds.), *Complex-shaped Metal Nanoparticles: Bottom-up Syntheses and Applications* (Wiley-VCH, Weinheim, 2012).
[Sch81] S. Schiller, G. Beister, W. Sieber, G. Schirmer, E. Hacker, Thin Solid Films, **83**, 239-245 (1981).
[Tin02] C.-C. Ting, S.-Y. Chen, D.-M. Liu, Thin Solid Films, **402**, 290-295 (2002).
[Tho12] C. V. Thompson, Annu. Rev. Mater. Res., **42**, 399 (2012).
[Zha09] Y. Zhang, X. Ma, P. Chen, D. Yang, J. Alloys Compd., **480**, 938-941 (2009).
[Zha98] H. Zhang, J. F. Banfield, J. Mater. Chem., **8(9)**, 2073–2076, (1998).

Chapter 4 TiO_2 subsurface embedded Ag nanoparticles via low energy ion beam synthesis

Low Energy Ion Beam Synthesis (LE-IBS) is an original technique that allows obtaining metallic nanoparticles (NPs) assemblies, with controlled size and density, few nm close to the free surface of a hosting oxide matrix. Engineering the optical response, film thickness and size of the nanoparticles embedded in this matrix we are able to take simultaneously advantage of spectrally and spatially localized surface plasmon resonance (LSPR) and optical amplification.

We present, in this section, the results on a novel Ag/TiO_2 nanocomposite films produced by LE-IBS. Combining TiO_2, characterized by a high refractive index, with Ag, known for its excellent plasmonic properties, we obtained a highly enhanced optical response in the visible range. Indeed, in comparison with bare TiO_2, the Ag/TiO_2 composite film shows up to 20 times higher optical signal when the exciting wavelength is close to LSPR and the matrix thickness matches the antireflective condition. The nanocomposite films have been deeply investigated by means of Raman spectroscopy, enlightening the signature of an efficient free carriers transfer into the TiO_2 matrix from Ag NPs.

4.1 Optical engineering

Photocatalytic reactions are always the result of complex and concurring processes occurring at the nanoscale. These processes are: (i) the absorption of light creating electron–hole excitations in a thin film of a semiconducting compound, (ii) the separation followed by (iii) the transfer of these charges to the free surface in contact with water or air, (iv) their interaction with organic or inorganic molecules located on this surface through oxidation and reduction reactions, leading finally (v) the electronic system to recover its ground state. Plasmonic metal nanoparticles can improve light absorption in the visible range by means of their localized

surface plasmon resonances (LSRP) and thus enhance the photocatalytic efficiency [Lin11][Hou13]. In order to enhance the efficiency of the preceding processes (from i to iv), devices need to be designed with plasmonic substrates that can effectively absorb the entire solar spectrum, thus harvesting energy from sunlight.

4.1.1 Low energy ion beam synthesis (LE-IBS)

During the 1990s ion implantation became an important and widely used technique for synthesizing nanocomposite materials, especially in the field of semiconductor devices. The popularity of ion implantation was due, in part, to its versatility and flexibility. In this technique, a selected host material is injected with energetic ions that are accelerated from a few tens to a few thousand kilovolts. High-dose implantation can create a solid state supersaturation of the implanted ions in a layer extending from the specimen surface to a depth of several tens to hundreds of nanometers. Subsequent thermal processing or further ion (or electron) irradiation can, depending on the specific host/nanoparticle solid state chemistry, induce the implanted material to precipitate as discrete nanoparticles. The versatility of the implantation technique arises from the fact that essentially any element in the periodic table can be implanted into virtually any selected host material. Moreover, the average precipitate size, depth and density can be tuned selecting the appropriate dose, dose rate, energy and annealing temperature. This versatility and the various possible combinations of implanted ions allow, in principle, for an extremely large range of potential nanoparticle-host combinations [Mel01].

In particular, low-energy ($E_{beam} \leq 50$ keV) ion implantation offers potential for control of nanocrystal size in layered structures. At low energy and high beam current density, deposition time and range straggling are minimized, while depth uniformity is simultaneously maximized. Recently, this methodology has successfully been optimized for the synthesis of Ag NCs delta layers for large-scale plasmonic structures [Car09][Far10][Ben13]. In Fig. 4.1 is shown an example of a delta layer of silver nanoclusters embedded in a silica matrix by means of Low Energy Ion Beam Synthesis (LE-IBS).

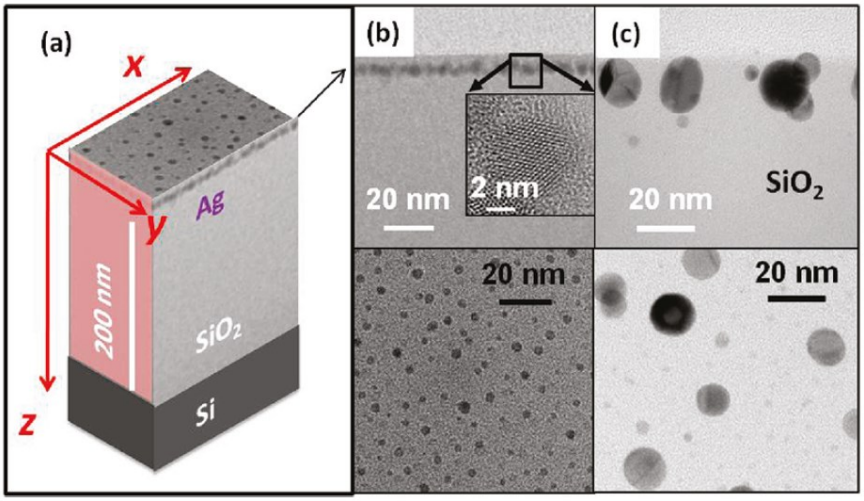

Figure 4.1: (a) 3D montage coupling the cross-section view (z axis) and the plan-view (x, y) of an Ag/SiO_2 composite system obtained via LE-IBS; (b) cross-sectional TEM image (defocused bright field) of the sample implanted at 3 keV with $4.7 \cdot 10^{15}$ ions/cm^2 and (c) at 20 keV with $3.1 \cdot 10^{16}$ ions/cm^2. In inset of panel b, HREM image of an isolated Ag nanocrystal; (d and e) associated plan-view observations. From ref. [Car11].

Photocatalytic reactions are always the result of complex processes that require the generation of carriers within the photoactive substrate, their subsequent separation and transfer to the free surface in contact with air or water and their interaction with molecules in solution. As a matter of fact, grafting TiO_2 with small Ag NPs can enhance its photocatalytic activity under UV light due to intrinsic intraband electronic transitions in silver, as well as promote the optical response of TiO_2 in the visible range due to Localized Surface Plasmon Resonances (LSPR). Furthermore, Ag nanoparticles are buried just beneath the surface of the oxide matrix, so that:

1. NPs will have a plasmon resonance, in the visible range, close to the interface;
2. the free surface of the catalytic material would maintain the exposure of the chemically active substrate to the environment;

3. this encapsulation can effectively protect silver nanoparticles against oxidation.

4.1.2 Optical amplification

In order to introduce the concept of optical amplification, let's consider a perfect mirror with a film of refractive index *n* grown on its surface. Let's consider a monochromatic wave in normal incidence on this film. It is well known that an electromagnetic wave, passing through a film and being reflected backward, will undergo to a phase shift δ:

$$\delta = \frac{2\pi t}{\lambda_n} \tag{4.1}$$

where *t* is the film thickness and λ_n the wavelength in the medium. When measuring the reflectivity of a thin film on substrate, we obtain constructive interference for $2\delta = 2\pi m$, destructive interference for $2\delta = (2m+1)\pi$, being *m* an integer. Thus, the thicknesses at which destructive or constructive interference occur are given by:

$$t = \frac{m\lambda_n}{2} \tag{4.2a}$$

$$t = \frac{(2m+1)\lambda_n}{4} \tag{4.2b}$$

It is worth noting that in destructive interference conditions, the electromagnetic field intensity at the air-film interface is at maximum. Indeed, in stationary state, thus considering the incident and reflected beam, we observe a node at the (perfect) mirror-dielectric interface; if we look at the intensity of the electromagnetic field ($\propto \mathcal{E}^2$) versus the distance from the mirror, we can observe a maximum of the intensity of field at:

$$d = \frac{(2m+1)\lambda_n}{4} \qquad (4.3)$$

Note how this distance equals the condition 4.2b, stating the antireflectivity conditions (i.e. destructive interference).

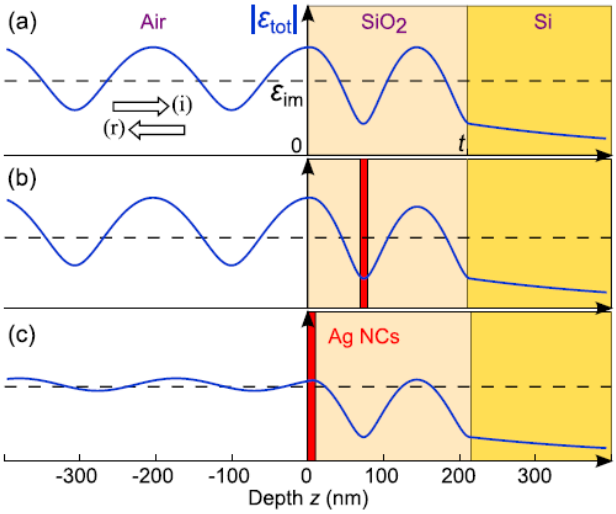

Figure 4.2: Variation vs depth of the amplitude of the total (incident *i* + reflected *r*) electric field $|\mathcal{E}_{tot}| = |\mathcal{E}_i + \mathcal{E}_r|$: (a) without Ag NCs, (b) with a plane of Ag NCs located at a node of the electric field into the dielectric layer, and (c) with this plane located at an antinode of the electric field near the dielectric/air interface. From ref. [Bay14].

In Fig. 4.2 are shown the calculation made by Bayle et al. [Bay14] in the case of a SiO_2/Si substrate. In this case, the wavelength in vacuum is chosen at 413 nm (in coincidence with the plasmon frequency of Ag NPs in SiO_2), the thickness of the layer is 210 nm (antireflectivity condition for the chosen wavelength), the incidence is normal. Firstly, one observes that, under these antireflectivity conditions, the intensity of the total electromagnetic field is maximum at the air/SiO_2 interface. Indeed, in Fig. 4.2a the total electromagnetic field (resulting from incident and reflected electromagnetic waves) shows a maximum at the free surface of the matrix: the film thickness matches the condition (4.2b), that is equal to condition

(4.3). This means that the film is in antireflective conditions. In Fig. 4.2b and 4.2c, a layer of Ag NCs (the particles diameter 5 nm and the amount of silver equals $5 \cdot 10^{16}$ atoms/cm^2) is placed into the oxide matrix. As it is possible to observe from the total electromagnetic field intensity, the same layer of Ag nanoparticles can show or not an enhanced optical response depending on the position, respectively at a minimum (Fig.4.2b) or at a maximum (Fig.4.2c) of the field.

Therefore, engineering the architecture of the stacking layers is the key to take simultaneously advantage of spectrally and spatially LSPR but also of optical amplification. This has been recently proposed for enhanced spectroscopy and imaging [Car11].

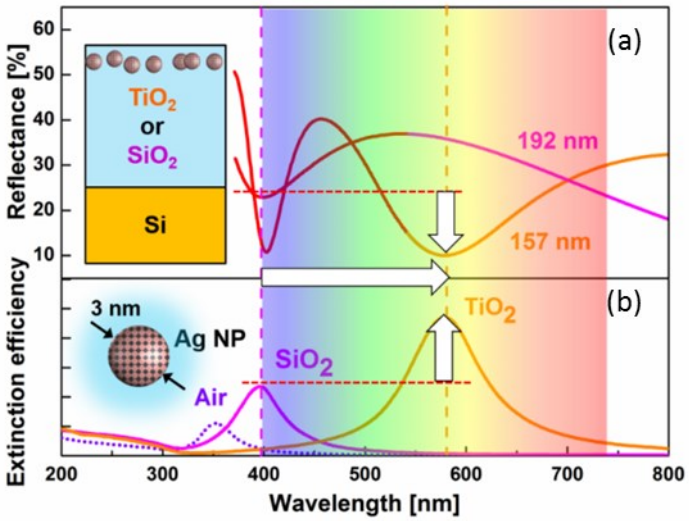

Figure 4.3: Theoretical simulation illustrating the tuning of anti-reflectivity condition in a SiO_2 (or TiO_2)/Si heterostructure and LSPR in a silver nanoparticle of diameter D = 3 nm. From ref. [Cac15].

By choosing an appropriate thickness of a TiO_2 layer deposited on a silicon substrate, one can easily tune the spectral position of one of the antireflective minima in such a way it can match the LSPR. In particular, in Fig. 4.3b is shown the extinction efficiency of a silver nanosphere (3 nm in

diameter) embedded in air ($n = 1$), SiO_2 ($n \approx 1.4$) or TiO_2 ($n \approx 2.7$). We can observe how the LSPR redshifts and, at the same time, increases its quality factor as the refractive index of the embedding medium increases. This is due to the higher confinement of the electromagnetic field in high refractive index materials [Boh83][Kel03]. In Fig. 4.3a is shown the reflectance of a SiO_2 (or TiO_2)/Si heterostructure with embedded a Ag NPs layer. By choosing the proper film thickness, i.e. matching the antireflectivity conditions for the wavelength at which plasmon resonance occurs, it is possible to obtain an enhanced optical response from the NPs layer.

The aim of the work presented in this section is to take benefit of this phenomenon in multilayer stacking containing TiO_2 and embedding Ag NPs. They will be adapted to manage amplifying processes in the visible range by exploiting simultaneously the resulting optical interference phenomenon and LSPR.

4.2 TiO_2 subsurface embedded Ag NPs

4.2.1 Materials and methods

TiO_2 has been obtained by thermal oxidation (600°C, 30 min in 2.5 lpm of O_2 flow using a standard Carbolite horizontal furnace) of Ti films grown by DC sputtering (P = 3 kW, Ar flow = 48 sccm, low pressure 10^{-3}mbar) on thermally oxidized Si wafers. The SiO_2 layer thickness was 85 nm and two Ti film thicknesses (50 and 100 nm) were chosen so that, after oxidation, we obtained correspondingly around 90 nm and 165 nm TiO_2 films, referred as sample A and B, respectively.

Crystal structure of TiO_2 was determined by X-ray diffraction (XRD, Bruker D-9000, Cu Kα, 40 kV, 40 mA, at 0.01° s^{-1}) and Bruker diffraction suite software was used for the diffraction analysis.

Silver ions (Ag^+) have been implanted in the TiO_2 layer with low energy (20 keV) and a fluence of 3×10^{16} ions/cm^2 by means of a Varian 200A2 implanter. According to SRIM simulations [Bie80] the implanted profile is expected to reach its maximum at a depth of 10 nm with a

straggle of 2.5 nm. A part of the free surface has been masked during implantation to get a reference signal in order to check the plasmon resonance effect on vibrations and carriers in the TiO_2 layer.

The composition and thickness of the films, before and after implantation, were checked by Rutherford Backscattering Spectrometry (RBS), with a 3.5 meV HVEE Singletron accelerator, using a 2 meV He+ beam with a scattering angle of 165° in normal incidence.

Microscopy imaging was performed using a field emission Transmission Electron Microscope, FEI Tecnai™ F20 microscope operating at 200 kV, equipped with a spherical aberration corrector dedicated for high quality High Resolution Electron Microscopy (HREM) images with an increased signal/noise ratio and nearly no delocalization effect at surfaces and interfaces. Energy Filtered TEM (EFTEM) imaging was conducted with a TRIDIEM Gatan imaging filter attached to the microscope and coupled to a scanning stage for the STEM-EELS analyses. TEM lamellae transparent to electrons were prepared in cross-section by mechanical grinding and Ar^+ ion milling.

The UV-VIS optical characterization was obtained by extracting 6° reflectance spectra in the 200-800 nm wavelength range, by using a Varian Cary 500 double beam scanning UV/VIS/NIR spectrophotometer. Raman spectra were recorded over a wide frequency range using an XploRA Horiba Jobin Yvon spectrometer. The laser illumination at 532 or 638 nm was lower than 1 mW to avoid any heating of the sample. Some very low frequency Raman-Brillouin spectra were recorded using a specifically modified version of a T64000 Horiba Jobin Yvon spectrometer and a Krypton laser tuned at the 530 nm line.

For the discoloration tests we referred to the guidelines of the ISO 10678:2010 [Mil12]. According to the standard, 10 µl of methylene blue (MB) solution (0.05 wt.%) were added to each 1 ml volume of deionized Milli-Q water (resistivity 18 MΩ·cm). The MB concentrations were measured according to the Lambert-Beer law at 664 nm (extinction coefficient $7.4 \cdot 10^4$ M^{-1} cm^{-1}). During the tests, each sample was placed on the bottom of a circular vessel of 2 cm^2 filled with 2 ml of the MB-water solution. The solutions were left for one hour in dark to allow the absorption of MB onto film and vessels surfaces and then illuminated with

UV or visible (blue) light. During light irradiation the vessels were covered with quartz in order to avoid evaporation during irradiation. The wavelength of the UV light source was centered at 368 nm (FWHM lower than 10nm) and UV irradiance was 1.1 mW/cm^2. The wavelength of the visible light source was centered at 453 nm (FWHM 40nm) and irradiance was 1.5 mW/cm^2. In this latter experimental condition, a UV filter was used in order to cut the wavelengths below 420 nm. The degradation rate was measured along time.

4.2.2 Structural characterization: TEM imaging

TiO_2 rutile phase was observed in XRD measurements. The thicknesses (90 ± 4 nm and 165 ± 4 nm for sample A and B, respectively) and the stoichiometry ($[O]/[Ti] = 2 \pm 0.1$) of the bare TiO_2 substrates before implantation were extracted by RBS. Moreover, since RBS is sensitive to Ag dissolved in the matrix, even if not clustered, it was possible to evaluate the amount of Ag after implantation. Thus the analysis of the Ag peak resulted in 1.1 ± 0.1 at/cm^2 dispersed in 18 ± 2 nm of TiO_2 matrix. The measured thicknesses of titania layers after implantation were respectively 83 ± 4 nm and 161 ± 4 nm. This result, together with a reduced dose of Ag in the matrix, can be explained by some sputtering occurred during implantation.

A cross-section Bright Field TEM image of sample A at low magnification (Fig. 4.4) shows the stacking of two layers on top of a Si substrate: TiO_2 with thickness $t_{TiO_2} = 91 \pm 4$ nm deposited on SiO_2 ($t_{SiO_2} = 84 \pm 3$ nm). In the region close to the surface the presence of a band of nanoparticles is detected, with average diameter $D \approx 3$ nm (see Figs 4.4 and 4.5a). The Ag NPs have nucleated during the implantation process and no annealing procedure was necessary for the phase separation. The Ag NPs are located in a 14 ± 1 nm thick band near the free surface. This is in good agreement with the SRIM simulations of the implanted profile, which peaks at a depth of 10 nm with a straggle of 2.5 nm. The region damaged by the implantation process, referred in what follows as “amorphous-like” TiO_2 (a-TiO_2), is around 20 nm thick.

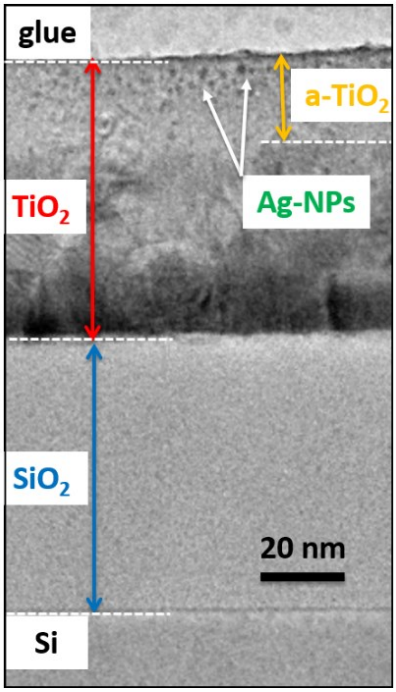

Figure 4.4: TEM cross-section image of sample A, observed in Bright Field, showing the different stacked layers. Adapted from ref. [Cac15].

These nanoparticles are made of pure silver, as confirmed by the mapping performed in the surface region by EFTEM (shown in Fig. 4.5c) when filtering at the Ag M45 core loss edge (467 eV). The associated HREM zero-loss image (Fig. 4.5a) indicates that these Ag NPs are crystalline. The interatomic distances measured using the Fast Fourier Transform (FFT, see Fig. 4.5b) of an individual Ag nanocrystal are the ones expected for metallic silver. The nanocrystal imaged in Fig. 4.5b is oriented following the (110) zone axis.

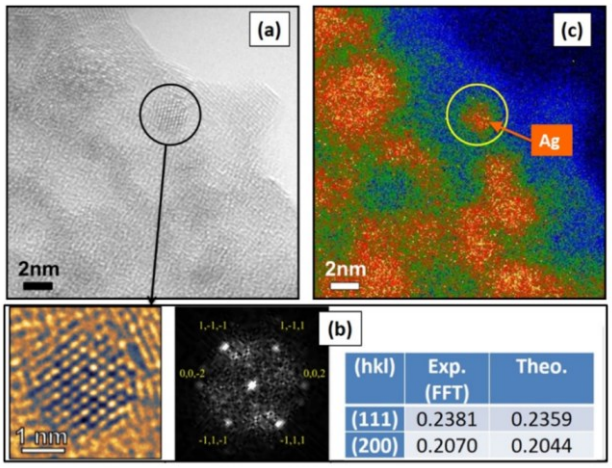

Figure 4.5: (a) HRTEM image of the implanted region, close to the free surface, showing the presence of crystalline Ag-NPs (see zoom); (b) associated FFT of the individual Ag-NP shown in the zoom. The NP is oriented following (110) zone axis and the measured interplane distances d_{hkl} fit well with the theoretical values (all in nm); (c) EFTEM image (filtering at the 467 eV edge of Ag) in the same region. Ag-rich regions are coloured in orange. From ref. [Cac15].

4.2.3 Optical response: plasmonic optical enhancement

The reflectance spectrum of a non-implanted zone of sample A is reported in Fig. 4.6a. The two minima around 500 nm and 350 nm correspond to anti-reflective conditions. As a matter of fact, the anti-reflective condition is given by the following equation:

$$2\left(n_{TiO_2}t_{TiO_2} + n_{SiO_2}t_{SiO_2}\right) = (m + 1/2)\lambda_m \qquad (4.4)$$

Using the thicknesses determined by TEM, one gets $\lambda_{1,\mathrm{A}} = 496$ nm with $n_{TiO_2,vis} \approx 2{,}7$ and $\lambda_{2,\mathrm{A}} = 371$ nm with $n_{TiO_2,UV} \approx 3{,}7$ for the destructive interference order $m = 1$ and 2, respectively, in good agreement with experiment shown in Fig. 4.6. One has to take in mind that the latter wavelength is located in the UV range where TiO_2 is strongly absorbing below its gap, *i.e.* 407 nm for rutile [Ben99].

To account more quantitatively of the optical response, we performed calculations of the reflectance. The theoretical spectra were obtained by describing the propagation of electromagnetic waves in the stratified medium using a matrix formulation [Car11][Bay14] and using the refractive and extinction indexes of amorphous SiO_2 and crystalline TiO_2 as input data. The best fit reported in Fig. 4.6a was obtained with $t_{TiO_2} = 89$ nm and $t_{SiO_2} = 84$ nm, in perfect agreement with TEM data. The experimental record of the reflectance is very well accounted for, in particular in the UV range (200 – 400 nm) where the absorption effect dominates.

The reflectance spectrum recorded from an implanted zone of sample A is reported in Fig. 4.6b. The presence of silver induces a spectral widening and blue shift (50 nm), and a reinforcing (up to 60 %) of the anti-reflective effect in the visible range. The LSPR should occur around 590 nm for Ag NPs embedded in a crystalline TiO_2 matrix (see Fig. 4.3), but its location is not obvious to determine from experimental data, because the resonance effect strongly interferes with the signature of electromagnetic confinement in the dielectric layer, as expected (Fig. 4.3).

The presence of silver also induces supplementary absorption corresponding to electronic interband transitions at wavelengths lower than the corresponding threshold near 320 nm (3.9 eV). This is brought out clearly in the differential reflectance spectrum (Fig. 4.6c) obtained by subtracting the experiment spectrum of a non-implanted zone from that of an implanted zone (Figs 4.6a and 4.6b, respectively). In Fig. 4.6c, besides the LSPR effect in the visible range, one also observes that the reflectance is reduced in the UV range (250-350 nm). This is a signature of intrinsic absorption by silver but also by defects generated in titania owing to the implantation process [Imp14].

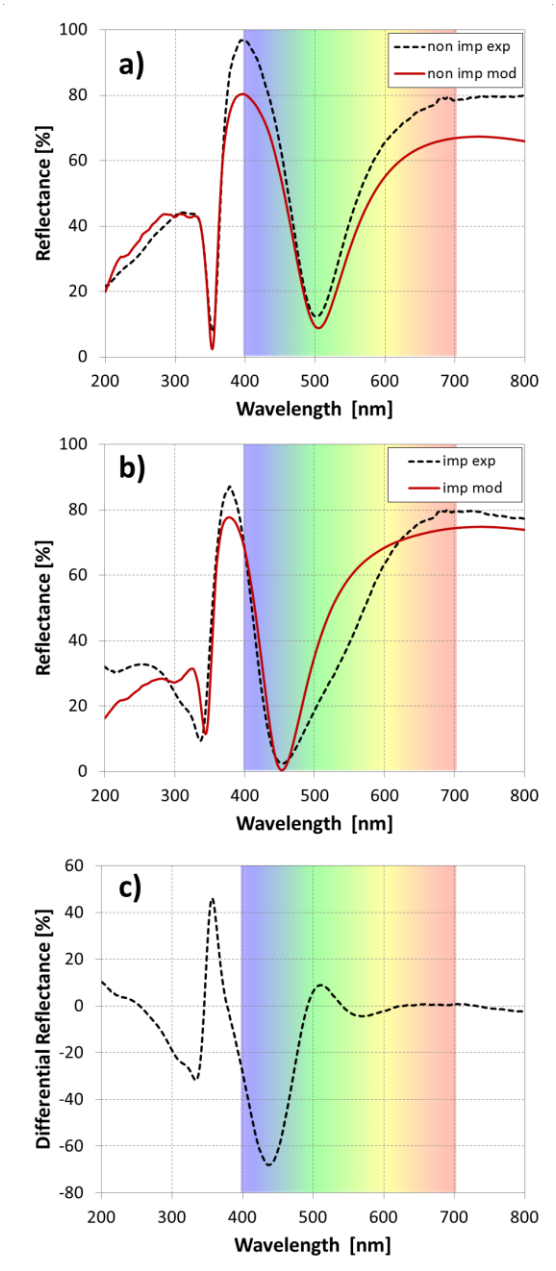

Figure 4.6: Reflectance of sample A (experiment in black dotted lines, theory in continuous red curves). a) non-implanted zone; b) implanted; c) differential reflectance. Adapted from [Cac15].

To account more precisely of these effects, simulations have been performed. The dielectric response of the composite layer with Ag NPs embedded in TiO_2 (TiO_2:Ag), has been described by using the quasi-static approximation of the classical Maxwell-Garnet theory (for more details, see [Car11][Bay14]). The energy relaxation of the plasmon occurs via generation of electron-hole excitations, and the corresponding energetic damping parameter is well known to be given by [Boh83]:

$$\Gamma = \hbar \frac{v_F}{L_{eff}} \tag{4.5}$$

where v_F is the Fermi velocity and L_{eff} the effective mean free path for electron collisions. In nm-sized NPs, surface collisions dominate and according to various models $0.43\,D < L_{eff} < 0.82\,D$ for a sphere of diameter D [Cor03]. Thus, the electronic confinement effect in the NPs with a mean size D is accounted for by introducing in the imaginary part of the metal dielectric function a plasmon damping term varying as D^{-1}. The best fit reported in Fig. 4.6b has been obtained by considering the following stacking: Si/SiO_2(84 nm)/c-TiO_2(68 nm)/a-TiO_2(10 nm)/a-TiO_2:Ag(10 nm) in agreement with TEM observations (Fig. 4.4). The theoretical curve corresponds to Ag NPs mean diameter $D = 3$ nm, in good agreement with TEM observations. The general trends of the experimental spectra are accounted for, namely the blue shift and deepening of the reflectance minima and the absorption enhancement in the UV mid-range. Nevertheless, some discrepancies are observed in the UV deep-range (below 300 nm) and in the visible mid-range. They are certainly due to the fact that disorder and defects into the TiO_2 matrix are not taken into account in our model. Indeed recent works on Fe^{2+} or C^+ implanted TiO_2 films [Imp14] have demonstrated an absorption enhancement in the UV range, and also new absorbing bands in the visible range because the implantation process generates energetically-deep levels into the gap of titania.

The main conclusion of this optical analysis is that embedded Ag NPs can considerably increase the absorption in a titania layer. When the size of these NPs remains in the nanometer range (< 5 nm), their

interaction with light is indeed dominated by absorption [Boh83] and the LSPR covers a wide spectral range in the visible. Moreover one can take simultaneously advantage of optical amplification because these Ag NPs are located in the vicinity of the free surface where the electric field is at maximum (under anti-reflective conditions) [Car11][Bay14]. More precisely, from data reported in Fig. 4.5c, one can estimate that a thin layer of 3 nm-sized Ag NPs into the composite layer leads to an average absorption increase of around 20% in the UV-VIS wavelength range.

4.2.4 Raman spectroscopy in Ag NPs and TiO_2

Raman spectroscopic measurements have been performed **in order** to analyze vibrational modes of the Ag NPs, TiO_2 matrix and Si substrate, but more particularly electron-hole excitations [Bay14]. Moreover, plasmon-resonant Raman spectroscopy has been used to get information on electron-phonon interactions in the Ag NPs and in TiO_2. A representative set of Raman spectra recorded on non-implanted zones and implanted zones of samples A and B, under plasmonic-optical resonance conditions (532 nm laser line) or out of resonance (638 nm laser line), are reported in Fig. 4.7. At first glance, one observes that the lowest signal is obtained with the 638 nm line whatever the zone or sample (similar records on sample B are not reported). This signal consists in the well-known first-order peak and acoustical or optical second-order Raman bands of the Si substrate (referred as 1O, 2A or 2O in Fig. 4.7, respectively). This signal will be used as a reference for evaluating absorption and resonance effects into the SiO_2/TiO_2:Ag multilayer film deposited on this substrate.

In Fig. 4.7, the Raman spectra recorded with the 532 nm laser line on non-implanted zones of samples A and B, show the appearance of two well-defined peaks located at 440 and 608 cm^{-1} characteristic of E_g and A_{1g} modes of a crystalline rutile phase of TiO_2 [Tra71]. These peaks are superimposed to a broad band with a cut-off around 700 cm^{-1} that can be attributed to an amorphous-like TiO_2 phase [War04]. Thus the Raman assignments comfort the TEM observation revealing a highly disordered polycrystalline film near the surface. One also notes that the signal of Si is

rather unchanged due to the transparency preservation of the deposited dielectric film. The most striking point is the fact that the TiO_2 signal drops by about 2 from sample A to B whereas the thickness of TiO_2 is almost doubled (from 85 to 165 nm). This is well accounted for by the optical confinement effect in the dielectric film: only in sample A, the exciting wavelength (532 nm) rather well fulfils the anti-reflectivity condition ($\lambda_{1A} \approx 500$ nm, Fig. 4.6a). The electromagnetic energy is thus essentially confined in the TiO_2 layer because of its high refractive index value and position near the free surface. In sample B, the optical amplification is very low because the photon wavelength is far from the antireflective condition ($\lambda_{1B} \approx 760$ nm).

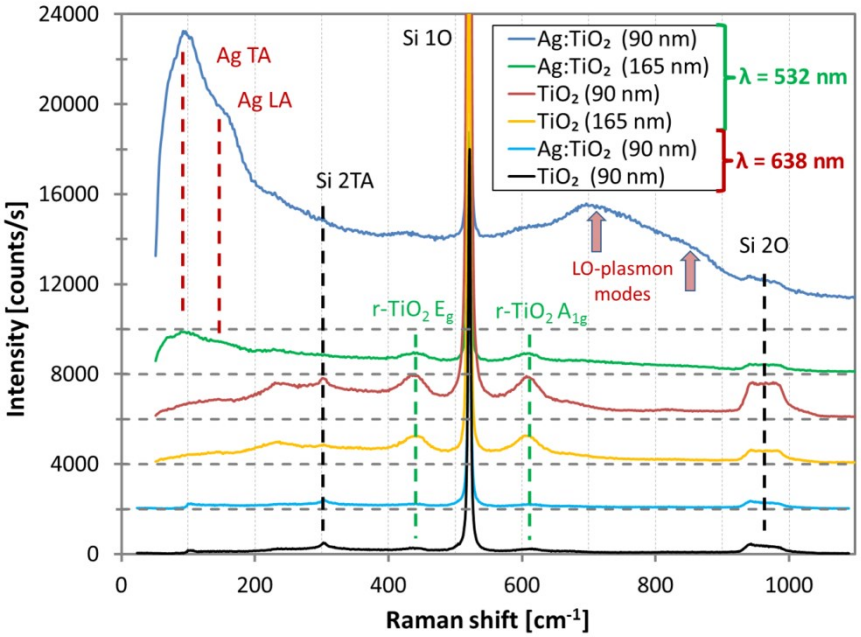

Figure 4.7: Raman spectra recorded on non-implanted zones and implanted zones of samples A and B under plasmon-resonant excitation (532 nm) or out of resonance (638 nm). The laser power was the same for all the spectra and limited to ~ 1 mW to avoid any heating of the samples. From ref. [Cac15].

This Raman analysis shows how engineering the optical properties of a photocatalytic film can be useful to increase the photon capture in a given spectral range.

The Raman spectra recorded with the 532 nm line on implanted zones of samples A and B are displayed in Fig. 4.7. The spectra are very similar taking into account the optical amplification effect: here the gain is 3.4. The incorporation of Ag in TiO_2 (which is exactly the same in both samples) considerably affects the Raman signal in three main points. First, the signal of the Si substrate is reduced testifying the absorption increase into the metal-dielectric composite film. Second, the peaks characteristic of crystalline rutile have weakened and widened because of disorder-induced effects of the matrix (amorphous-like layer in Fig. 4.4). Third, new and intense bands appear at low (below 200 cm^{-1}) and at high frequencies (between 650 and 900 cm^{-1}). At low frequency they are attributed to Ag vibrational modes, and at high frequency to TiO_2 vibrational modes, respectively. They are superimposed on a continuous background spanning a very large frequency range well beyond the vibrational response cut-off of the composite film near 1000 cm^{-1}.

All these observations are characteristic of a plasmonic-resonant effect, in which the Raman scattering by vibrations is considerably enhanced if the corresponding bonds are located in the vicinity of metallic particles supporting a LSPR. Moreover, such a SERS signal is systematically accompanied by the so-called “background” which origin is generally largely ignored and arbitrary subtracted. However, when photoluminescence processes can be discarded, this background is now recognized as originating in inelastic scattering by electron-hole excitations [Mon87] [Ake94][Por01][Bay14][Car15]. In fact it can be used as a sensitive probe to directly inform on the presence of free carriers. Single-particle excitations consist in intraband transitions for electrons in the vicinity of the Fermi level to the continuum of free states above this level: their spectrum begins at zero frequency and displays a monotonous shape that culminates at a frequency directly linked to the characteristic scale of the electronic confinement [Mon87][Bay14]. For confinement at the nanoscale, the spectral energetic range of electronic excitations coincides with that of many molecular vibrations, ensuring easy tuning for efficient coupling. In

sample A, the background ends at a frequency near 2000 cm^{-1} in good agreement with previous observations in nm-sized Ag NPs [Bay14]. Thus any vibrational mode with a lower frequency may couple with the continuum of electron-hole excitations of the Ag NPs and thus display a SERS enhancement. Two types of modes are indeed implied, the "bulk" phonons of the Ag NPs themselves and the TiO_2 phonons of the matrix in the vicinity of these Ag NPs. It has been recently shown [Bay14][Bay14b] that Raman scattering by bulk phonons of Ag and Au nanocrystals can be activated due to the lack of translational invariance during the light-matter interaction. The signal mimics rather well the vibrational density of states (VDOS) of crystalline nanocrystals and is a powerful tool for structure determination of metal nanoparticles with few nanometers in size [Sau15]. In Fig. 4.7, one clearly observes two Van Hove singularities of this VDOS corresponding to transverse and longitudinal acoustical modes (TA and LA respectively) at high symmetry points of the Brillouin zone in bulk silver [Bay14]. The strong decrease upon frequency shift is simply due to the Bose population factor effect. The very high intensity of this Raman signal is directly linked to the plasmon-resonant SERS and the high quality factor of the LSPR in titania; it is unobservable out of resonant condition, as shown in Fig. 4.7.

4.2.5 LO-phonon-plasmon modes in TiO_2

In Fig. 4.7 we attribute the structures emerging from the background between 650 and 900 cm^{-1} to enhanced Raman scattering by coupled "LO-phonon-plasmon modes" of TiO_2. This signal is absent out of resonance and without Ag NPs. The coupling of electronic excitations with the longitudinal optical (LO) polar phonons has been widely studied in *n*- or *p*-doped semiconductors [Moo66][Mla91] and high-Tc superconductors [Rez93]. These modes have been also observed with IR reflectance spectroscopy in non-stoichiometric rutile [Bau77] and anatase [Gon97] [Gru06]. LO- and surface optic (SO-) plasmon modes have also been invoked as sensitive to water absorption at the surface of photocatalytic TiO_2 particle films [War04]. In rutile, the four polar LO modes (1 A_{2u} + 3 E_u) are

not Raman active due to their odd symmetry [Tra71]. However these modes can strongly interact with free carriers present in the dielectric matrix. The resulting "LO-phonon-plasmon" modes lead to Raman scattering related to mechanisms (electro-optic or Fröhlich) normally forbidden out of resonance. The presence of disorder may favor these mechanisms owing to breakdown of the wave-vector selection rule.

In IR spectra, similar modes have been accounted for theoretically [Gon97] [Gru06] by using a dielectric function $\varepsilon(\omega)$ containing two terms, a first one relative to optical phonons and the second to free carriers. One can write this dielectric function, according to notations used in ref. [Mla91] and [Gro98], as follows:

$$\varepsilon(\omega) = \varepsilon_\infty \left(1 + \sum\nolimits_{j=1}^{4} \frac{\omega_{p,j}^2}{\omega_{T,j}^2 - \omega^2 + i\gamma_j\omega} + \frac{\omega_p^2}{-\omega^2 + i\gamma_p\omega}\right) \qquad (4.6)$$

where ε_∞ is the high frequency dielectric constant, $\varepsilon_\infty = n_{vis}^2 \approx 8$ for rutile. For each *j*-th oscillator of TiO_2, the ionic plasmon frequency $\omega_{p,j}$ is defined from the corresponding LO and TO frequencies, $\omega_{L,j}$ and $\omega_{T,j}$:

$$\omega_{p,j}^2 = \omega_{L,j}^2 - \omega_{T,j}^2 \qquad (4.7)$$

The damping of each oscillator is taken into account through the parameters γ_j and γ_p. The presence of charge carriers is described by the last (Drude-like) term in Eq. (4.6) in which ω_p is the plasmon frequency. Obviously $\omega_T = 0$ for free carriers. It should be made clear here that this "plasmon" component invoked in the so-called "LO-phonon-plasmon modes" refers to carriers injected in the TiO_2 matrix and not to the free electron gas of the metallic NPs. For TiO_2 polar modes, large TO-LO splittings have to be considered due to the ionic character of the bonds. At high doping level, the coupling with the resulting over damped electronic oscillation is expected to get broad Raman features in the optical-phonon frequency range [Mla91][Koz94]. The frequencies of LO polar modes in rutile have been estimated at 366, 445, 830 cm^{-1} (E_{u2} modes) and 796 cm^{-1} (A_{2u}) [Sch13] and thus one expect LO-phonon-plasmon modes in this

frequency range, as already observed experimentally in IR spectra [Gon97][Gru06]. Of particular relevance is the fact that Warren et al. [War04] have observed the appearance of three modes at 685, 745 and 828 cm^{-1} in IR spectra of TiO_2 photocatalytic particle films. The absorption spectrum is deduced from the imaginary part of the dielectric function, $Im\{\varepsilon(\omega)\}$ whereas the Raman spectrum is linked to $Im\{-\varepsilon^{-1}(\omega)\}$. However, in both spectra the frequencies of the LO-phonon-plasmon modes are expected near the poles of $\varepsilon(\omega)$ (Eq. (4.6)). Indeed, an intense and broad Raman band is observed in Fig. 5 near 700 cm^{-1} with a shoulder near 820 cm^{-1}. When several polar modes are simultaneously present in a given material, it has been shown that the higher the frequency is, the stronger the ionic plasmon coupling is [Gro98][Har11]. In TiO_2, one thus expect that the LO-plasmon coupling will mainly concern the highest frequency and intense E_{u2} mode which TO-LO splitting is 500-830 cm^{-1} [Sch13].

The presence of broad Raman bands in disordered TiO_2 materials has been observed but attributed to an amorphous-like phase [Har11]. Here we have discarded such interpretation because the Raman bands lie at higher frequencies than in amorphous titania. Moreover we found a very low scattering efficiency within the same experimental conditions. Moreover the Raman lineshape in figure 4.7 does not reflect the rutile VDOS expected from lattice dynamics simulations [Sik05][Sch13]: only the highest frequency and polar modes are selectively activated. In particular, one notes in Fig. 4.7 that the E_g and A_g modes are not at all affected by this SERS effect.

Of importance is to note that the enhancement of the polar modes gets a proof of the presence of free carriers into the TiO_2 matrix in the vicinity of Ag NPs. This should offer a very interesting opportunity to analyze *in-situ* electron transfer from metallic NPs to a polar semiconductor which is known as the crucial step for plasmon-assisted photocatalytic processes.

4.2.6 Electron-phonon confinement in Ag NPs

Finally, we have used plasmon-enhanced Raman scattering to get information on the Ag NPs sizes, in a nondestructive way. Very low frequency Raman (or Brillouin) spectra have been recorded in plasmon resonant conditions using the 530 nm laser line of a Krypton laser and a specific spectrometric set-up developed at CEMES-CNRS [Bay14] (Fig. 4.8).

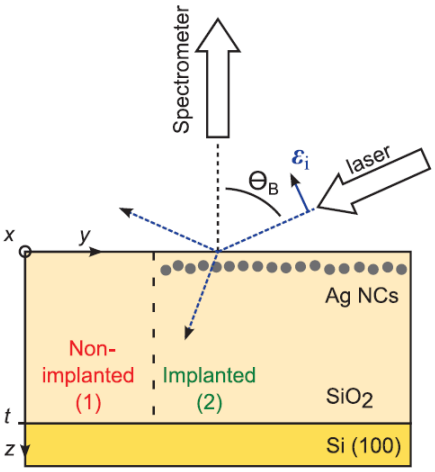

Fig. 4.8: Schematic view of the experimental setup. A specific double objective geometry is used at the entrance of the spectrometer. The p-polarized laser light is focused under the Brewster incidence. From ref. [Bay14].

Both Stokes and anti-Stokes parts of the spectra recorded on implanted and non-implanted zones of sample A are reported in Fig. 4.9. On silver-free TiO_2 layer, one only observes the Brillouin peak of the Si substrate, whereas on TiO_2 doped with Ag NPs, a very intense Raman band is observed. We interpret this band as due to Lamb modes of the Ag NPs which are strongly enhanced in plasmon-resonant conditions. The intensity of the electron-phonon coupling is at maximum for these vibrational modes because they imply the NP as an ensemble: they are thus spatially coherent with the plasmon mode [Bay14].

These collective oscillations have been already widely studied, either experimentally or theoretically, in Ag or Au NPs embedded in various matrices (Al_2O_3 or SiO_2) [Pal99][Bay14]. It has been shown that only even modes are Raman active, and that the spectrum is dominated by the fundamental ($n = 1$) quadrupolar ($\ell = 2$) mode. The unusual huge signal observed here in TiO_2 (for the first time to our knowledge) demonstrates once more the high quality factor of LSPR for Ag NPs embedded in a high index matrix.

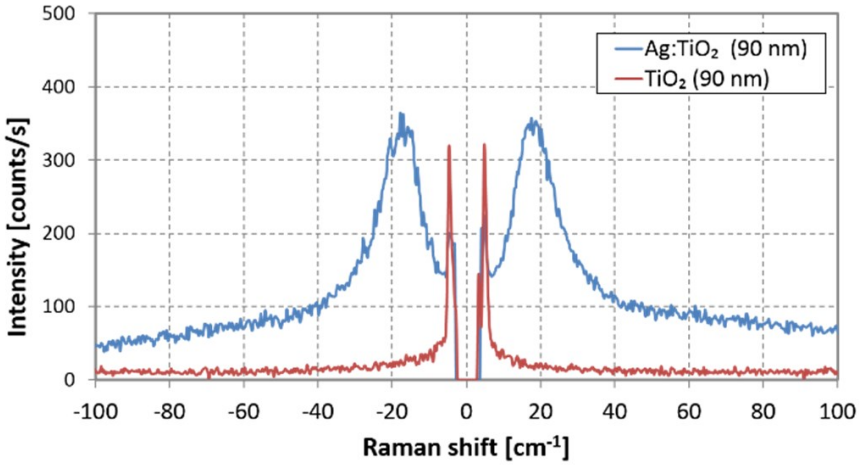

Figure 4.9: Raman-Brillouin scattering (Stokes and anti-Stokes parts) of an implanted zone of sample A. From ref. [Cac15].

To get a more precise information from this low-frequency Raman signal, it has been corrected from the set-up response, Bose statistics factor and electron-hole contribution using a procedure already reported [Bay14]. The resulting corrected spectrum is reported in Fig. 4.10 where the signal has been decomposed in 4 components. A fitting procedure has been performed using Gaussians in order to take into account the inhomogeneous broadening due to statistical size distribution of the Ag NPs. The lowest frequency components, at 17 ± 2, 26 ± 4 and 42 ± 8 cm^{-1}, are attributed to the lowest harmonics ($n = 1,\ 2$ and 3, respectively) of the quadrupolar Lamb mode ($\ell = 2$) [Bay14]. The higher mode (around 70

cm^{-1}) is the contribution of the TA band of the silver VDOS, as shown in Fig. 4.7. The frequencies of these quasi-confined collective modes vary as D^{-1}:

$$\omega_{n,\ell} = A_{n,\ell} \frac{v_T}{D} \tag{4.8}$$

where v_T is the transverse sound velocity and $A_{n,\ell}$ a numerical coefficient depending on the degree of confinement. For the fundamental quadrupolar mode and using previous calculations [Pal99], one gets $\omega_{1,2}\left(\text{cm}^{-1}\right) = 47/D(\text{nm})$. That leads to an average size of the Ag NPs $D = 2.8 \pm 0.3$ nm, in good agreement with TEM observations (See Fig. 4.5) and reflectance simulations.

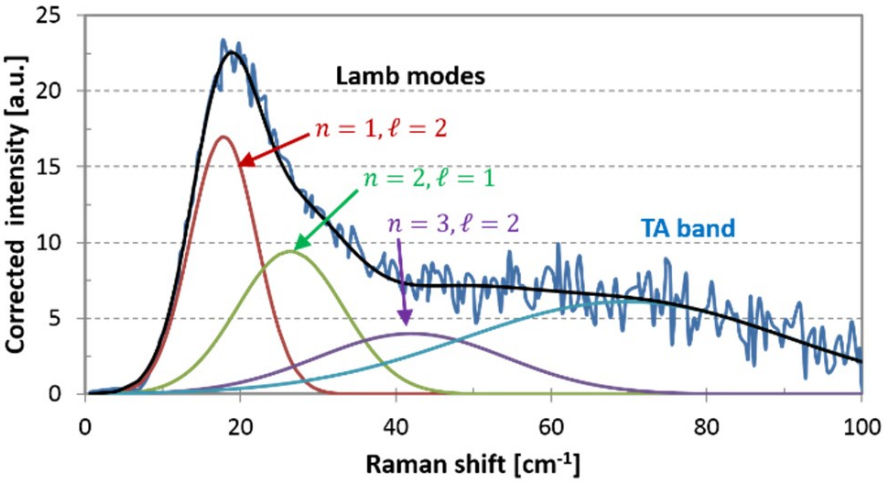

Figure 4.10: Deconvolution of the corrected Stokes Raman spectrum into the different Lamb modes. From ref. [Cac15].

Low-frequency Raman spectroscopy can thus be used as a non-destructive probe to analyze metallic particles, whose size and location are crucial parameters to define spectrally and spatially the LSPR.

4.2.7 Electron-hole generation and transfer: photocatalytic activity

From discoloration tests of MB solutions, the photocatalytic activity of implanted samples has been compared with that of non-implanted ones.

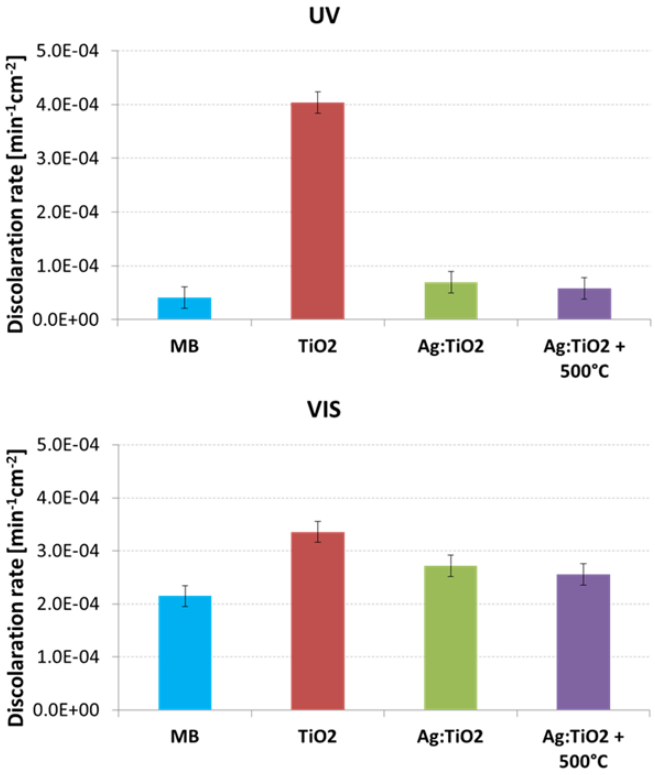

Figure 4.11: Discoloration rate of the TiO_2 and $Ag:TiO_2$ samples under UV or visible illumination. The rates have been normalized to the macroscopic area of each sample.

The results in Fig. 4.11 do not show an activity enhancement induced by the implantation process and the presence of Ag NPs. On the contrary, a strong reduction (~80 %) is observed under UV illumination, probably due to charge carrier recombination on defects generated by the implantation

process: the superficial and active layer became a highly disordered TiO_2 phase, as revealed by TEM (Fig. 4.4) and optical absorption analysis (Fig. 4.6b). The ion bombardment affects the free surface and thus may alter the MB molecule adsorption efficiency. However the photocatalytic activity under visible illumination is less reduced (~ 20%). One may argue that disorder effect (traps and surface alteration) is partly compensated in this optical range by Ag NPs plasmonic enhancement effect. Moreover, we observe neither recovery nor enhancement of the photocatalytic activity after annealing of the implanted samples.

4.3 Conclusions

In this section we have shown how a specific optical engineering of composite substrates containing Ag NPs embedded in a thin TiO_2 layer may be fruitful for plasmon-enhanced photocatalytic applications. For that purpose, we have simultaneously taken benefit of the (i) very high quality factor of the corresponding localized surface plasmon polariton resonance that guaranties the best electromagnetic field enhancement, (ii) downshift versus the middle range of the visible spectrum of this resonance.
Using low-energy ion beam synthesis, Ag NPs have been formed, in a single step procedure, at few nanometers from the free surface, *i.e.* in the region where all the photocatalytic processes take place.

Moreover, the plasmonic effect is amplified using an antireflective multilayer. This allows to (i) increase the photon capture in a desired spectral range and (ii) enhance this capture in a very thin layer near the surface.

Using simultaneously small Ag NPs (few nanometers in size) in doped titania and the lowest optical interference order in controlled stacking architectures can considerably improve photocatalytic performance under visible light irradiation. These composite substrates which design is optimized so as to maximize the electromagnetic energy and carriers generation also appear promising for sensitive SERS probes or other plasmo-electronics based devices.

Unfortunately, however, the synthesis technique seems to damage irremediably the upper layer of the hosting TiO_2 matrix. Therefore, the logically consequent step should be to use a properly optically engineered substrate with embedded metal nanoparticle through a technique that preserves the photoactive material. This will be the content of next section.

4.4 References

[Ake94] W. Akemann, A. Otto, Surface science, **307–309 B**, 1071–1075 (1994).
[Bau77] J. F. Baumard, F. Gervais, Phys. Rev. B, **15**, 2316 (1977).
[Bay14] M. Bayle, P. Benzo, N. Combe, C. Gatel, C. Bonafos, G. Benassayag, R. Carles, Phys. Rev. B, **89**, 195402 (2014).
[Bay14b] M. Bayle, N. Combe, N. M. Sangeetha, G. Viau, R. Carles, Nanoscale **6**, 9157-9165 (2014).
[Ben13] P. Benzo, C. Bonafos, M. Bayle, R. Carles, L. Cattaneo, C. Farcau, G. Benassayag, B. Pécassou, D. Muller, J. Appl. Phys., **113**, 193505 (2013).
[Ben99] A. Bendavid, P. J. Martin, Å. Jamting, H. Takikawa, Thin Solid Films **355–356**, 6–11 (1999).
[Bie80] J. P. Biersack, L. G. Haggmark, Nucl. Instr. Methods, **174**, 257 (1980).
[Boh83] C. F. Bohren; D. R. Huffman, *Absorption of Light by Small Particles*, Wiley: New York, 1983.
[Cac15] G. Cacciato, M. Bayle, A. Pugliara, C. Bonafos, M. Zimbone, V. Privitera, M. G. Grimaldi, R. Carles, Nanoscale, **7**, 13468-13476 (2015).
[Car09] R. Carles, C. Farcau, C. Bonafos, G. Benassayag, B. Pécassou, A. Zwick, Nanotechnology, **20**, 355305 (2009).
[Car11] R. Carles, C. Farcau, C. Bonafos, G. Benassayag, M. Bayle, P. Benzo, J. Groenen, A. Zwick, ACS Nano, **5**,8774–8782 (2011).
[Car15] R. Carles, M. Bayle, P. Benzo, G. Cacciato, V. Privitera, G. Benassayag, C. Bonafos, Phys. Rev. B, **92**, 174302 (2015).
[Cor03] E. A. Coronado, G.C. Schatz, J. Chem. Phys., **119**, 3926 (2003).
[Far10] C. Farcau, C. Bonafos, P. Benzo, G. Benassayag, R. Carles, J. Appl. Phys., **108**, 093516 (2010).
[Gon97] R. J. Gonzalez, R. Zallen, H. Berger, Phys. Rev. B, **55**, 7014 (1997).

[Gro98] J. Groenen, R. Carles, G. Landa, C. Guerret-Piécourt, C. Fontaine, M. Gendry, Phys. Rev. B, **58**, 1045 (1998).
[Gru06] M. Grujić-Brojčin, M. Šćepanović, Z. Dohčević-Mitrović, Z. V. Popović, Science of Sintering, **38**, 183 (2006).
[Har11] F. D. Hardcastle, H. Ishihara, R. Sharma, A. S. Biris, J. Mat. Chem., **21**, 6337 (2011).
[Hou13] W. Hou, S. B. Cronin, Adv. Funct. Mater., **23**,1612–1619 (2013).
[Kel03] K. L. Kelly, E. Coronado, L. L. Zhao, G. C. Schatz, J. Phys. Chem. B, **107**, 668-677 (2003).
[Koz94] T. Kozawa, T. Kachi, H. Kano, Y. Taga, M. Hashimoto, N. Koide, K. Manabe, J. Appl. Phys., **75**, 1098 (1994).
[Imp14] G. Impellizzeri, V. Scuderi, L. Romano, P. M. Sberna, E. Arcadipane, R. Sanz, M. Scuderi, G. Nicotra, M. Bayle, R. Carles, F. Simone, V. Privitera, J. Appl. Phys., **116**, 173507 (2014).
[Lin11] S. Linic, P. Christopher, D. B. Ingram, Nature Materials, **10**, 911–921 (2011).
[Liu14] E. Liu, L. Kang, Y. Yang, T. Sun, X. Hu, C. Zhu, H. Liu, Q. Wang, X. Li, J. Fan, Nanotechnology, **25**, 165401 (2014).
[Mel01] A. Meldrum, R. F. Haglund, L. A. Boatner, C. Woody White, Adv. Mater., **13** (19), 1431 (2001).
[Mil12] A. Mills, C. Hill, P. K. J. Robertson, Journal of Photochemistry and Potobiology A: Chemistry, **237**, 7-23 (2012).
[Mla91] A. Mlayah, R. Carles, G. Landa, E. Bedel, A. Muñoz-Yagüe, J. Appl. Phys., **69**, 4064-4070 (1991).
[Mon87] R. Monreal, F. Flores, Y. Gao, T. López-Ríos, Europhys. Lett., **4**, 115 (1987).
[Moo66] A. Mooradian, G. B. Wright, Phys. Rev. Lett., **16**, 999 (1966).
[Pal99] B. Palpant, H. Portales, L. Saviot, J. Lerme, B. Prevel, M. Pellarin, E. Duval, A. Perez,M. Broyer, Phys. Rev. B, **60**, 17107-17111 (1999).
[Por01] H. Portales, E. Duval, L. Saviot, M. Fujii, M. Sumitomo, S. Hayashi, Phys. Rev. B, **63**, 233402 (2001).
[Rez93] D. Reznik, S. L. Cooper, M. V. Klein, W. C. Lee, D. M. Ginsberg, A. A. Maksimov, A. V. Puchkov, I. I. Tartakovskii, S-W. Cheong, Phys. Rev. B, **48**, 7624 (1993).

[Sau15] H.E. Sauceda, I.L. Garzón, J. Phys. Chem. C, **119 (20)**, 10876–10880 (2015).
[Sch13] S. Schöche, T. Hofmann, R. Korlacki, T. E. Tiwald, M. Schubert, J. Appl. Phys., **113**, 164102 (2013).
[Sik05] R. Sikora, J. Phys. Chem. Sol., **66**, 1069-1073 (2005).
[Tra71] J. G. Traylor, H. G. Smith, R. M. Nicklow, M. K. Wilkinson, Phys. Rev. B, **3**, 3457 (1971).
[War04] D. S. Warren, A. J. McQuillan, J. Phys. Chem. B, **108**, 19373-19379 (2004).

Chapter 5 TiO_2/Ag/TiO_2 nanocomposite film obtained via sequential sputtering

In the previous two sections, we demonstrated how the presence of metal nanoparticles can enhance the optical absorption of a nanocomposite metal-TiO_2 thin film, especially with proper film thickness engineering. However, despite the correct optical tuning, we observed two main deficiencies: one is related to the maximization of the area of the photocatalytic substrate (TiO_2) exposed to water; the second one is related to the preservation against damage of the first few nm of the surface.

In this section, we finally reached the goal of having a TiO_2/AgNPs/TiO_2 nanocomposite film showing photocatalytic activity under visible illumination.

5.1 Optical engineering of TiO_2/Ag/TiO_2 nanocomposite films for visible driven photocatalysis

The exposure of a photocatalytically active surface has been demonstrated, through the previous two chapters, of primary importance for the goal of efficient substrates for water purification. At the same time, the optical engineering of the substrate can highly improve the response of the nanocomposite in the visible range. Therefore, the logical step towards solar-driven photocatalysis is to fabricate a TiO_2/AgNPs/TiO_2 multilayer using a technique that allows fine tuning of several parameters (particle size and position, thickness of each layer) while preserving the quality of the photoactive surface. For these reasons, we proposed sequential sputtering and annealing as methodology to elaborate a TiO_2/Ag/TiO_2 nanocomposite film. In Fig. 5.1 is shown a schematic representation of the steps followed to realize of the nanocomposite film: (a) deposition of the TiO_2 “matrix” layer (realized for the antireflective propose), (b) deposition of the Ag film, (c) thermal annealing in order to realize the silver

nanoparticles through dewetting and (d) deposition of the TiO_2 protective layer.

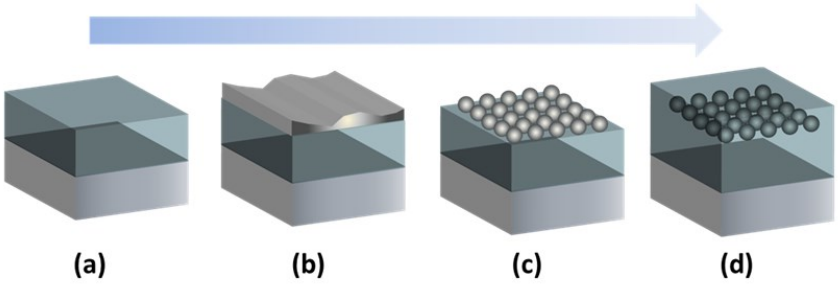

Figure 5.1: From left to right, schematic representation of the elaboration process: (a) TiO_2 substrate deposition, (b) Ag deposition and (c) nanostructuration via thermal annealing, and (d) deposition of a TiO_2 capping layer.

5.1.1 Optical engineering

As widely discussed in the previous chapter, in order to obtain an enhanced optical response of the nanocomposite film, we must tune the film thickness in order to match the antireflectivity conditions in correspondence to the plasmon resonance wavelength. The plasmon resonance wavelength depends on the size and shape of metal nanoparticles and on the refractive index of the surrounding medium. So we performed several simulations in order to have more insight into the position of the plasmon resonance of a Ag NP embedded in a TiO_2 matrix [Kel03][Mai07] [Nog07]. Firstly, we performed simulations of the extinction spectra of a silver (refractive index from [Joh72]) nanosphere embedded in TiO_2 (rutile, refractive index from [Lan12]) using SCATMECH library by T. A. Germer [Ger15]. There is a clear limitation in this approach since it is supposed that nanoparticles are immersed in a isotropic medium (not close to the surface) and that they are far apart so to neglect mutual interactions. Nevertheless, it has been proved to be a quite good qualitative approximation of our experimental case. In Fig. 5.2 are shown the results

for three different diameters (20 nm, 40 nm, and 60 nm). According to the simulations, the wavelength range of interest for the plasmon resonance of Ag nanoparticles in TiO_2 matrix lies between 550 nm and 750 nm. It is worth noting that the position of the plasmon resonance is red-shifted respect to the case of nanoparticles of the same size but embedded in air, for which the resonance appears approximately in the range of 400-500 nm. In the simulated spectra we observe that, as expected, the resonance peak redshifts and broadens as the diameter size increases. We also observe the appearance of the quadrupolar mode at lower wavelengths for bigger diameters [Boh83].

The thickness of the oxide layer necessary to match the antireflectivity condition was calculated using Eq. 4.3, already discussed in the previous chapter:

$$d = \frac{(2m+1)\lambda_n}{4} \qquad (4.3)$$

where *m* (integer) is the order of reflection and λ_n is the wavelength in the medium of refractive index *n*. Assuming $m = 1$ and $n_{TiO_2} \approx 2.7$ (in the visible spectral range), we obtain a matrix thickness between 167 nm and 191 nm. By using this information, we have to realize a sample having a final thickness (including the 10 nm capping layer) of about 190 nm. Experimentally, we prepared a 180 nm TiO_2 "matrix" layer on silicon; then we deposited a 5 nm Ag film and performed thermal annealing (400 °C, 1 h, in vacuum) in order to induce the dewetting-driven nanostructuration; finally we deposited a 10 nm TiO_2 "capping" layer.

Moreover, a TiO_2/Ag/TiO_2 nanocomposite sample whose oxide thickness was out of the antireflectivity conditions (150 nm) was grown, in order to demonstrate the role of the optical amplification.

The details of the experimental procedure followed in order to realize both the samples will be presented in the next two paragraphs.

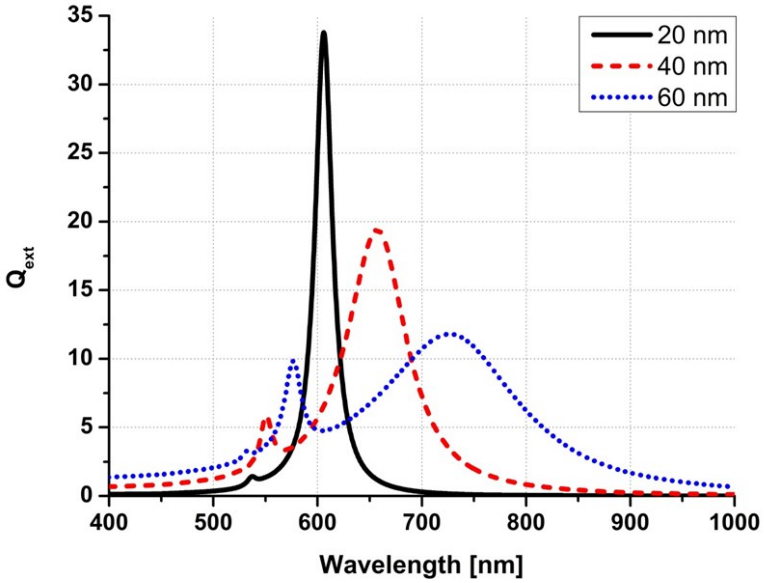

Figure 5.2: Extinction coefficient versus wavelength for a Ag sphere embedded in TiO_2 (rutile) varying the diameter: 20 nm (black continuous line), 40 nm (red dashed line) and 60 nm (blue dotted line).

5.1.2 Materials and methods

A Ti (99.999% purity target) film was grown by sputtering (using a Dual Sputter Quorum Q350T D system, at 100 mA at base pressure of 1.0e-02 mbar, using Ar as sputtering gas) on Si <100> substrates. Polycrystalline TiO_2 was obtained, starting from these substrates, by thermal oxidation at 600°C, 30 min in 2.5 lpm of O_2 flow using a standard Carbolite horizontal furnace.

Ag (99.999% purity target) depositions on the polycrystalline TiO_2 were carried out using a Emitech K550x Sputter coater apparatus. The thickness of the Ag layer after 150 s of deposition, at an emission current of 10 mA, a nominal thickness (checked by RBS) of d = 5 nm of Ag was

deposited. After Ag depositions, samples were annealed in vacuum (pressure $6 \cdot 10^{-3}$ mbar), at 400°C for 60 min.

The final 10 nm TiO_2 capping layer has been obtained via deposition of a thin Ti film (Dual Sputter Quorum Q350T D system, at 50 mA), followed by a thermal annealing at 400 °C for 30 min in vacuum. Due to the low deposition rate, the deposited layer is already oxidized, so that the thermal annealing was required just to ensure the crystallinity of the capping layer. Anyway, this step has not influenced the underlying Ag nanostructured film. The thickness of 10 nm for the capping layer was chosen according to the maximum diffusion length of carriers in TiO_2, as recently reported by Luttrell *et al.* [Lut14].

Crystal structure was determined by X-ray diffraction (XRD, Bruker D-9000, Cu Kα, 40 kV, 40 mA, at 0.01° s^{-1}) and Bruker diffraction suite software was used for the diffraction analysis.

The stoichiometry and the thickness of the films were checked by Rutherford Backscattering Spectrometry (RBS), using a 2 MeV He^+ beam with a scattering angle of 165°.

SEM analyses were performed with a Zeiss FEG-SEM Supra 25 Microscope operating at 5 kV at a working distance of 4 mm. SEM images were analyzed by Gatan Digital Micrograph software.

AFM analyses were performed with a Veeco-Innova microscope operating in high amplitude mode, and ultra-sharpened Si tips were used (MSNL-10 from BRUKER). AFM images were analyzed by Gwyddion software.

Optical properties were measured in the wavelength range of 200-1000 nm using a Perkin-Elmer UV-Vis Lambda 40 spectrophotometer.

For the photocatalytic activity tests we referred to the guidelines of the ISO 10678:2010 [Mills, 2012]. According to the standard, 10 µl of methylene blue (MB) solution (0.05 wt.%) were added to each 1 ml volume of deionized Milli-Q water (resistivity 18 MΩ·cm). The MB concentrations were measured according to the Lambert-Beer law at 664 nm (extinction coefficient 7.4×10^4 M^{-1} cm^{-1}). During the tests, each sample was placed at the bottom of a cylindrical vessel having a base area of 2 cm^2 filled with 2 ml of the MB-water solution. The solutions were left for one hour in dark to allow the adsorption of MB onto films and vessels surfaces and then

illuminated with visible light (Osram DULUX S BL 9 W/71 lamp). During light irradiation the vessels were covered with quartz in order to avoid evaporation during irradiation. The wavelength of the visible light source was centered at 453 nm (FWHM 40 nm) and irradiance was 1.5 mW/cm^2. A UV filter was used in order to cut the wavelengths below 420 nm.

5.1.3 Structural characterization

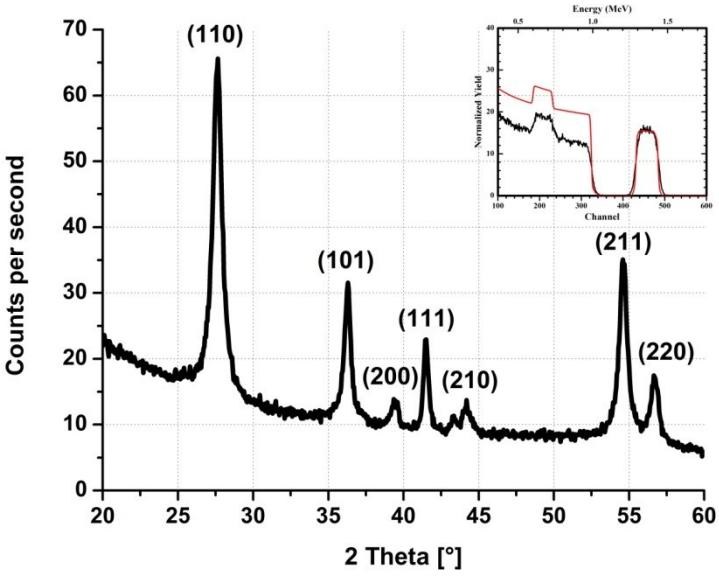

Figure 5.3: XRD spectra of the TiO_2 substrate showing the main peak of rutile phase. In the inset, RBS spectra of the same sample (black) with RUMP simulation (red).

The phase formed after the 600°C annealing in O_2 was checked via XRD. In Fig. 5.3 we report the resulting spectrum. Only the peaks of rutile phase have been detected. In the inset the RBS spectrum of the same sample is reported. The spectrum simulation performed with RUMP, reported by the red line, confirmed that the stoichiometry was that of TiO_2 ($[O]/[Ti] = 2.0 \pm 0.1$) and resulted in a thickness of 172 ± 8 nm and of

156 ± 8 nm (using the density of rutile 4.25 gcm^{-3}[Han11]) for the two samples in or out the antireflectivity conditions. Note that the discrepancy of the simulation with respect to the experimental data is limited to the region concerning the Si signal. This is simply due to a channeling effect that causes a reduction of the yield of the signal.

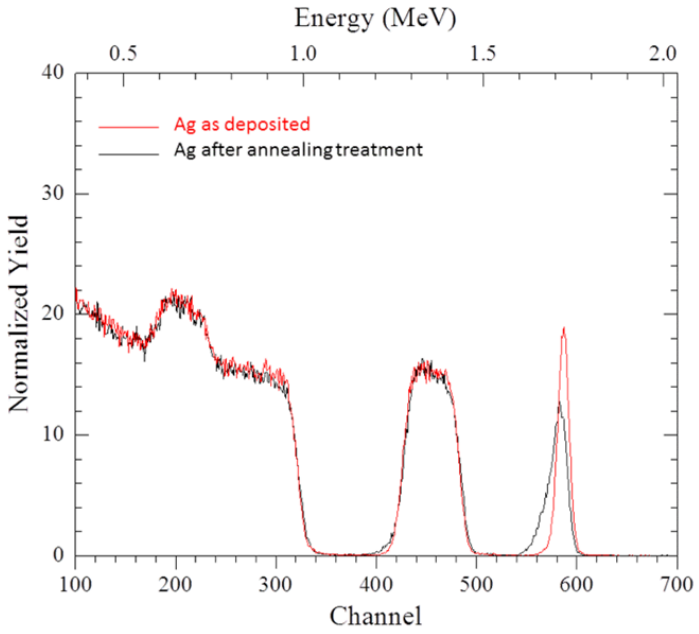

Figure 5.4: RBS spectra of the Ag/TiO_2 sample as-deposited (black) and after annealing treatment at 400 °C (red).

In Fig. 5.4 the RBS spectra of the Ag/TiO_2 samples before and after the annealing treatment are reported. The integral of the Ag signal (between channels 540 and 610) indicates that the thickness of the as deposited Ag layer is $4.01 \cdot 10^{16}$ atoms/cm^2, corresponding to about 5 nm if we assume a uniform layer having the bulk Ag density ($5.85 \cdot 10^{22}$ atoms/cm^3). The area of the Ag peak does not change after the annealing, indicating that there is no Ag loss. However, the Ag peak after annealing is broadened and the change in the shape is the signature of the

nanostructuration of the metal film. Indeed, in the latter case the beam sees a high surface roughness and the Ag nanoparticles have a diameter that is greater than the original Ag film thickness. This means that part of the beam undergoes to higher energy loss, translating in a higher number of counts at lower energy range with respect to that of Ag.

The morphology of the sample at different stage of the preparation was observed via AFM and SEM. The images of (a) the TiO_2 substrate, (b) the Ag as deposited film, (c) the Ag/TiO_2 after annealing and, finally, (d) the TiO_2 capping layer are shown in Fig. 5.5 (AFM) and Fig. 5.6 (SEM).

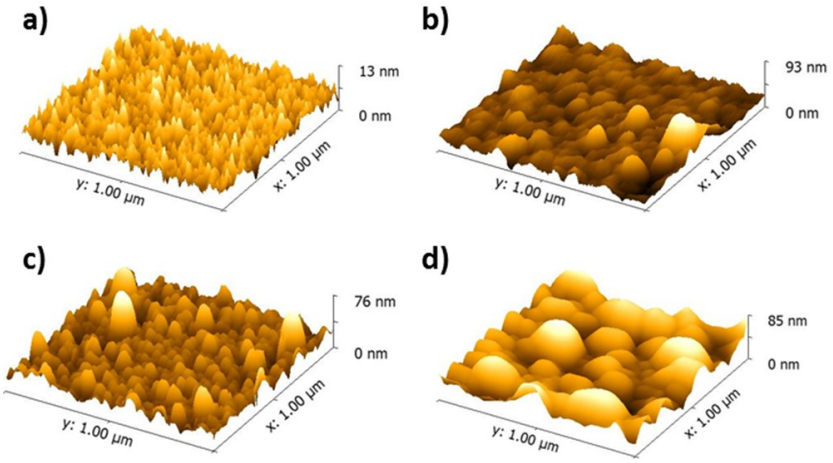

Figure 5.5: AFM images ($1\ \mu m \times 1\ \mu m$) of (a) the TiO_2 substrate, to (b) the Ag as deposited film, (c) the Ag/TiO_2 after annealing and, finally, (d) the TiO_2 capping layer.

According to AFM images analysis, we observe an increase of the roughness of the film from (a) 1.6 nm, to (b) 5.7 nm, (c) 8.1 nm and (d) 15.1 nm. The nanoparticles in Fig. 5.5 (c) have an average height of 15.1 nm.

SEM images in Fig. 5.6 clearly show the nanostructuration of the metal film (from Fig. 5.6(b) to Fig. 5.6(c)) and then the conformal coverture of the final 10 nm thick TiO_2 layer (from Fig. 5.6(c) to Fig. 5.6(d)).

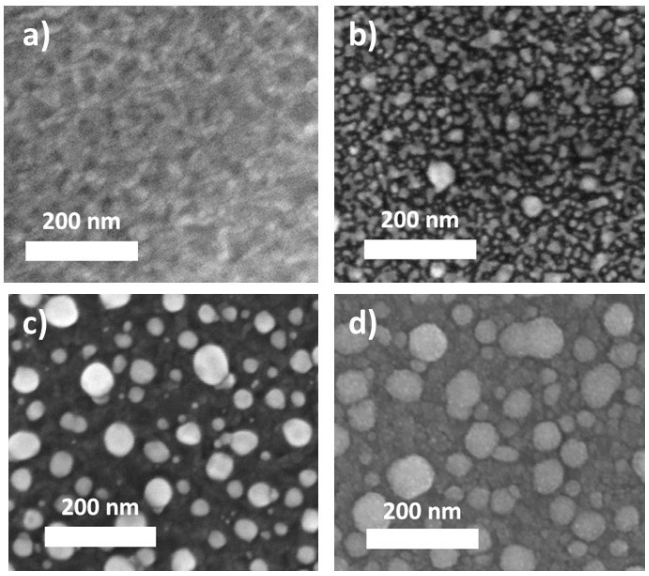

Figure 5.6: SEM images of (a) the TiO_2 substrate, to (b) the Ag as deposited film, (c) the Ag/TiO_2 after annealing and, finally, (d) the TiO_2 capping layer.

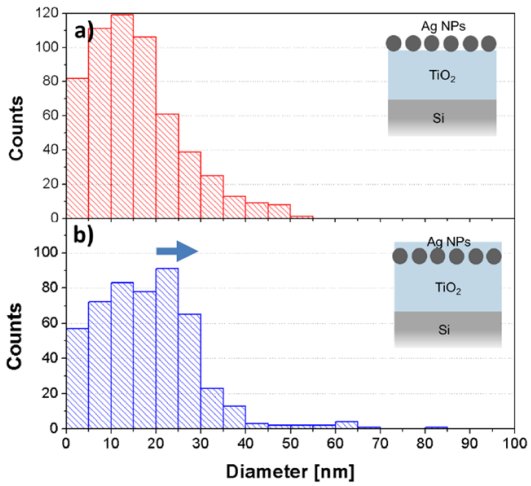

Figure 5.7: Size distribution of the Ag/TiO_2 nanocomposite film (a) before and (b) after the deposition of 10 nm of TiO_2 as capping layer.

This is further highlighted by the comparison of the nanostructures size distribution reported in Fig. 5.7. Indeed, we observe a shift in the distribution to higher diameters. One notes also that the size distribution is quite broad, spanning from 5 nm to 50 nm. This is peculiar of the dewetting nanostructuration, as already observed in Chapter 3 (see Fig. 3.5), and may turns out as an advantage in terms of a broadened plasmonic response, meaning an enlarged optical absorption in the visible range.

5.1.4 Optical characterization

The reflectivity measurements of the nanocomposite films noticeably enlighten the effect of optical amplification. Indeed, comparing the response of the Ag/TiO_2 composite with that of the bare TiO_2 one clearly observes the fingerprint of plasmonic excitations. As already mentioned, we prepared two substrates: one matched the antireflectivity conditions, while the other one was out of these conditions.

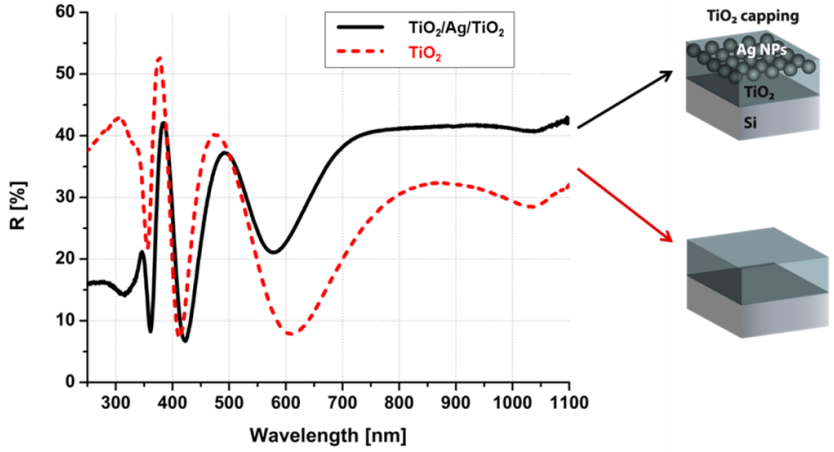

Figure 5.8: Reflectivity spectra of TiO_2/Si films, with (black continuous line) and without (red dashed line) Ag NPs. The measured matrix thickness is 176 nm. In this case we are out of antireflectivity conditions.

In Fig. 5.8 are reported the reflectivity spectra of the TiO_2/Si films, with and without Ag NPs, out of antireflectivity conditions. Note that the main differences introduced by the presence of Ag NPs consist of an increased absorption in the UV range (200 nm - 400 nm), due to intraband transitions in silver, and of a higher reflectance in the visible range. The plasmonic response of such Ag NPs is expected in the wavelength range between 700 nm and 800 nm. In this specific sample (bare TiO_2, red dashed line) we observe a minimum at about 600 nm.

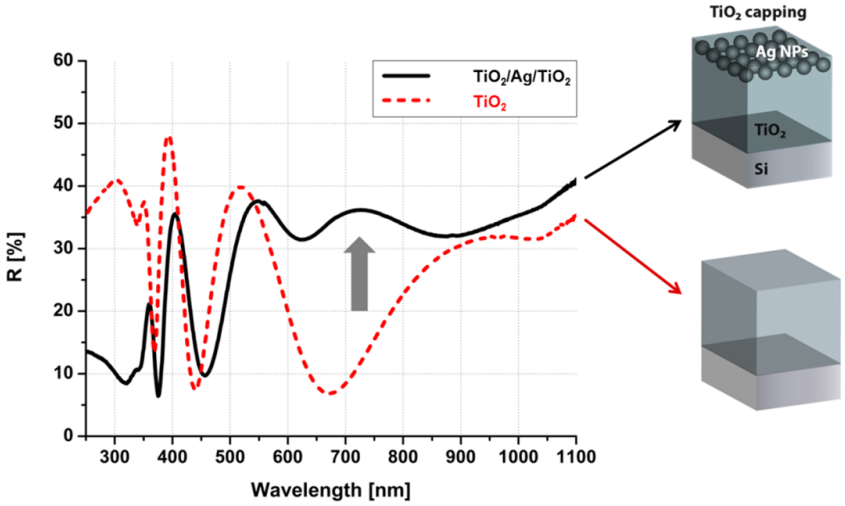

Figure 5.9: Reflectivity spectra of TiO_2/Si films, with (black continuous line) and without (red dashed line) Ag NPs. The measured matrix thickness is 193 nm. In this case we match the condition for optical amplification.

In Fig. 5.9 are reported the reflectivity spectra of the TiO_2/Si films, with and without Ag NPs, matching the antireflectivity conditions. First of all, we note that in this case the minima in reflectivity shifted, as expected, since the film thickness is different with respect the sample out of antireflectivity conditions (Fig. 5.8). Furthermore, in this case the presence of the Ag NPs gives the expected increased absorption in the UV range and an enhancement in the range between 700 nm and 800 nm. Note that the new bump in the spectra (grey arrow) is not due to a variation in the thickness of the matrix, but to the plasmonic response of the

nanostructured metal film. Although the simulations presented in the first part of this chapter (Fig. 5.2) suggest that Ag NPs having diameter between 20 nm and 40 nm should resonate in the wavelength range between 600 nm and 700 nm, one needs to consider some differences with respect to the simulation conditions. First of all, we have a broad distribution of sizes (see Fig. 5.7). Secondly, the simulation does not take into account the interactions among particles. In fact, looking at SEM caption in Fig. 5.6(c) one observes that the Ag NPs are quite close. Actually, the so-called "plasmon rule" states that two plasmonic particles do interact if the interparticle distance is lower than their diameter [Tab09]. This interaction causes a redshift in the plasmon resonance peak position [Mai07]. Lastly, in reflectivity measurements we detect the diffused component of the total plasmonic scattering fraction coming from metal nanoparticles. Thus, it is important to remind that the scattering cross section scales as the sixth power of diameter ($C_{sca} \propto D^6$), while the absorption cross section scales as the third power of diameter ($C_{abs} \propto D^3$) [Boh83][Mai07]. This implies that bigger particles give a higher contribution to scattering. It is known from theory (and from simulations) that bigger particles show redshifted resonances.

To qualitatively prove that this peak is due to plasmon resonances, we simulated the reflectance spectra of a TiO_2/AgNPs/TiO_2/Si hetero-structure by means of the effective medium approximation theory (EMA) [Bho83]. According to this approximation, it is possible to calculate the dielectric constant of a film constituted by small particles uniformly distributed in a matrix. The refractive index of the effective medium is given by:

$$\varepsilon_{EMA} \approx \varepsilon_m \left[1 + \frac{3f\left(\frac{\varepsilon - \varepsilon_m}{\varepsilon + 2\varepsilon_m}\right)}{1 - f\left(\frac{\varepsilon - \varepsilon_m}{\varepsilon + 2\varepsilon_m}\right)} \right] \qquad (5.1)$$

being ε and $\varepsilon_m$the dielectric constant of the embedding medium (TiO_2) and of the metal particles (Ag) respectively, and f the volume fraction of particles in the matrix. The dielectric constant ε_{EMA} is thus calculated by averaging the polarizability of the Ag and TiO_2 phases. However, this

approximation is reasonably verified for those medium composed by point-like nanoparticles embedded in isotropic matrix. Nonetheless, we can extract useful qualitative information on the optical behavior of the film. In fact, the finite NPs dimension and size distributions influence mainly the width and spectral position of the plasmon peak.

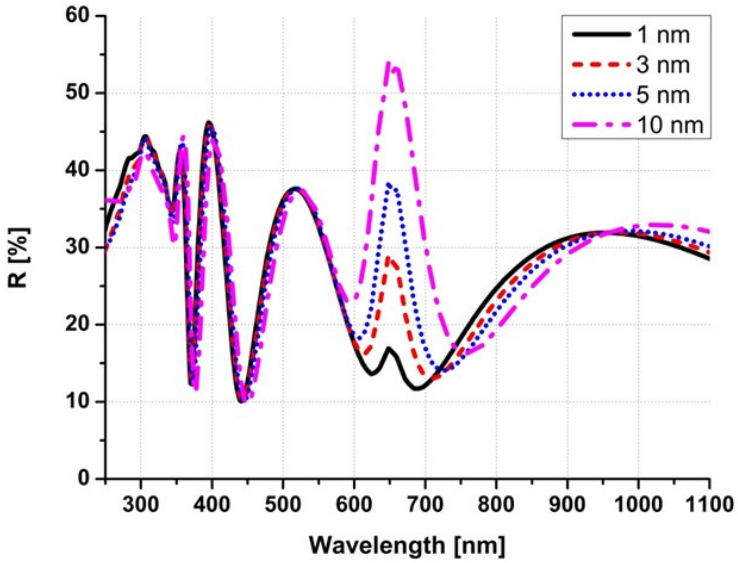

Figure 5.10: Simulated reflectance spectra of a 10 nm TiO_2/EMA Ag-TiO_2/170 nm TiO_2/Si multilayer varying the EMA layer thickness from 1 nm to 10 nm.

In Fig. 5.10 we report the reflectance spectra of a 10 nm TiO_2/EMA Ag-TiO_2/170 nm TiO_2/Si multilayer, varying the thickness of EMA layer, for a volume fraction $f = 0.1$. We have chosen a proper TiO_2 thickness so that the effect of the EMA layer is easily understandable, as we will show in the following. The peak at about 650 nm is due to the scattering of silver NPs within the EMA layer. Note how, as the Ag-TiO_2 layer thickness increases, the plasmon resonance peak increases its intensity. In fact a thicker layer corresponds to a higher number of scattering centers (particles). It is worth

noting how this peak, related to plasmon resonances of small silver NPs, is superimposed onto the TiO_2 reflectance spectra only in the region where plasmon resonance occurs. Furthermore, the position of this peak remains almost unchanged, taking into account a minor redshift due to the increase in the total thickness of the multilayer film.

5.1.5 Photocatalytic response under visible irradiation

In order to have more insight on the photocatalysis process we tested the photoactivity of our samples trough the discoloration of MB. The results of the photocatalytic test are summarized in Fig. 5.11.

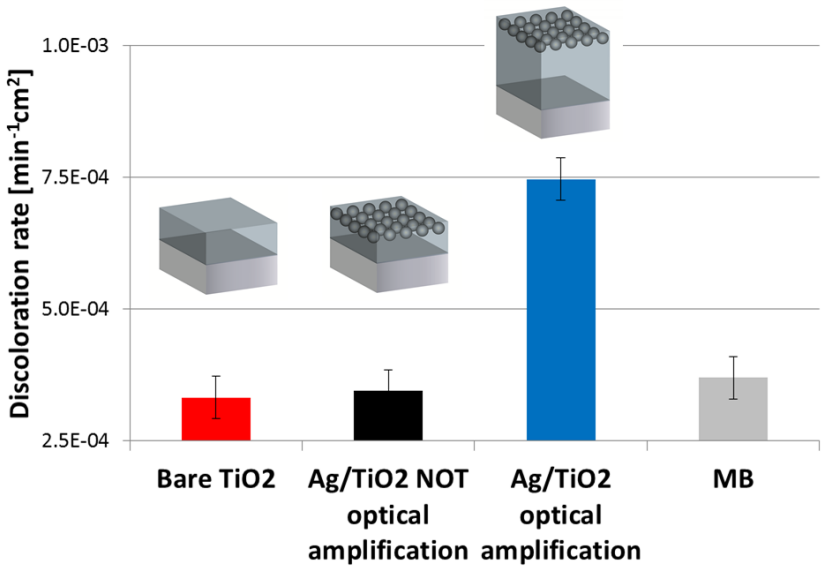

Figure 5.11: Discoloration test results under visible irradiation.

We compared the two TiO_2/Ag/TiO_2 nanocomposite films in and out the optical amplification conditions. We also measured the activity of a bare TiO_2 film whose 10 nm-thick superficial layer was prepared following the same procedure of the capping layer of Ag NPs. Methylene blue dye (MB)

degradation occurs under irradiation; therefore we report also the degradation of a vessel not containing photocatalytic material as reference. We observe that, as expected, TiO_2 is not active under visible illumination. The fundamental result of the test is that, despite having the same composition and superficial morphology, the two TiO_2/Ag/TiO_2 nanocomposite film show completely different behavior. In particular, the film matching the antireflectivity conditions is able to decompose the MB dye, showing a good photocatalytic activity in the visible range, while the film outside these conditions appears to be not active. These results underline the importance of a proper optical engineering of the supporting matrix for plasmon enhanced applications.

5.2 Conclusions

We obtained an Ag/TiO_2 nanocomposite activated by visible irradiation. Such an activity, occurring at irradiation energies below the absorption threshold of titania (gap) and thus not observable in the bare TiO_2 film, has been ascribed to the presence of plasmonic metal nanoparticles. Moreover, we observed a strong correlation between photocatalytic activity and optical amplification conditions. Therefore, we demonstrated the importance of proper film thickness engineering in order to take simultaneously advantage of plasmon resonances and optical interference. Actually, this result had been already demonstrated in Chapter 4 [Cac15], at least from the optical point of view. Such substrates are ideal candidates for solar-driven photocatalytic reactions. This result, in this last section, demonstrated also for photocatalysis, is actually more general, and could be potentially employed in other plasmo-electronic applications (e.g. SERS,…).

5.3 References

[Boh83] C. F. Bohren; D. R. Huffman, *Absorption of Light by Small Particles*, Wiley: New York, 1983.

[Cac15] G. Cacciato, M. Bayle, A. Pugliara, C. Bonafos, M. Zimbone, V. Privitera, M. G. Grimaldi, R. Carles, Nanoscale, **7**, 13468-13476 (2015).
[Ger15] SCATMECH version 7.00 (January 2015), by T. A. Germer, http://pml.nist.gov/Scatmech/html/index.htm
[Han11] D. A. H. Hanaor, C. C. Sorrell, J. Mater. Sci. , **46**, 855-874 (2011).
[Kel03] K. L. Kelly, E. Coronado, L. L. Zhao, G. C. Schatz, J. Phys. Chem. B, **107**, 668-677 (2003).
[Joh72] P. B. Johnson, R. W. Christy, Phys. Rev. B, **6**, 4370 (1972).
[Lan12] M. Landmann, E. Rauls, W. G. Schmidt, J. Phys.: Cond. Matt., **24**, 195503 (2012).
[Lut14] T. Luttrell, S. Halpegamage, J. Tao, A. Kramer, E. Sutter, M. Batzill, Scientific Reports **4**, Article number: 4043 (2014) doi:10.1038/srep04043.
[Mai07] S. A. Maier, *Plasmonics: Fundamentals and Applications*, Springer, 2007.
[Nog07] C. Noguez, J. Phys. Chem. C, **111**, 3806-3819 (2007).
[Ruf15] F. Ruffino, M. G. Grimaldi, Phys. Status Solidi A, 1–23 (2015) / DOI 10.1002/pssa.201431755.
[Tab09] C. Tabor, R. Murali, M. Mahmoud, M. A. El-Sayed, J. Phys. Chem. A, **113**, 1946-1953 (2009).

Conclusions

In the work presented in this thesis, two approaches have been followed: TiO_2 nanoparticles obtained via laser ablation and optical engineering of multilayered metal-TiO_2 thin films.

In the first approach, TiO_2 nanoparticles are synthetized by pulsed laser ablation in liquid, a novel, industrially scalable and eco-friendly technique. The laser ablated nanoparticles (LA-NPs) were found to be in amorphous phase. Nevertheless, they showed a photocatalytic activity comparable to that of crystalline commercial powder and a higher antibacterial activity. This unexpected result has been explained taking into account the effects of disorder and hydrogen inclusion in the structure of TiO_2 nanoparticles. In fact, these characteristics are reported to be responsible for the presence of superficial charge traps, that help the scavenging of electrons and, thereby, improve photocatalytic reactions. Mixing TiO_2 LA-NPs with Ag nanoparticles has been demonstrated to further increase the photocatalytic efficiency of TiO_2, thanks to an enhanced charge separation. In this approach nanoparticles are dispersed in solution. In view of water remediation technologies this may results as a disadvantage, introducing more step in the purification process. Therefore we proposed a second approach based in the use of thin films.

In the thin film approach, we studied composite films of metal (Au or Ag) nanoparticles (NPs) and TiO_2 for plasmon-enhanced photocatalysis. Using thermal dewetting or low-energy ion beam synthesis, metal NPs have been formed on top, or located at well-defined depth below the surface of a TiO_2 layer. We demonstrated that the plasmonic effect can be effectively amplified using an antireflective multilayer. This allows increasing the photon capture in a desired spectral range and enhancing this capture in a very thin layer near the surface.

Photocatalytic activity has been observed under visible irradiation in multilayer Ag/TiO_2 nanocomposite samples in which the preparation procedure and stacking sequence were accurately selected. Such an activity, occurring at irradiation energies below the absorption threshold of

titania (gap) and thus not observable in the bare TiO_2 film, has been ascribed to the presence of plasmonic metal nanoparticles in optical amplification conditions. Therefore, the importance of proper film thickness engineering in order to take simultaneously advantage of plasmon resonances and optical interference has been evidenced.

List of publications

This thesis is based on the following publications:

1. **G. Cacciato**, G. Sanzone, M. Zimbone, F. Ruffino, G. Piccitto, A. M. Mio, R. Carles, V. Privitera, M. G. Grimaldi, "*Optical engineering of Ag/TiO_2 nanocomposite films for visible driven photocatalysis*", in preparation.

2. M. Zimbone, **G. Cacciato**, R. Sanz, R. Carles, V. Privitera, M. G. Grimaldi, "*Enhanced photoactivity in black titanate photocatalyst synthetized by laser irradiation in water*", submitted.

3. M. Zimbone, **G. Cacciato**, R. Sanz, N. Piluso, F. La Via, G. Amiard, S. Boninelli, R. Carles, M. A. Buccheri, G. Rappazzo, M. G. Grimaldi, V. Privitera, "*Effect of annealing temperature and pH on the structure, photo-catalytic and antibacterial activity of TiO_2 nanoparticles obtained by pulsed laser ablation in liquids*", submitted.

4. M. Zimbone, **G. Cacciato**, M. A. Buccheri, R. Sanz, N. Piluso, R. Reitano, F. La Via, M. G. Grimaldi, V. Privitera, "*Photocatalytical activity of amorphous hydrogenated TiO_2 obtained by Pulsed Laser Ablation in Liquid*", Materials Science in Semiconductor Processing, (2015), http://dx.doi.org/10.1016/j.mssp.2015.09.012.

5. **G. Cacciato**, F. Ruffino, M. Zimbone, R. Reitano, V. Privitera, M. G. Grimaldi, "*Au thin films nano-structuration on polycrystalline anatase and rutile TiO_2 substrates towards photocatalytic applications*", Materials Science in Semiconductor Processing, (2015), http://dx.doi.org/10.1016/j.mssp.2015.07.074.

6. **G. Cacciato**, M. Bayle, A. Pugliara, C. Bonafos, M. Zimbone, V. Privitera, M. G. Grimaldi, R. Carles, "*Enhancing carrier generation in*

TiO_2 by a synergistic effect between plasmon resonance in Ag nanoparticles and optical interference", Nanoscale, **7**, 13468-13476, (2015). http://dx.doi.org/10.1039/c5nr02406d

7. M. Zimbone, M. A. Buccheri, **G. Cacciato**, R. Sanz, G. Rappazzo, S. Boninelli, R. Reitano, L. Romano, V. Privitera, M. G. Grimaldi, "*Photocatalytical and antibacterial activity of TiO_2 nanoparticles obtained by laser ablation in water*", Applied Catalysis B: Environmental, **165**, 487-494, (2015). http://dx.doi.org/doi:10.1016/j.apcatb.2014.10.031

Other publications:

8. R. Carles, M. Bayle, P. Benzo, **G. Cacciato**, V. Privitera, G. Benassayag, C. Bonafos, "*Plasmon-resonant Raman spectroscopy in metallic nanoparticles: surface-enhanced scattering by electronic excitations revisited*", Physical Review B, **92**, 174302 (2015). http://dx.doi.org/10.1103/PhysRevB.92.174302

9. S. Spampinato, **G. Cacciato**, M. Zimbone, F. Ruffino, M. G. Grimaldi, "*Quantitative evaluation of surface topographical changes of Au thin films after DNA immobilization*", Chemical Physics Letters, **639**, 120, (2015). http://dx.doi.org/doi:10.1016/j.cplett.2015.09.006

10. **G. Cacciato**, M. Zimbone, F. Ruffino, A. Sciuto, G. D'Arrigo, M. G. Grimaldi, "*Growth dynamics of quasi-one-dimensional confined Au nanoparticles on SiO_2 surface*", Materials Letters, **141**, 347, (2015). http://dx.doi.org/10.1016/j.matlet.2014.11.096

11. A. Gentile, **G. Cacciato**, F. Ruffino, R. Reitano, G. Scapellato, M. Zimbone, S. Lombardo, A. Battaglia, C. Gerardi, M. Foti, M. G. Grimaldi, "*Electrical properties modulation of thin film solar cell using gold nanostructures at textured FTO/p-i-n interface*", Functional Materials Letters, **8** (2), 1550017, 2015. http://dx.doi.org/10.1142/S1793604715500174

12. A. Gentile, **G. Cacciato**, F. Ruffino, R. Reitano, G. Scapellato, M. Zimbone, S. Lombardo, A. Battaglia, C. Gerardi, M. Foti, M. G. Grimaldi, "*Nano-scale structuration and optical properties of thin gold films on textured FTO*", Journal of Materials Science, **49** (24), 8498, (2014). http://dx.doi.org/10.1007/s10853-014-8560-1

13. F. Ruffino, **G. Cacciato**, M. G. Grimaldi, "*Surface diffusion coefficient of Au atoms on single layer graphene grown on Cu*", Journal of Applied Physics, **115** (8), 084304, (2014). http://dx.doi.org/10.1063/1.4866876

Curriculum Vitae

Giuseppe Cacciato was born on May 11th 1988 in Enna (Italy). He attained his Master Degree in Physics (110/110 *cum laude*) from University of Catania in 2012. He spent a period of 4 months at imec (Leuven, Belgium) during an internship in the framework of the Erasmus Placement program, working on his master thesis project. In 2012 he was also admitted to the Ph.D. course in Materials Science at the University of Catania. He is currently working under the supervision of Prof. Maria Grazia Grimaldi at the Department of Physics and Astronomy of the University of Catania and at the CNR-IMM MATIS group of Catania. His main scientific interests are focused on plasmonic metal nanoparticles and photocatalysis. During his Ph.D. project he has been actively involved in several scientific collaborations with: CNR-IMM, ST Microelectronics – 3SUN, CEMES CNRS – University of Toulouse, University of Oslo. He spent part of his research activity at CEMES CNRS – University of Toulouse under the supervision of Prof. Robert Carles. He was tutor of the course of Physics for Biologists and Pharmacists and of the course of Experimental Physics for Physicists at University of Catania. During his Ph.D. he attended two international summer schools (Ettore Majorana Foundation and Centre for Scientific Culture International School of Atomic and Molecular Spectroscopy "NANO-STRUCTURES FOR OPTICS AND PHOTONICS", Ettore Majorana Foundation and Centre for Scientific Culture International School of Solid State Physics 62nd Course "Materials for Renewable Energy") and national and international conferences (EMRS Spring Meeting 2014, 100° Congresso SIF – Pisa 2014, IEEE NMDC 2014, MRS Fall Meeting 2014, EMRS Spring Meeting 2015) giving oral and poster contributions. He won the Best Poster Award

at EMRS Spring Meeting 2015 Symposium B. He is author or co-author of 10 articles, published in international referred scientific journals.

Acknowledgements

First of all, I would like to thank my tutor, prof. Maria Grazia Grimaldi. Her guidance and support have made me able to better understand and appreciate our work; although her busy agenda, she always found time to discuss and help me.

My gratitude also goes to Dr. Vittorio Privitera, who has given me the possibility to work within the WATER project.

A special thank goes to Prof. Robert Carles (CEMES CNRS – University of Toulouse). His deep knowledge and his ability in explaining even the most complex things gave me an invaluable opportunity to understand difficult topics in the field of nanoscience.

My sincere gratitude also goes to Dr. Massimo Zimbone and Dr. Francesco Ruffino, two of the most brilliant researchers that I have ever met. Their patient and constant mentoring helped me to grow as a scientist. My academic career would not have been the same without their advices and their assistance.

I have to thank Giuseppe Sanzone for the excellent work he did during his master thesis project.

I want to thank Prof. Francesco Priolo and Prof. Antonio Terrasi, former and current head of the research unit, for having involved me in the CNR-IMM MATIS group. I am grateful to Prof. Riccardo Reitano, Prof. Giovanni Piccitto, Prof. Bengt Svensson , Prof. Lucia Romano and Dr. Ruy Sanz for their scientific support and fruitful discussions.

These years spent working in MATIS group has been a precious experience. I had the possibility to interact and exchange ideas with many

different people and everyone left me something. For this reason my sincere thanks go to all of them.

I wish to thank the people I met during the period that I spent at CEMES CNRS – University of Toulouse: Dr. Maxime Bayle, Alessandro Pugliara and Dr. Caroline Bonafos.

E' stato un piacere condividere il percorso di dottorato con Vicky, Adriana ed Enrica. Il viaggio è stato particolarmente divertente grazie a loro ed anche alla mitica sala dottorandi, per cui grazie a Brunilde, Maria, Emanuele, Giuseppe, Marta e Laura.

Il periodo di studio è stato segnato anche dalla condivisione di amore ed odio per la scienza con Lisa e Sofia. Le generazioni future dovranno tenere conto delle vostre riflessioni.

Grazie al gruppo dei *pagghiazzi*, che si sostiene anche se sparso per tutta l'Europa.

Grazie alla mia famiglia e a Danila, per esserci stati anche nei momenti più duri.